Extreme Precipitation and Flash Floods in Central Western Europe

Occurrences, Atmospheric Conditions, and Regionalized Modelling

Judith Nijzink

PhD thesis

Doctoral School of Science and Engineering
Faculty of Science, Technology, and Medicine
University of Luxembourg

Judith Nijzink

Extreme Precipitation and Flash Floods in Central Western Europe
- Occurrences, Atmospheric Conditions and Regionalized Modelling

Cover: White Ernz, Altlinster, Luxembourg, 2021. The White Ernz is known in Luxembourg for having hosted two destructive flash floods in 2016 and 2018.

151 pages.
PhD thesis
Electronic version on ORBilu (October 30, 2024)
University of Luxembourg
Esch-sur-Alzette, Luxembourg (2024)

PhD-FSTM-2024-069
An electronic version of this dissertation is available at the Open Repository and Bibliography of the University of Luxembourg (ORBilu):
https://orbilu.uni.lu/

UNIVERSITÉ DU LUXEMBOURG

PhD-FSTM-2024-069
The Faculty of Science, Technology and Medicine

DISSERTATION

Defence held on 17/10/2024 in Esch-sur-Alzette

to obtain the degree of

DOCTEUR DE L'UNIVERSITÉ DU LUXEMBOURG EN SCIENCES DE L'INGÉNIEUR

by

Judith NIJZINK
Born on 8 October 1991 in Schwetzingen (Germany)

EXTREME PRECIPITATION AND FLASH FLOOD EVENTS IN CENTRAL WESTERN EUROPE

– OCCURRENCE, ATMOSPHERIC CONDITIONS AND REGIONALIZED MODELLING

Dissertation defence committee

Dr. Olivier Francis, Chairman
Professor, University of Luxembourg

Dr. Erwin Zehe, Vice Chairman
Professor, Karlsruhe Institute of Science and Technology

Dr. Laurent Pfister, dissertation supervisor
Professor, University of Luxembourg

Dr. Ryan Teuling
Associate Professor, Wageningen University and Research

Dr. Patrick Willems
Professor, Catholic University Leuven

Abstract

The recent accumulation of extreme rainfall and subsequent flash flood events in Luxembourg in 2016 and 2018 has raised two major concerns:

1. How can the extreme rainfall and runoff events that recently occurred in Luxembourg and the Greater Region be conceptualized in an era of proven global change?

2. Can we use large-scale data sets and machine learning algorithms to simulate extreme and flash flood events?

To evaluate potential trends in the frequency and magnitude of extreme precipitation and flash flood events, we identified and analysed thunderstorm relevant weather patterns and atmospheric conditions. Therefore, we made use of the objective weather pattern classification by Hess and Brezowsky (1977) and proxy parameters from reanalysis data (ERA 5) representing abundant atmospheric moisture contents, sufficient atmospheric instability, and low wind speed and shear winds. These three categories typically characterize thunderstorm conditions with intensive and long-lasting rainfall, that have the potential to trigger flash floods. The occurrence of all other weather patterns fluctuated without clear trends between 1960 and 2018, whereas the occurrence of trough weather patterns, which can be relevant for meridional, thunderstorm causing conditions, has increased over time. However, between 1980 and 2020, we did find significant increases in the occurrence frequency and amount of abundant absolute atmospheric moisture contents along with increases in high atmospheric instability. These findings are the basis for potential increases in the occurrence and intensity of extreme precipitation and flash flood events.

Moreover, regarding the damage potential of flash floods, it is crucial to further develop the simulation of peak flows. As most hydrological models used in forecasting are exceeding their design limits during extreme summer peak flow events, we explore the potential added value of large hydrological data sets. Therefore, we physiographically characterized the entire region of the Luxembourgish stream network and collected hydro-meteorological data, which were compiled in the CAMELS-LUX data set. With this data we trained and tested a neural network (Long Short-Term Memory, LSTM). For the first time, we were simulating discharge in all 56 nested catchments achieving overall reasonable model results. However, also the LSTM model had difficulties simulating the extreme peak flows mentioned above. Attempts to improve the model performance during summer peak flows by adding the identified thunderstorm relevant atmospheric parameters to the model and increasing its temporal resolution, did not lead to significant improvements. Instead, we noticed

the inability of the standard LSTM to extrapolate discharge simulations to values outside the normalized range of the training data. This shows the design limits of data-based models, that function very well only during conditions that are well represented in the training data set.

Overall, my research has contributed to a better understanding of the development of flash floods, that might not only be linked to atmospheric changes, but also to other determining driving factors. With the extensive description of hydrological data in and around Luxembourg, we pave the way for further exploitation of regional hydrological data. Delivering the basic LSTM model as a tool opens a range of possibilities for further model development and analyses.

Keywords: Intensification of the hydrological cycle, extreme precipitation, extreme precipitation favouring atmospheric conditions, atmospheric proxy parameters, flash floods, non-stationary hydrological systems, machine learning, long short-term memory (LSTM) model, central western Europe, Luxembourg.

Contents

1 General introduction

Hydrological extremes comprise both intense precipitation events causing flooding and inundations on the one hand as well as extended periods of precipitation deficits leading to prolonged dry spells and droughts on the other hand. Both extremes of the hydrological spectrum range among the most destructive and costliest natural catastrophes with losses due to flooding amounting up to 300 billion US$ between 2018 and 2022 (MunichRe, 2024). The by far costliest flood disaster in decades occurred in July 2021 across parts of western Germany, eastern Belgium, the south of the Netherlands and Luxembourg, with an overall loss of 46 billion € (54 billion US$) (MunichRe, 2024) and the tragic loss of more than 200 lives (BMI, 2022; Crisis Centrum, 2021). Continuous rainfall over the entire region for several days ended up saturating the soils. In the following days, extreme precipitation cells triggered fast runoff reactions (Kreienkamp et al., 2021). Along similar lines, stagnating warm and moist air masses sustained an episode of flash floods in the summers of 2016 and 2018 on a much more localized scale in Luxembourg and western Germany. While on 22 July 2016 a flash flood affected the catchment of the White Ernz (Iffly et al., 2018; Pfister et al., 2018; Mathias, 2021) it was the neighbouring catchment of the Black Ernz that experienced a similar event two years later on 1 June 2018. Just one week later on 7 June 2018, heavy precipitation again caused a flood event in the Kaasselbach, located in the Black Ernz catchment (Pfister et al., 2020; Mathias, 2019). Successive catastrophic events like those above lead to critical concerns and stimulated the scientific community to delve deeper into the underlying causes (Hao et al., 2018; IPCC, 2022).

While hydrological extremes count already today among the most devastating natural disasters (MunichRe, 2024), global climate change is projected to further intensify hydrological extremes in frequency, magnitude and areal extent (e.g. Donat et al., 2016; Wu et al., 2013; Yang et al., 2021). Moreover, the event-to-event variability is expected to increase (Madakumbura et al., 2019; Ficklin et al., 2022). These assumptions are based on the physical understanding of thermodynamic processes,

where warmer air masses intensify moisture fluxes between the ocean, the land surface and the atmosphere and increase the atmospheric saturation vapour pressure (Allan et al., 2020). According to the Clausius-Clapeyron relationship, an increase of 6-7% of the global atmospheric water vapour is assumed per Kelvin degree air temperature increase, when averaged at the global scale. Based on this assumption the hydrological cycle is potentially influenced in two ways: increasing precipitation intensities (Tandon et al., 2018; Pfahl et al., 2017; Trenberth et al., 2003; Giorgi et al., 2019) as well as increasing atmospheric evaporation demand (Scheff and Frierson, 2014; Allan et al., 2020). The latter is however mitigated by dynamic vegetation responses to elevated atmospheric vapour pressure and elevated CO_2, which increase the plant water use efficiency (Ficklin et al., 2022; Lemordant et al., 2018; Milly and Dunne, 2016).

Changes in the global water cycle are very complex and are involving various uncertainties in the responses of the hydrological systems at the regional and local scale (Koutsoyiannis, 2020). Local changes in water availability are controlled by global circulation patterns and altered by smaller scale physical processes, such as topography, land use and human interactions, that affect local water and energy fluxes (Thackeray et al., 2018; Giorgi et al., 2019; Daniels et al., 2016; Champion et al., 2015). While local features of the water cycle are the result of an interplay between multiple drivers (Allan et al., 2020) our research focussed on the overarching controlling mechanisms, namely the weather patterns and the atmospheric conditions. They are determined by changing heating and cooling patterns throughout the atmosphere and across the planet's surface (Allan et al., 2020). We investigated the weather patterns and atmospheric conditions during extreme precipitation and subsequent flash flood events and their fluctuations over the past decades (Chapter 3, 4), to test the following hypotheses:

> "The strong correlation between atmospheric circulation types and winter discharge observed in the second half of the 20^{th} century for central western Europe still prevails today."
>
> "The recent accumulation of extreme precipitation and flash flood occurrences in central western Europe is triggered by a change in atmospheric circulation patterns."
>
> "A change in atmospheric conditions has led to more frequent extreme precipitation events that have subsequently triggered flash flood events in central western Europe."

The non-stationarity of hydrological systems is a considerable source of uncertainty for the predictability of the reaction of catchments. A stationary hydrological system would by definition keep a stable mean and variance of rainfall and discharge behaviour along with a constant water storage over time (Koutsoyiannis, 2020; Slater et al., 2021). Statistics based on the assumption of stationarity are used to date when calculating return periods for flood protection measures and engineering constructions (e.g. Slater et al., 2021). Yet, changing global circulation patterns as well as local human interferences with the hydrological system through varying land or water

use, proof this assumption wrong (Allan et al., 2020; Slater et al., 2021). Moreover, the disruptive nature of extreme flood events has the potential to irreversibly alter a catchment's geomorphology and subsequent hydrological responses (e.g. Bronstert et al., 2018).

As a catchment's non-stationarity is extremely difficult to assess, the assumption of stationary conditions still builds the basis of standard hydrological tools and process-based models. Both, conceptional models as well as highly resolved physical based models rely on storage-controlled modelling concepts calibrated on the *status quo* of the past (Devi et al., 2015). This concept is suitable for operational purposes simulating slowly developing river floods in mesoscale catchments. Yet, under the increasing pressure to simulate faster runoff reactions in smaller catchments, these models are being pushed beyond their design limits, which leads to high errors and uncertainties in streamflow simulations. Achieving the simulation of these fast runoff mechanisms would however be a *conditio sine qua non* when aiming for the projection of robust future streamflow conditions and especially unprecedented extreme events.

A way to overcome the stationary constraints of conventional hydrological models could be machine learning algorithms. Machine learning algorithms extract and reproduce temporal and spatial patterns in the data sets they are trained on and rely on past observed data just as conventional hydrological models (Shen et al., 2021). Yet, using a regionalized modelling approach and mining the data of many catchments largely increases the amount of input data and allows the model to learn universally applicable physical laws through extensive training (Shen et al., 2021). Nearing et al. (2021) even suggests that these large-scale data sets, on which the models are trained, might contain more information than experts could extract and implement in the design of conceptual models. The catchments' heterogeneity is thereby represented through standardized catchment characterizations. Climatic variations beyond the observed extents within one catchment can be compensated through observations in other catchments to certain extents. This increases the chance, that extraordinary events in one catchment have already been observed in another allowing the model to directly apply the behaviour in catchments experiencing certain conditions for the first time (Nearing et al., 2019; Bertola et al., 2023). Yet, more testing is needed to prove that machine learning algorithms are capable of making predictions outside the range of their respective training data set (Shen et al., 2018; Feng et al., 2020). Based on our physiographic characterization of Luxembourg (CAMELS-LUX data set, Chapter 2), we have set up a regionalized LSTM model (Long Short-Term Memory). We used this model to test the following hypothesis in Chapter 2:

> "LSTMs are capable of simulating discharge across catchments with contrasted physiographic settings in and around Luxembourg."

With purely data-based modelling approaches being independent from our understanding of physical dependencies of parameters, we would like to leverage this model design and add atmospheric input parameters relevant for the formation of extreme precipitation. The relation between atmospheric parameters potentially triggering extreme precipitation events and eventually streamflow behaviour is extremely interwoven and complex. Yet, knowing that they are related, we conjecture that adding

this information provides a broader description of the hydrological conditions leading to the summer peak discharge events. In Chapter 5, we therefore hypothesize:

> "An hourly resolution improves the model performance during summer peak flow events."

> "Including atmospheric variables relevant for extreme precipitation improves the simulation of summer peak flow events."

The research hypotheses and questions mentioned above are developed in the four chapters of this thesis. Chapter 2 focusses on the hydro-climatological and physiographic characterisation of the greater region of Luxembourg, presenting the resulting CAMELS-LUX data set. Chapter 3 investigates the relation between atmospheric circulation patterns and precipitation and streamflow as well as variations in their occurrences. Chapter 4 builds on Chapter 3 identifying and analysing thunderstorm relevant atmospheric proxy parameters. Chapter 5 combines all collected data and findings in the LSTM model for Luxembourg. Note that all chapters rely on scientific publications or conference contributions that have either been published, submitted or are planned for submission to peer-reviewed scientific journals (see List of publications).

2

CAMELS-LUX: Highly Resolved Hydro-Meteorological and Atmospheric Data for Physiographically Characterized Catchments around Luxembourg

This chapter sets the scene of the study area - the Greater Region of Luxembourg - around which all of this thesis' chapters are centred. The Greater Region is physiographically characterized in terms of topography, geology and landuse, but also described from a hydrological point of view. We include general hydrometeorological parameters but also focus on a few local features. This data set includes thunderstorm relevant atmospheric proxy parameters analysed in Chapter 4 and forms the basis for simulations using the LSTM in Chapter 5.

This chapter is based on:

Nijzink, J., Loritz, R., Gourdol, L., Iffly, J. F., Zoccatelli, D. and Pfister, L.: CAMELS-LUX: Highly resolved hydro-meteorological and atmospheric data for physiographically characterized catchments around Luxembourg, Earth Syst. Sci. Data, [in preparation].

Author contribution:

JN collected and processed the time series data and wrote the first draft. LG calculated the topographic indices for the catchment characterization. RL provided the model code for the benchmark model and the CARAVAN extension. All the co-authors (JN, LG, JFI, RL and LP) contributed to and edited the manuscript.

2.1 Introduction - Meta data

Within recent years, data-driven processes gained increasing importance in hydrology. Therefore, it is crucial to have comprehensive data sets of high quality. With this Luxembourgish data set we contribute to international initiatives in large-sample hydrology, such as the work done around differing CAMELS data sets (Catchment Attributes and MEteorology for Large-sample Studies) that work towards the classification and regionalization of catchments trying to increase the robustness of models. So far, CAMELS data sets have been published for catchments in the USA (CAMELS, Addor et al., 2017), Chile (CAMELS-CL, Alvarez-Garreton et al., 2018), Brazil (CAMELS-BR, Chagas et al., 2020), Great-Britain (CAMELS-GB, Coxon et al., 2020), Central Europe (LamaH-CE, Klingler et al., 2021), Australia (CAMELS-AUS, Fowler et al., 2021), and Switzerland (CAMELS-CH, Höge et al., 2023) and are under construction for Germany (CAMELS-DE, Loritz et al., 2022), and France (CAMELS-FR, Andréassian et al., 2021). In recent efforts the CAMELS have been aligned for further consistency in the CARAVAN data set that can be extended by the hydrologic community via a corresponding cloud-based platform (Kratzert et al., 2023). As the forcing data of the CARAVAN data set is extracted from the coarse ERA5 reanalysis data, a few deficiencies in the data quality, and especially the overestimated potential evaporation, need to be kept in mind, when applying the data set (Clerc-Schwarzenbach et al., 2024).

CAMELS-LUX data is available for 56 catchments, that drain into the Luxembourgish stream network at some point. The catchments in CAMELS-LUX are very heterogeneous from a physiographic point of view and homogenous from a climatic perspective. The density of stations is rather high and allows therefore a quite unique view on physiographic controls on rainfall-runoff transformation processes (and how they may be affected by changes in climate). The provided catchments are incorporated in a nested setup and include a few rather homogeneous, small headwater catchments. The catchments are characterized physically including basic geographic data such as the catchment area, the outlet location and major water courses, but also data of geology and land-use classes within the catchments. These classes are grouped based on their hydrologic properties. Additionally, topographic measures are included, that can help to further classify the catchments.

Most of the catchment's time series range from 01.11.2004-31.10.2021, with a few catchments being limited by the availability of discharge data. The time series are available at three temporal resolutions: 15-minutes, hourly and daily. The high temporal resolution of the CAMELS-LUX data set allows analyses with respect to convective short-term extreme precipitation events and possible subsequent runoff events in small catchments. The time series covered in the data set encompass stream flow, aggregated radar precipitation (RadKlim, Winterrath et al., 2018), interpolated station precipitation (from AGE, ASTA, DWD, LIST, MeteoLux) as well as atmospheric and soil moisture reanalysis data (ERA 5, Hersbach et al., 2023a,b; Muñoz Sabater, 2019). Rainfall is often determined by large scale atmospheric patterns and therefore, the atmospheric parameters provide valuable additional information about the meteorological conditions (Lengfeld et al., 2019). The atmospheric parameters of this CAMELS-LUX data set were chosen due to their relevance during thunder-

storms (Chapter 4). Consequently, they allow a better identification of extreme precipitation and flash flood favouring atmospheric conditions.

The CAMELS-LUX data set was originally developed for setting up a regional LSTM for the entire country of Luxembourg hypothesizing that LSTMs are capable of simulating discharge across catchments with varying physiographic settings in and around Luxembourg. The benchmark model is included in Sect. 2.6.2. As this data set includes a sufficiently high temporal resolution and the thunderstorm relevant atmospheric conditions, the research focus lies on the simulation of summer peak flows (Chapter 5).

2.2 Hydro-meteorologic time series

2.2.1 Discharge

Discharge data for Luxembourg was collected from stations of the Luxembourgish Water Agency (AGE) and the Luxembourg Institute of Science and Technology (LIST). The discharge data for the German region was provided by the Rhineland-Palatine State Office for Environment (LfU-RLP, 2022).

The discharge is measured at 56 stream gauges that contribute to the Luxembourgish stream network. This stream network includes headwater catchments that include areas on the Belgian and French side of Luxembourg, as well as areas and streams on the German side. The Our and the Sure River in the East, mark a part of the border between the two countries. The original temporal resolution of the discharge measurements is 15 minutes. This time step dictates the minimum resolution for this data set. Data was aggregated to hourly and daily time steps. For most catchments, data is available for the entire time period of this data set. Ten catchments (ID 12, 20, 31, 36, 37, 38, 46, 54, 55, 56) do not cover the entire time period of this data set and typically start one or two years later. The significantly shorter time series are the catchments, in which flash floods were observed (ID 55-56).

Discharge data was processed to fill all gaps in the time series. The data gaps were examined individually and compared to neighbouring stream gauges. Decisions were taken individually according to the following "rules": If the gaps only covered very few time steps, in which no precipitation fell, data was interpolated linearly. If there was rainfall and streamflow was not in the recession period, the specific discharge was introduced from the surrounding stream gauge, that reacted the closest to the stream gauge that needed to be filled within the days or weeks around the data gap. In the data set, a flag column was included to indicate interpolated values. "0" are original values, "1" stands for a linear interpolation. All further numbers are surrounding stream gauges.

2.2.2 Precipitation

Radar data

The precipitation radar data is derived from the radar product RadKlim ("Radar-based Precipitation Climatology" - YW) by the German Weather Service (DWD, ver-

sion 2017.002 - Winterrath et al., 2018). RadKlim is a reprocessed and quasi gauge-adjusted version of the DWD's operational Radolan ("Radar-Online-Adjustment") product. The data quality is high, even though precipitation might be underestimated during extreme rainfall events (Kreklow et al., 2020; Pöschmann et al., 2021).

The radar data was spatially aggregated. The 1 km × 1 km sized grid cells were considered for a catchment if their center point lies within the catchment area. The area of Weierbach catchment (ID 50) is the by far the smallest within the data set (0.4575 km^2)) and does not contain any radar grid cell center. In this case, we averaged the 4 grid cells, that partly overlay the catchment.

The original data has a temporal resolution of 5 minutes and was accumulated to this data set's 15 minute, hourly and daily time step. Apart from the aggregated rain rate, we extracted the maximum and the minimum rain rate within one grid cell and one timestep (in the original 5-minute resolution). The 5-minute maximum rain rate can be used as an indicator for the precipitation intensity during an extreme event. The 15-minute, hourly and daily resolution of the data still contain the minimum and maximum rain rate per 5 minutes within the respective time steps. In case missing values persisted in the final time series per catchment, these gaps were eventually filled with an interpolated data product described in the next paragraph. The 5-minute minimum and maximum rain rates in the data set are taken from the min and max of the station data and calculated from a further disaggregation. They clearly do not represent the maximum 5-minute rain rate and are therefore not really comparable to the radar data but are closest to what we could extract from the data. All values that are replaced within the radar precipitation time series are marked with a flag, that is set to 1.

Interpolated station data

To complement the radar data, we added the spatially interpolated station data as an extra time series. We used 66 stations that are spread over Luxembourg and Germany, maintained by the Luxembourgish Water Agency (AGE), the Luxembourgish Ministry of Agriculture (ASTA), the Luxembourg Institute of Science and Technology (LIST), the Luxembourgish Weather Service (MeteoLux) or the German Weather Service (DWD). This data is available at an hourly resolution for Luxembourg and 10-minute resolution for Germany. We disaggregated or aggregated data respectively to reach the 15-minute, hourly and daily temporal resolutions. The disaggregation for the 15-minute values needs to be kept in mind in case of deciding to use the station data at high resolution. The gaps of each station itself were filled with data from the nearest neighbour. We then calculated Voronoi polygons (Fig. 2.2.1) and determined the surrounding stations that represent each catchment by different percentages.

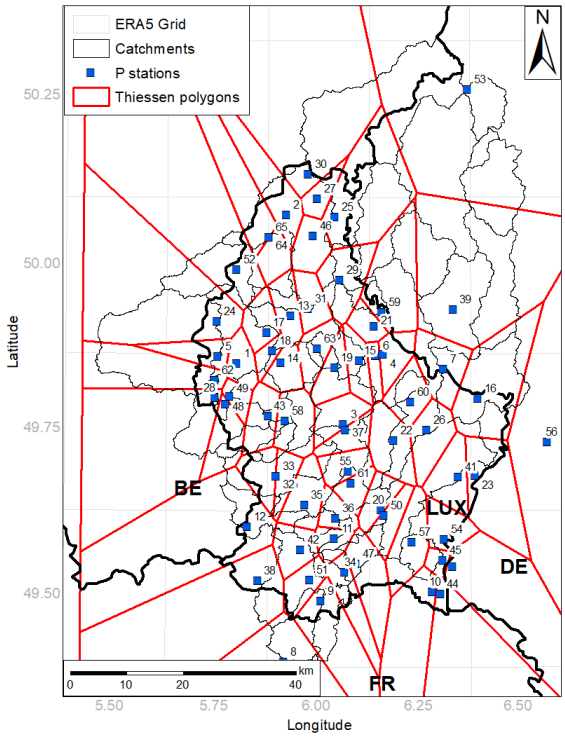

Figure 2.2.1: Precipitation stations and Thiessen polygons for the interpolation to the catchments.

2.2.3 Atmospheric data

The ERA5 reanalysis data was downloaded from the Copernicus Climate Data Store (CDS). We extracted parameters of atmospheric data at single levels (Hersbach et al., 2023b) as well as at different pressure levels (Hersbach et al., 2023a) and some land data (Muñoz Sabater, 2019). The specific parameters are listed in Table 2.2.1 and represent different aspects of thunderstorm formation, such as high atmospheric instability and a high moisture content. In addition, wind speeds and shear winds should be low, to allow a slow storm motion and good organisation so that a large amount of rainfall accumulate over a specific area. These atmospheric conditions are considered extreme precipitation and potentially flash flood favouring (Meyer et al., 2022).

The spatial resolution of the atmospheric ERA5 grid cells is $0.25° \times 0.25°$, and of the ERA land data $0.1° \times 0.1°$. To translate the data to one time series per catchment, the catchment shapes were cut out from the grid cells and the values of the grid cells within the catchments were averaged respecting the percentage of the area of each grid cell within the catchment. A few small catchments are located within one ERA5 grid cell only (catchments: 10, 12, 13, 16, 17, 23, 36, 53, 54, 56). The original temporal resolution of the ERA5 data is at hourly rate. To disaggregate the data to the 15-minute interval of the observed discharge data of our data set, we used linear interpolation for most parameters. The values at the full hour are the original values. As the total precipitation is an accumulated value, we equally divided the hourly values for this parameter. From the original parameters, we calculated the

mean wind speed ($WS_{10\,m\ a.g.l.-500\,hPa}$, eq. 2.1) between 10 m a.g.l. and the pressure level of 500 hPa from the squared northward direction wind vector u ($m\,s^{-1}$) and the squared eastward direction wind vector v ($m\,s^{-1}$).

Table 2.2.1: Selected proxy parameters for the assessment of convection-relevant atmospheric conditions and soil moisture data from the ERA5 data set (adapted from Meyer et al., 2022).

Proxy for	Parameter	Abbr.	Unit	Level	Source
Instability	Convective available potential energy	CAPE	$J\,kg^{-1}$	Single	Hersbach et al. (2018a)
	Convective inhibition	CIN	$J\,kg^{-1}$	Single	Hersbach et al. (2018a)
	K index	K index	°C	Single	Hersbach et al. (2018a)
Moisture	Total column water vapour	TCWV	$kg\,m^{-2}$	Single	Hersbach et al. (2018a)
	Specific humidity	q	$kg\,kg^{-1}$	700 hPa	Hersbach et al. (2018b)
	Relative humidity	RH	%	700 hPa	Hersbach et al. (2018b)
Storm motion and organization	$\vec{u}$ component of wind	$\vec{u}$	$m\,s^{-1}$	10 m, 500 hPa and	Hersbach et al. (2018b)
	$\vec{v}$ component of wind	$\vec{v}$	$m\,s^{-1}$	700 hPa	Hersbach et al. (2018b)
Catchment wetness state	Volumetric soil water layer 1	Swvl1	$m^3\,m^{-3}$	0–7 cm	Muñoz Sabater (2019)
	Volumetric soil water layer 2	Swvl2	$m^3\,m^{-3}$	7–28 cm	Muñoz Sabater (2019)
	Volumetric soil water layer 3	Swvl3	$m^3\,m^{-3}$	28–100 cm	Muñoz Sabater (2019)
	Volumetric soil water layer 4	Swvl4	$m^3\,m^{-3}$	100–289 cm	Muñoz Sabater (2019)

$$WS_{10\,m\ a.g.l.-500\,hPa} = \sqrt{\frac{\left(u^2_{10\,m\ a.g.l.} + v^2_{10\,m\ a.g.l.}\right) + \left(u^2_{500\,hPa} + v^2_{500\,hPa}\right)}{2}} \tag{2.1}$$

Low-level wind shear (LLS, $m\,s^{-1}$) and deep-layer wind shear (DLS, $m\,s^{-1}$) were computed likewise to the wind speed. Yet, for the LLS (eq. 2.2), the difference

of the vectors u and v was calculated between the near ground level and 850 hPa height (approximately 1.5 km) and for the DLS (eq. 2.3) respectively, the difference between near ground level and 500 hPa height (approximately 6 km).

$$\mathrm{LLS} = \sqrt{(u_{1000\,\mathrm{hPa}} - u_{850\,\mathrm{hPa}})^2 + (v_{1000\,\mathrm{hPa}} - v_{850\,\mathrm{hPa}})^2} \tag{2.2}$$

$$\mathrm{DLS} = \sqrt{(u_{1000\,\mathrm{hPa}} - u_{500\,\mathrm{hPa}})^2 + (v_{1000\,\mathrm{hPa}} - v_{500\,\mathrm{hPa}})^2} \tag{2.3}$$

Potential evapotranspiration (eq. 2.4) was computed based on the air temperature (T) within the ERA5 data set following a method by Oudin et al. (2005). R_e (MJ m^{-2} d^{-1}) is the extraterrestrial radiation, that is derived from the Julian day, the latitude and the solar constant of approximately 0.082 MJ m^{-1}. It is divided by the latent heat flux λ (MJ kg^{-1}), that was approximated to 2.45 MJ kg^{-1}, and the density of water ρ (kg m^{-3}). The constants were set to K1=75 and K2=5. The resulting potential evapotranspiration values seem a bit low when checking the basic water balance.

$$\mathrm{ET}_{\mathrm{pot}} = \begin{cases} \frac{R_e}{\lambda\rho} \times \frac{(T+K_2)}{K_1} & \text{if } T + K_2 > 0 \\ 0 & \text{otherwise} \end{cases} \tag{2.4}$$

2.3 Catchment characteristics of Luxembourg and surroundings

2.3.1 Regional context

Luxembourg lies in central western Europe, bordering France, Belgium and Germany (Fig. 2.3.3). The country is characterized by two geographic regions with largely differing characteristics: The Oesling region in the North and the Gutland region in the South of the country. The Oesling forms a part of the Ardennes massif, with a schistose and steep bedrock geology. The area hosts only few settlements and a substantial forested part. The Gutland, in contrast, is characterized by soft valleys in sandstone and marl that form the basis for extensive agriculture and urban areas. The 60-80 m thick sandstone formation marks the Eastern limit of the Paris basin and holds an extensive aquifer (Bintz and Muller, 1965; Lucius, 1948). In the East of Luxembourg, the Moselle valley marks the border with Germany. The valley offers milder climatic conditions perfectly suited for viticulture.

2.3.2 Climate

The relatively homogeneous climate of Luxembourg is characterized by westerly atmospheric circulation coming from the Atlantic (Pfister et al., 2000) and classified as a temperate oceanic climate (Kottek et al., 2006). The mean annual rainfall is 700-900 mm (this data set (2003-2020), Pfister et al., 2005, (1971-2000)) and spreads almost equally throughout the course of a year (Fig. 2.3.1), with around 100 mm/month during the winter and 70 mm/month in the late summer (Wrede

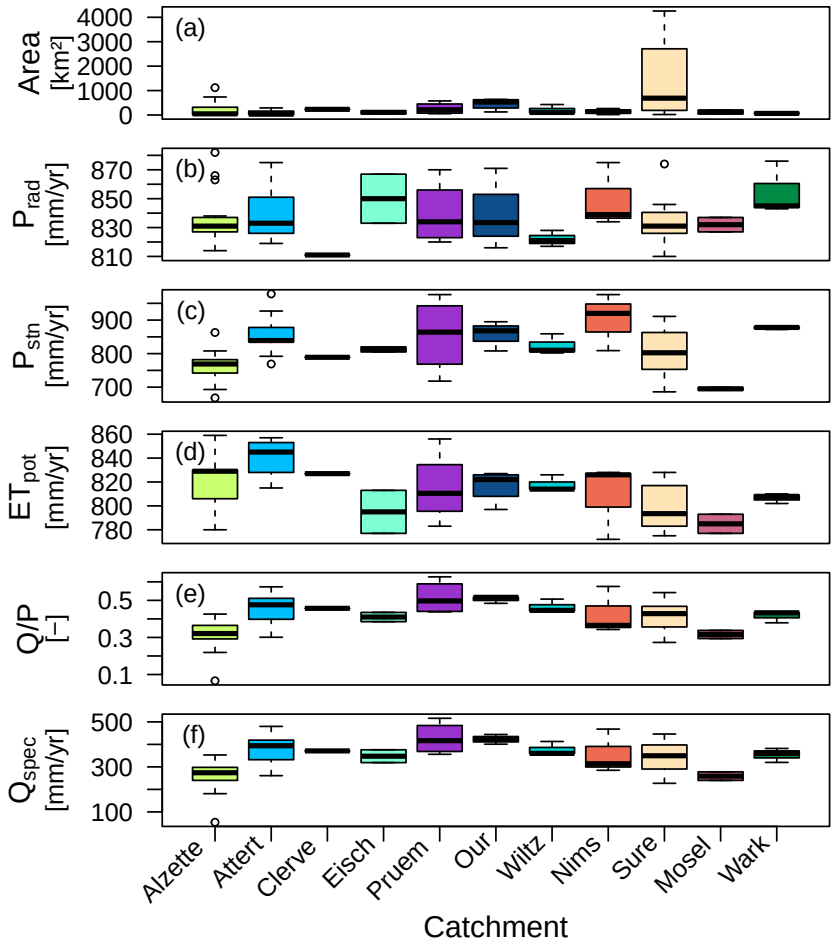

Figure 2.3.1: Water balance related catchment variables per major river basins. Subplot (a) indicates the range of the catchments sizes, (b) and (c) show the annual rainfall based on the radar product and respectively the station interpolation, (d) shows the annual potential evapotranspiration calculated according to Oudin et al. (2005), (e) shows the annual runoff ratio (Q/P) and the specific discharge (Qspec) is shown in subfigure (f).

et al., 2015). The mean monthly temperature (1971-2000) varies seasonally from about 0°C in January to 18°C in July (Pfister et al., 2005). The potential evapotranspiration (ET_{pot}) was calculated according to the air temperature based method by Oudin et al. (2005) and ranges around 800-900 mm per year (Fig. 2.3.1). These values appear a bit low, which especially shows when calculating the aridity indices (ET_{pot}/P). A cause might be slightly underestimated midday air temperature data in the ERA5 data set. The Mosel valley area is prone to heavy thunderstorms between May and August, with relatively regular daily precipitation values above 100 mm (Schmithüsen, 1940). Within the last 20 years (2001-2020), a slight increase in thunderstorm favouring conditions was observed throughout the entire country (Meyer et al., 2022).

2.3.3 Hydrology

The hydrological regime within Luxembourg is pluvial oceanic (Pardé, 1947). Typically, streamflow regimes are characterized by high water levels and flooding during the winter and low flow situations during the summer (Wrede et al., 2015). While during the period of 1980-2000 large winter floods were observed on multiple occasions (Pfister et al., 2000), they have been observed less frequently within the last 20 years. Instead, floods caused by thunderstorms in the beginning of the summer have been observed to an increasing extent between 2016-2021 (Bingenheimer, 2018; Pfister et al., 2018).

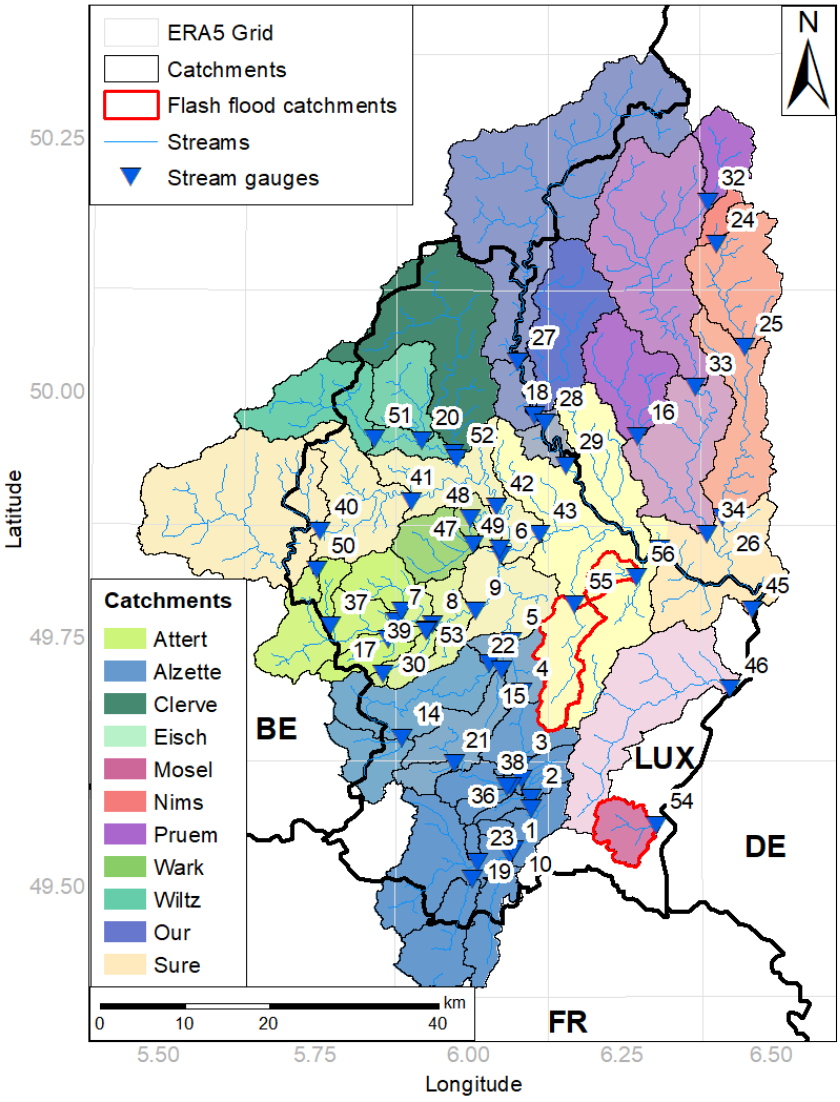

Figure 2.3.2: 56 nested catchments of CAMELS-LUX grouped in a few basins of higher order.

Luxembourg contains a nested catchment set-up of many headwater catchments, that contribute to a few rivers of a higher order (Fig. 2.3.2). These are the Attert and Wark in the West, the Alzette in the South and the Wiltz, Clerve, and Our

in the North of the country. East of the latter three on the German side are the Pruem and Nims catchments. All of these contribute to the Sure River, that feeds the Mosel at Trier, East of Luxembourg. The Syre and Aalbach river in the East of Luxembourg directly feed the Moselle. Two particular flash flood series occurred around 22 July 2016 (Pfister et al., 2018) and 01 June 2018 (Pfister et al., 2020), that especially hit the catchments of the White Ernz and Aalbach. The thunderstorms in the country, however, caused abruptly rising water levels within many others of the listed catchments as well. Another severe flooding event directly following heavy rainfall hit Luxembourg and surrounding regions in Belgium and Germany in mid-July 2021. While the rainfall triggered flash floods in Germany, the Luxembourgish streams had slower rising water levels (e.g. Kreienkamp et al., 2021). Large-scale floods during the winter occurred - among others - in the first week of January in 2010 and in January 2020.

2.3.4 Geology

Luxembourg is divided in two major natural regions, consisting of distinct geological and geomorphological features (Fig. 2.3.3 b). The northern region (called 'Oesling') covers nearly one third of the country and is a part of the Ardennes-Rhenish shield. In the southern region (called 'Gutland') Mesozoic sediments prevail and form the northeastern limit of the Paris Basin.

In the Oesling, the limited permeability of the schistous bedrock causes surface and lateral subsurface flows to dominate streamflow generation. The Gutland region is characterized by alternating layers of permeable (e.g., sandstone) and less permeable (e.g., marls) bedrock layers. The former allow a deep percolation of water towards large aquifers that eventually feed a constant baseflow component in the river network (Gourdol et al., 2023; Wrede et al., 2015). In catchments dominated by substrates with limited permeability, fast hydrological processes - such as saturation excess overland flow - dominate streamflow generation (Wrede et al., 2015). Based on geological data from Luxembourg (APC, 2022), Belgium (Hellebrand et al., 2007), France (BRGM, 2020) and Germany (BGR, 2019), five geology classes were determined, based on their hydrological behaviour and featured permeability (Pfister et al., 2017): (1) marl and claystone, (2) schists & quartzites, (3) surface deposits, (4) Limestone & dolomites, (5) sandstone & conglomerates (classes listed with increasing permeability).

2.3.5 Land use

The North of the country is widely covered by forests and cultivated land. The South has some forested area as well, but is dominated by vast areas of cultivated land and urbanised areas. The hillsides towards the Mosel valley in the East of the country are traditionally used as vineyards. Based on data from Luxembourg (MECB and MEA, 2018; EEA, 2018) land use was grouped into five classes: water bodies & wetlands, forests & natural areas, grassland, agricultural land & urban areas (Fig. 2.3.3 c).

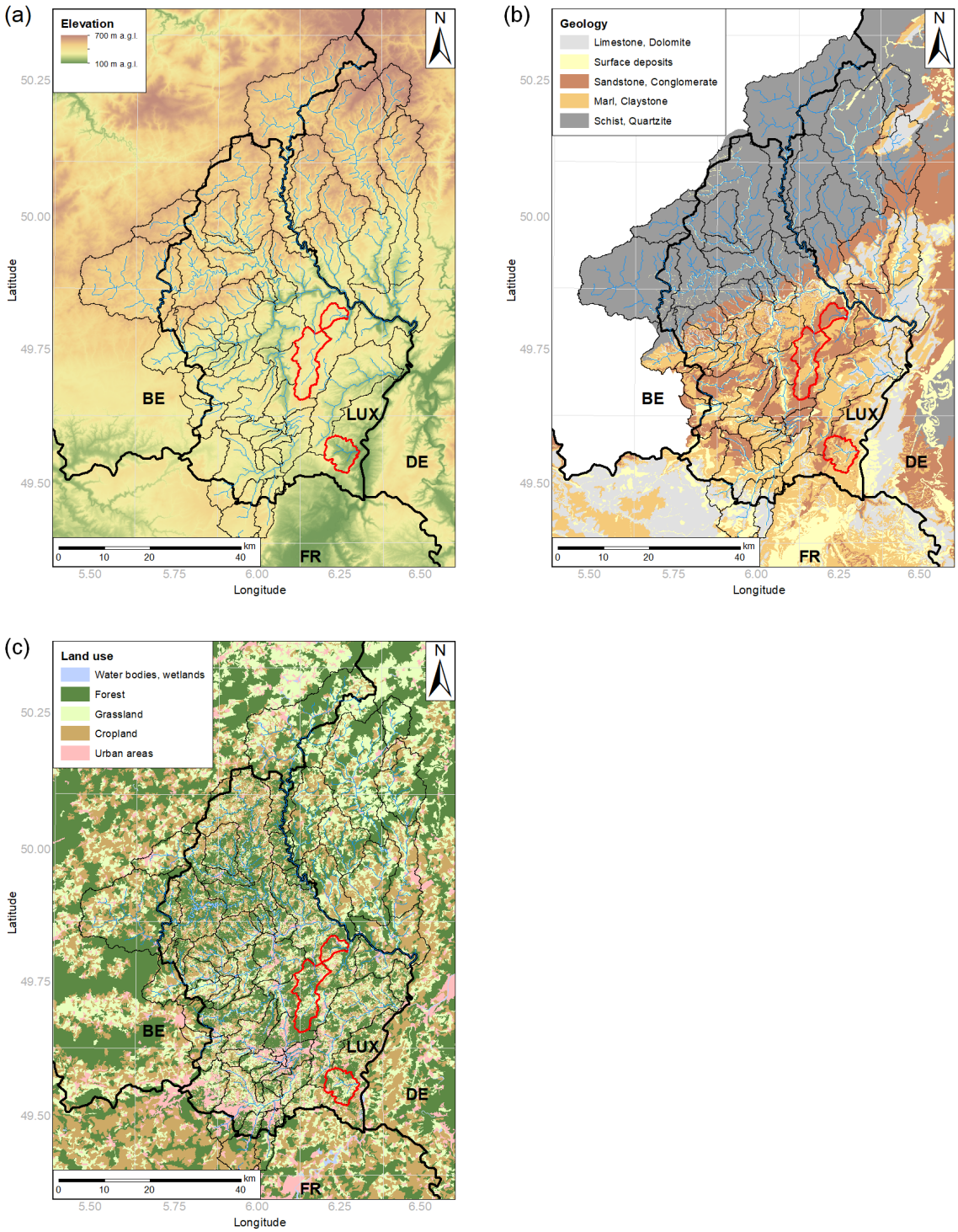

Figure 2.3.3: Physiographic settings of the catchments. (a) illustrates the topography, (b) the geology and (c) the land use of Luxembourg and its surroundings.

2.4 Topography and derived morphometric parameters

The topography of Luxembourg is shown in Fig. 2.3.3 (a). The North of Luxembourg, the Oesling region, is a mountainous region, that is a part of the Ardennes massif that extends from France to Germany. In Belgium, the Ardennes massif reaches elevations of up to 600-700 m a.s.l. (Pfister, 2012). In Luxembourg, the highest peak is reached in Wilwerdange with an elevation of 560 m a.s.l. Valleys are cut in deep V-shapes. The South of the country, the Gutland area, lies at the eastern limit of the Paris basin (Wrede et al., 2015) and ranges from approximately 100-400 m a.s.l.. Hills are softer and the landscape and U-shaped valleys are wider. The South-Eastern border of Luxembourg is defined by the Mosel valley, that is cut in deeply into the surrounding hills. An area in the central East of Luxembourg is sometimes also referred to as the "little Switzerland of Luxembourg" and is characterized by some very steep and rocky slopes.

An according 5 x 5 m digital elevation model (DEM) was constructed for the entire study area based on data from Luxembourg (ACT, 2019), Belgium (SPW, 2014), France (RGE ALTI, 2020), North Rhine-Westphalia (IT-NRW, 2021), Rhineland-Palatinate (LGV, 2021) and (Hengl et al., 2022). The catchments of the 56 stream gauges have been extracted from this DEM, using the hydrological network to ensure consistency. In addition to basic catchment characteristics (elevation, area, perimeter and slope), a few morphometric indices considered relevant are described in subsections hereafter.

2.4.1 Gravelius compactness coefficient (K_c)

As the basin shape influences the accumulation of runoff, and therefore the hydrographs of flood peaks, the Gravelius compactness coefficient (K_c) was included in the hydrologic catchment properties. Its calculation is based on the ratio of the basin's perimeter and the perimeter of a circle of the catchment's area (eq. 2.5). K_c values close to 1 indicate a circular catchment shape. The roundest catchment of this data set is the Weierbach (ID 50) with $K_c = 1.133$. The larger K_c values are, the more elongated a catchment is (Gravelius, 1914). In this data set the highest $K_c = 2.202$ is calculated in the Sure catchment at Bollendorf (ID 44).

$$K_c = \frac{\text{Perimeter}}{2\sqrt{\pi \times \text{Area}}} \tag{2.5}$$

2.4.2 Index of Development and Persistence of the river networks (IDPR)

The Index of Network Development and Persistence of the river network (IDPR) was incorporated in the data set as an assessment tool for infiltration capacities of the soil or ground. It can moreover be considered a proxy for the catchment's drainage density making it an indicator for both topographic and hydrological catchment

properties (Mardhel et al., 2021; Uhan et al., 2004). The IDPR quantifies the discrepancy between the observed natural river system and a theoretical hydrographic network calculated only from a DEM for a given accumulation threshold (set to 62.5 hectares in this study). The IDPR is therefore the ratio of the shortest distance following the steepest slope of a point considered to (a) the theoretical river system and (b) the actual river system. Originally this ratio was arbitrarily multiplied by 1000 and limited to a maximum value of 2000 (Mardhel et al., 2021). A transformation of this ratio into a logarithmic value (base 10) was preferred in this study (eq. 2.6). Negative values indicate areas prone to infiltration, while positive values indicate areas that favour surface runoff. The index indicates that the closer the value is to 1, the less infiltration occurs within a catchment. The IDPR is often in agreement with the fraction of a priori impermeable geologic formations in the basin. The range of the catchments´ mean IDPR in this data set reach from -0.501 (Kaylbach, ID 19, mainly limestone and dolomites) to 0.615 (Weierbach, ID 50, schist). The latter value hints to an important weakness of the index: Other than indicated by the IDPR, the Weierbach is characterized by one of the highest infiltration rates of all considered catchments. This is linked to a high permeability of the soil, that is not represented in the slopes of the DEM and therefore not considered by the IDPR.

$$\mathrm{IDPR} = 10^{\frac{a}{b}} \tag{2.6}$$

The Topographic wetness index (TWI) was developed by Beven and Kirkby (1979) and is an index for the spatial variation of soil moisture within a catchment. Its calculation (eq. 2.7) is based on the upstream contributory area (topographic area drained at the point considered) (α) and the local surface slope in radian (β). TWI values provide information about the ability of a point to accumulate water as a function of the amount of water flowing in and escaping from it. An area with high TWI values is characterized by an increased potential for accumulated runoff and therefore a higher probability of getting saturated. On the other hand, sectors with steep slopes and close to ridgelines will have a TWI close to zero. In this data set, TWI catchment means range from 5.846 (Huewelerbach, ID 17) to 7.146 (Eisch, ID 14).

$$\mathrm{TWI} = \ln\left(\frac{\alpha}{\tan\beta}\right) \tag{2.7}$$

2.4.3 Vector Ruggedness Measure (VRM)

Terrain roughness is characterized in this data set by the Vector Ruggedness Measure (VRM) index. It measures the dispersion in three dimensions of orthogonal vectors on the terrain surface (x, y, z) and thus incorporates variability in both the aspect (β) and the slope (α). Proposed by Hobson (1972) and adapted by Sappington et al. (2007), the VRM index is dimensionless and ranges from 0 to 1. Typical values for natural soils vary between 0 and 0.5. Rugged landscapes are defined by values greater than 0.01-0.02. Here, mean VRM values at the catchment scale range from 0.001 (Wollefsbach, ID 53) to 0.011 (Enz, ID 16).

$$\mathrm{VRM} = 1 - \frac{|r|}{n} \tag{2.8}$$

with

$$|r| = \sqrt{\left(\sum x\right)^2 + \left(\sum y\right)^2 + \left(\sum z\right)^2} \tag{2.9}$$

$$z = 1 \times \cos(\alpha) \tag{2.10}$$

$$xy = 1 \times \sin(\alpha) \tag{2.11}$$

$$x = xy \times \sin(\beta) \tag{2.12}$$

$$y = xy \times \cos(\beta) \tag{2.13}$$

2.5 Catchment behaviour

Luxembourg's nested catchment set-up is prone for studying the influence of the underlying bedrock. While the climate is relatively constant throughout the country, the geology varies to a high extent. Bedrock geology controls both, the streamflow regime and the catchment storage. This was shown in detail in a study with a subset of 16 Luxembourgish catchments (Pfister et al., 2017; Wrede et al., 2015). The dominant geology classes in Luxembourg are represented in small and relatively homogeneous headwater catchments, such as the Wollefsbach (ID 53), that purely consists of marls, the schistose Weierbach (ID 50), and the sandstone based Huewelerbach (ID 17) (Wrede et al., 2015). The marl catchments react fast and highly seasonal. As marl is impermeable, lateral subsurface flow dominates the runoff reaction, that often follows preferential pathways to be even faster. Depending on the current soil moisture conditions, saturation excess overland flow adds to the runoff. The catchments in schist are also characterized by a strong seasonality and subsurface lateral flow. Uneven bedrock surfaces lead to a 'fill and spill' mechanism, that is activated during higher soil saturation. The fast runoff reaction if likely caused by overland flow in saturated riverine areas. These two processes sum up to the Weierbach's typical double peak pattern (Hissler et al., 2021). The highly permeable sandstone formations allow deep percolation and form an immense storage reservoir, that feeds the streams with a nearly constant baseflow throughout the year (Wrede et al., 2015).

In Fig. 2.5.1, we provide an impression of the meaning of the morphologic parameters in comparison to the geology classes, in which the catchments were grouped. Regarding the topographic wetness index (Fig. 2.5.1 a), we can see that catchments with a high percentage of marl and claystone have a higher TWI than catchments that are mainly situated in schist and quarzite or sandstone and conglomerate. The IDPR shows higher values, when the impermeability is higher and lower values for a higher permeability (Fig. 2.5.1 d). As the index is a tool for infiltration capacities.

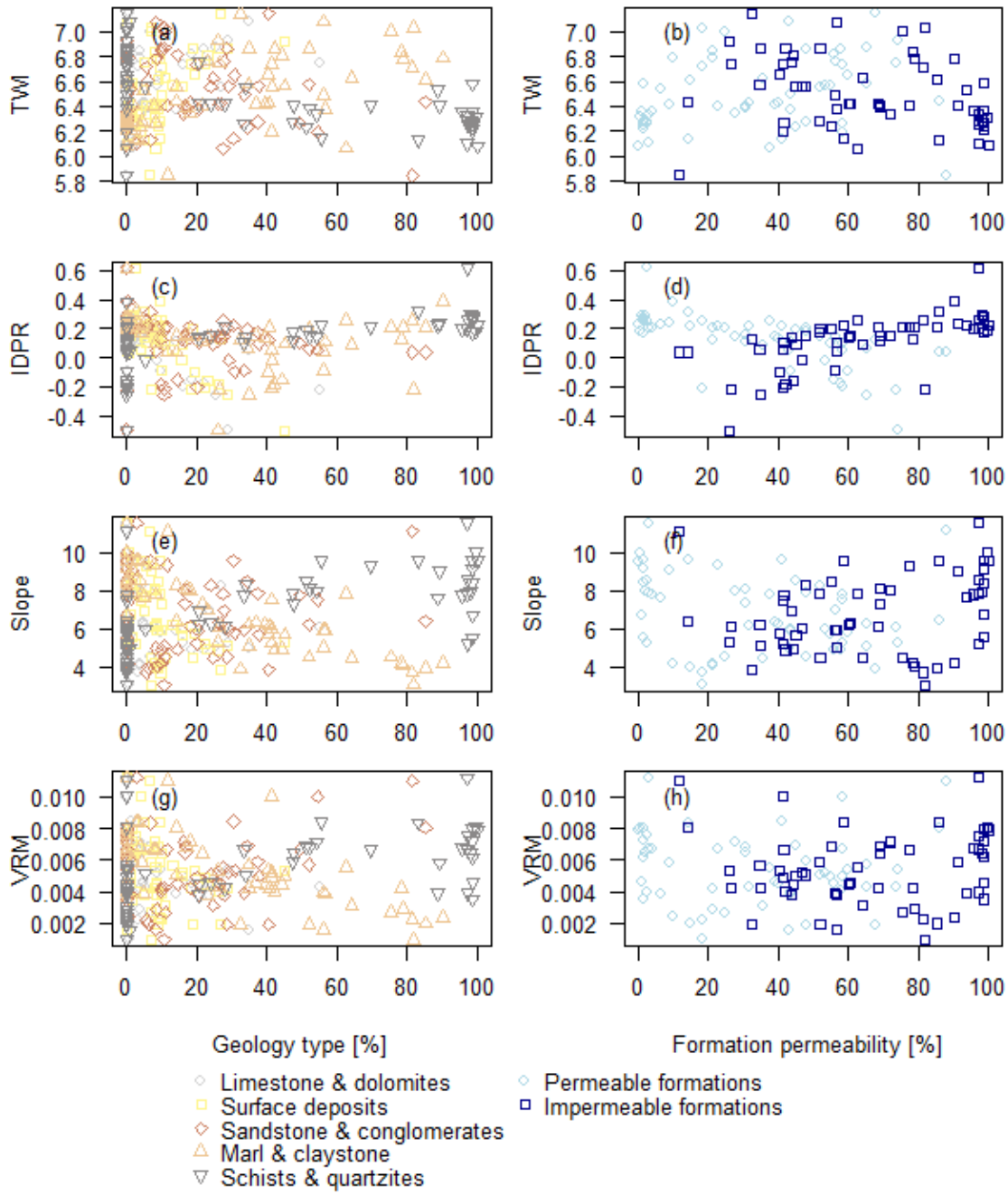

Figure 2.5.1: Morphologic parameters in comparison to the percentage of geology within a catchment.

Regarding the slope (Fig. 2.5.1 e), we can see that the softer geology structures have the flatter (U-shaped) slopes, compared to the steep (V-shaped) slopes in the schist geology. This is coherent with the surface roughness that is lower in the marl areas compared to the schist areas (Fig. 2.5.1 g). Also land use is practised according to the topography and geology. In the schistose areas, forests cover the often steep hills and agriculture is practised on the plateaus. Contrarily, in the South of the country, agriculture is performed in the valleys on marly ground, where the sandstone opened

wide U-shaped valleys. Forests remain on the sandstone plateaus.

We would moreover like to briefly emphasize on a few catchments that exhibit peculiar hydrological behaviour. Due to its very permeable sandstone bedrock, the Huewelerbach (ID 17) has an exceptionally high storage capacity, leading to substantial volumes of water percolating to deep groundwater bodies. At the interface between permeable sandstone and less permeable marls, springs provide a continued and very stable baseflow contribution to the Huewelerbach. The Kaylbach (ID 19) and the Dudelingerbach (ID 13) are catchments, that have been strongly influenced by mining activities in the past. Baseflow continues to be sustained by pumping of water infiltrated into flooded mining galleries. The catchment reacts to strong summer rainfall events, essentially generated by rapid surface and subsurface flows. The Pétrusse (ID 31) catchment is a telling example of rainfall-runoff responses proper to urbanized catchments. The City of Luxembourg covers approximately one third of the catchment, contributing to a flashy response to intense rainfall events (leading occasionally to so-called first-flush pollution events).

2.6 Data set application

2.6.1 Atmospheric parameters characterizing thunderstorms

This data has been collected to allow a comprehensive overview over Luxembourg´s Hydrometeorology in the past decades. The driving motivation lies in the analysis of flash flood occurrences, that have accumulated in 2016 and 2018 and we are keen to figure out any relations to a changing climate. The atmospheric parameters in this data set have been chosen as proxies for atmospheric conditions that have the potential for the development of rain-intense thunderstorms. The parameters can be classified in three groups that are considered the ingredients for thunderstorm development: high atmospheric moisture, sufficient atmospheric instability, and slow wind speeds to keep the system motion low and allow the system to dump all its rain over one area. This combination can potentially trigger flash floods. The long-term trends (1981-2020) of these parameters were studied in Chapter 4. Significantly increasing trends were found in the proxies for an abundant atmospheric moisture content (specific humidity, q, and total column water vapour, TCVW). Yet, relative humidity decreased slightly. These results follow the Clausius-Clapeyron relation and are related to higher air temperatures, that allow a higher absolute amount of water content in the air, yet, in relative measures, this increase is levelled out. Moreover, the proxy parameters representing instability (convective available potential energy (CAPE) and the K index) have increased between 1981-2020. Yet, also convective inhibition (CIN) has increased, which controls the gains in CAPE (Taszarek et al., 2021a). Parameters referring to the system motion and organization have remained unchanged. Trends were especially strong within the second half of the time period, from 2001-2020. This corresponds approximately to the time span of this data set (2004-2021). This data set is moreover used for the set-up of a databased regional model for Luxembourg. The inclusion of atmospheric data in the modelling process will allow the identification of thunderstorm favouring atmospheric conditions. This

indication can give additional hints to the origin of possible high flows, even, if they somehow fall through the raster of precipitation measurements. The regional characterization of catchments also opens opportunities for the simulation of catchments, that only contain a few years of data. This is the case in the catchments in which flash floods have occurred in 2016 and 2018. These are therefore of special interest to us.

2.6.2 Benchmark model LSTM

Model setup and training

To provide a reference for model intercomparison studies, a benchmark Long-Short-Term-Memory (LSTM) model for Luxembourg was added to this data set. This benchmark model utilizes all dynamic time series and a selection of physiographic catchment characteristics as input features (Appendix 2.7.1).The LSTM hyperparameters were selected based on literature references (Espinoza et al., 2023). For the daily data, a sequence length of 365 days was chosen to reflect the annual hydrological cycle. The model includes one LSTM layer that is coupled with a linear head layer, both with a hidden size of 64. It was trained to optimize the area-averaged Nash-Sutcliffe efficiency over 30 epochs with a batch size of 256, with a dropout rate of 40% and an initial learning rate of 0.0001. The learning rate was adjusted by a gamma rate of 0.8 every five epochs. The forget gate was initially set to a value of 3. More details about the LSTM are described in Chapter 5 and Espinoza et al. (2023). For an overview of how LSTMs function in hydrology, please refer to Kratzert et al. (2019b).

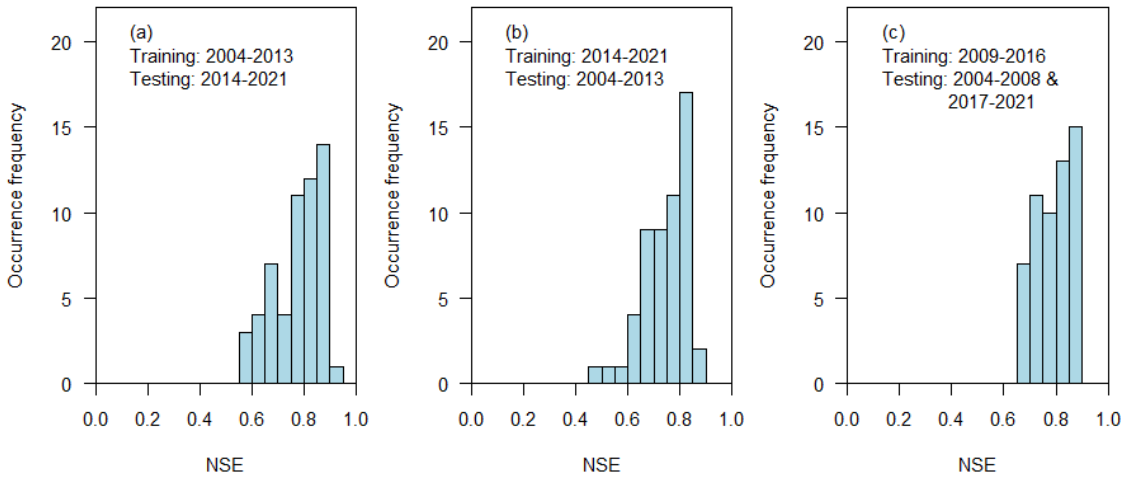

Figure 2.6.1: NSE distribution of the 56 catchments during 3 different model runs with varying testing and training periods. Subplot (a) was trained on data from 2004-2013 and tested on data from 2014-2021. Subplot (b), respectively on the inverted periods. Subplot (c) was trained on data from 2009-2016 and tested on the time periods before and after that. This period from 2009-2016 was chosen to include a series of flash floods that is present only in the second half of the data.

General evaluation of the LSTM performance

With these hyperparameter settings, the model achieved efficiencies in the test periods with a Nash-Sutcliffe Efficiency (NSE) ranging from 0.4 to 0.9, varying based on the choice of testing and training periods as well as different training runs (see Fig. 2.6.1). Fig. 2.6.2 shows the spatial distribution of the NSE values. One catchment that is particularly challenging to simulate with this LSTM, as well as other hydrological models (Wrede et al., 2015), is the Huewelerbach (ID 17), which is presumed to lose groundwater to deep percolation in a sandstone aquifer. Similarly, the Kaylbach (ID 19) is difficult to simulate due to the groundwater´s infiltration into mining galleries. The weak performance being related to a non-closing water balance has also been found in highly conductive chalk or karstic aquifers in Great-Britain and Southern Texas and might - among others - also be related to insufficiently characterizing catchment attributes (Lees et al., 2021; Feng et al., 2020). The White Ernz (ID 55) and Hallerbach (ID 56) have significantly shorter periods of available data and are not always well-represented in model training, which also explains their low performance scores.

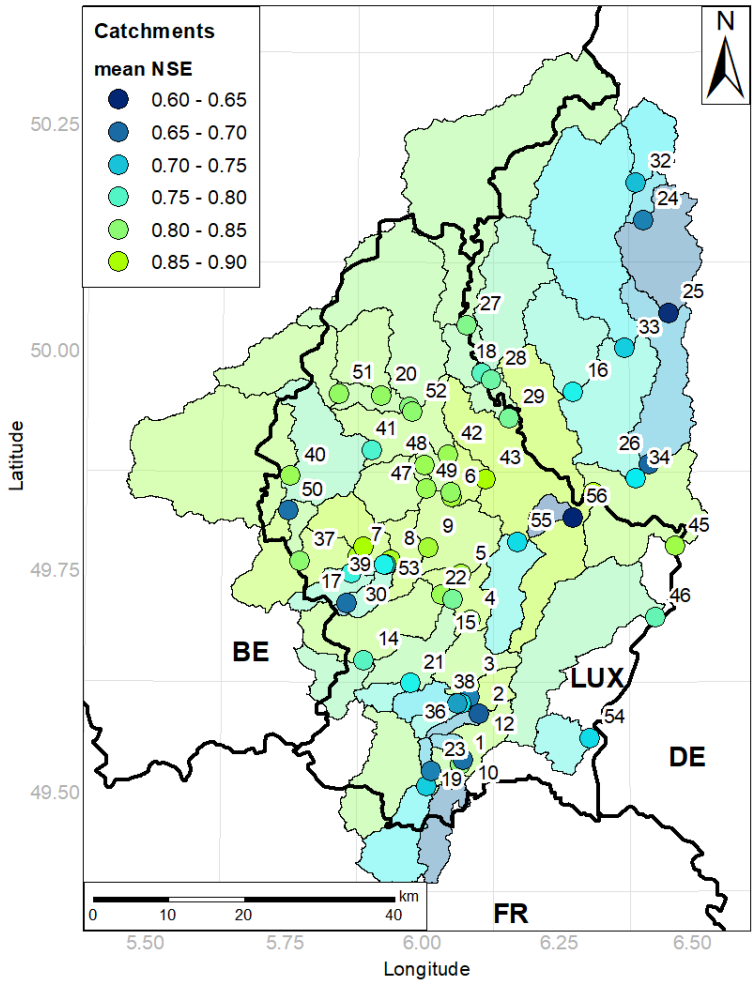

Figure 2.6.2: NSE distribution of the catchments, calculated from the mean of the three model runs.

Evaluation in dependence of the static catchment characteristics

Larger catchments reach NSE values at the upper end of the range, while there is a wide spread of NSE values in smaller catchments (0-100 km^2) (Fig. 2.6.3 a, b). The NSE is moreover higher in catchments, with a higher elevation range and a higher mean slope (Fig. 2.6.3 d, e). The second row of Fig. 2.6.3 (f-j) shows the model performances depending on the five different geology classes and the third row (k-o) the ones depending on the five different land use classes. Regarding the wide spread of NSE values, we draw the conclusion at this point, that the performance of the LSTMs is not dependant on the either of them.

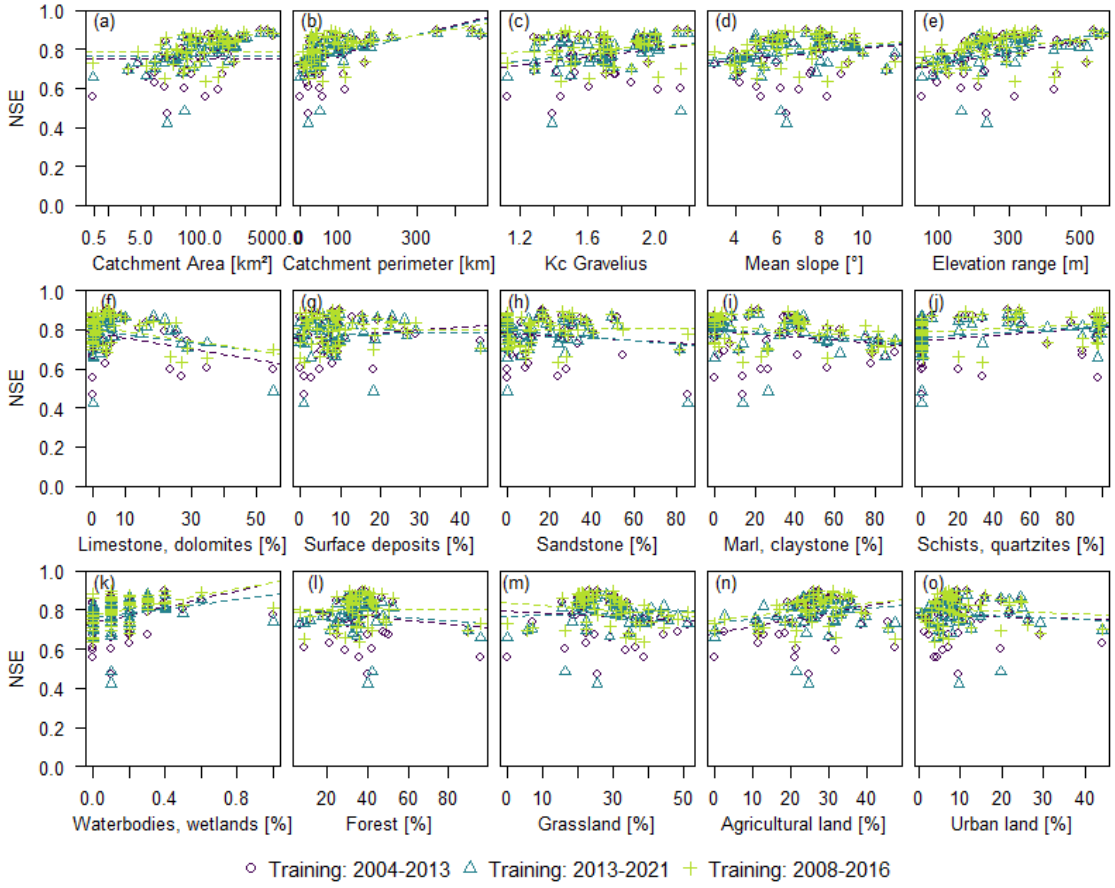

Figure 2.6.3: Links between the general model performance as evaluated by the Nash-Sutcliffe Efficiency (NSE) and differing static catchment characteristics. Note the logarithmic horizontal axis in subplot (a). The subplots (a)-(c) include catchment meta data, such as area, perimeter and shape, (d) and (e) address topographic properties. The second row (f)-(j) displays the effect of a catchment´s differing percentage of the five geology classes, while the third row (k)-(o) refers to the five land use classes.

However, the model evaluation depending on catchment characteristics is likely overlain by correlations between geology, elevation, and land use. The catchments in the North of Luxembourg lie in the schistose Ardennes mountain range, where steep valleys have formed and forests dominate vast parts of the plateau. The South

of Luxembourg is characterized by alternating sandstone and marl, which form soft valleys at a generally lower elevation. The major land use type is related to agriculture and urban areas. As storage-controlled floods during winter are simulated more precisely than summer peak flows, we had anticipated, that catchments with large storage capacities (i.e. sandstone) would be easier to simulate for the LSTM model than catchments with higher surface runoff components and flashier character. This is however not the case.

Conclusion

We have succeeded in setting up and training a regional model for Luxembourg and can clearly validate our hypothesis "LSTMs are capable of simulating discharge across catchments with varying physiographic settings in and around Luxembourg". It is the first time that simulations have been made in many of the small catchments achieving reasonable results (NSE ranging between 0.4 and 0.9). For standard forecasting applications this model could surely be beneficial leaving room for further optimization.

2.7 Appendix

2.7.1 Benchmark model settings - LSTM-LUX

Table 2.7.1: LSTM model settings: Time series, static catchments attributes and hyperparameters.

	Abbr.	
Dynamic time series	Qflag, RR_rad, RR_min_rad, RR_max_rad, RR_flag_rad, RR_stn, tp, t2m, etpot, cape, cin, kx, q, rh, tcwv, ws10500, lls, dls, swvl1, swvl2, swvl3, swvl4	
Static catchment attributes	Area_km2, Kc_Gravelius, limestone_dolomites, surface_deposits, sandstone_conglomerates, marl_claystone, schists_quarzites, watercourses_waterbodies_wetlands, forests_naturalareas_grassland_agricultural_land, urban, Z_RANGE, IDPR_MEAN, SLOPE_MAX, TWI_MEAN, VRM_MEAN	
Hyperparameters	Time step	daily
	No. of layers	1
	Sequence length	365
	Hidden size	64
	Batch size	265
	No. of epochs	30
	Drop out rate	0.4
	Learning rate	0.001
	Adapt learning rate epoch	5
	Gamma adapt learning rate	0.8
	Forget gate	3

3

The Fluctuations of Atmospheric Mesoscale Circulation Patterns Sustaining Major Precipitation

To get a first, general understanding of the atmospheric factors driving major precipitation and flooding events, we zoomed out of the Greater Region of Luxembourg and analysed mesoscale circulation patterns. This allowed us to place events in the atmospheric context and distinguish between the differing characteristics of summer and winter events. The predictability of large-scale storage-controlled winter floods is opposed by the high dynamic and local occurrence of thunderstorm-triggered summer floods. Correlating these events with the prevailing zonal and meridional circulation patterns adds understanding to the origin of the atmospheric moisture sustaining extreme precipitation and the energy needed for the development of thunderstorms. This, in turn, builds the basis for drawing conclusions about changing climate conditions triggering extreme hydrological events.

Parts of this chapter were presented at:

Meyer, J., Douinot, A., Zehe, E., Tamez-Meléndez, C., Francis, O., and Pfister, L.: Impact of Atmospheric Circulation on Flooding Occurrence and Type in Luxembourg (Central Western Europe), EGU General Assembly 2020, Online, 4–8 May 2020, EGU2020-13953, doi: 10.5194/egusphere-egu2020-13953, 2020.

Author contribution:

JN and LP designed the study. JN wrote the first draft. LP contributed to and edited the chapter.

3.1 Introduction

During the late 1980s until the late 1990s, westerly atmospheric circulation patterns dominated the hydrological systems in central Western Europe, triggering several consecutive large-scale storage-controlled winter floods (Pfister et al., 2000; Bouwer et al., 2008; Mansell, 1997). However, within recent years, especially in 2016 and 2018, rain-intense thunderstorms have triggered flash floods peaking within only a few hours in Luxembourg and neighbouring regions (Pfister et al., 2018, 2020; Johst et al., 2018). As opposed to typical winter floods, flash floods are not associated with predictable zonal circulation patterns. However, floods of either characteristic can be considered an integration of atmospheric mesoscale circulation patterns.

Atmospheric circulation patterns at a regional or continental scale have been classified in weather patterns – typically based on geopotential heights or sea level pressure. Classifications like these are applied to translate atmospheric flow patterns into the actual weather conditions that usually last a few days before transitioning to the next (Fleig et al., 2011; James, 2007). While synoptic flow patterns can be determined on a continent-wide scale, the ground weather conditions can vary substantially in different regions (James, 2007). Numerous weather classification systems have been developed and can be categorized in two groups: subjective and objective weather classifications. Subjective weather classifications, such as the Hess and Brezowski weather type classification for central Europe (Hess and Brezowsky, 1977) or the Lamb Weather Type classifications for the British Isles (Lamb, 1972), are determined by a specialist analyzing the steering synoptic situation (Huth et al., 2008). Contrarily, objective weather classifications such as the objective weather type classification (OWTS) by the German Weather Service (Bissolli and Dittmann, 2001) make use of numeric algorithms and are always reproducible.

One of the most extensively used conceptual weather type classification systems for central Europe is the subjective weather type classification by Hess and Brezowsky (Hess and Brezowsky, 1977; James, 2007). This weather type classification concept has originally been elaborated by Baur et al. (1944). Later, the concept was further developed by Hess and Brezowsky (1952, 1969, 1977), before it was brought to its current definition by Gerstengarbe et al. (1999), that is being perpetuated by the German Weather Service (DWD, 2024b). The Hess and Brezowsky weather patterns are classified in 29 intuitively named categories that represent experienced weather spells (James, 2007). The circulation form is based on the location of high and low pressure, ridges and troughs at the 500 hPa level as well as the stretch of the frontal zones (Gerstengarbe et al., 1999; Bouwer et al., 2008). To account for the early years 1881-1938, where only ground level pressure data was available, the pressure patterns at sea level were equally taken into account (Gerstengarbe et al., 1999; James, 2007).

Different weather patterns naturally imply differing hydrological consequences. Zonal circulation types, that bring humid air masses from the Atlantic to the European mainland often involve large-scale steady rain (Gerstengarbe et al., 1999). These weather types are therefore highly correlated with high winter river discharge in receiving basins in Europe (Pfister et al., 2000; Bouwer et al., 2008; Mansell, 1997). Localized heavy precipitation storms in summer often occur during meridional flows with incoming atmospheric flows from the South. These warm air masses

from the Mediterranean have the potential to destabilize the atmosphere and trigger convective precipitation events (Van Delden, 2001). Droughts, on the other hand, are observed during weather patterns related to high pressure systems above the affected region or connected to flow directions coming from land areas (Fleig et al., 2011).

Pfister et al. (2000, 2004) had investigated the effects of rainfall structure and atmospheric circulation variability on streamflow in the Alzette River basin (Luxembourg). They identified a local-scale sensitivity of river discharge to large-scale changes in atmospheric circulation, with a marked increase in precipitation related to westerly atmospheric circulation types. The latter were significantly correlated to an increase in rainfall intensity and duration that had induced an increase in winter maximum daily discharge in the Alzette River basin since the 1970s. Here, we leverage the two decades of additional precipitation and streamflow data that have been recorded since 2000 and test the hypothesis that the strong correlation between atmospheric circulation types and winter discharge observed in the second half of the 20^{th} century for central Western Europe still prevails today.

Regarding the accumulation of flash flood events in the period between 2016 and 2021, we further hypothesize that the recent accumulation of extreme precipitation and flash flood occurrences in central Western Europe is triggered by a change in atmospheric circulation patterns. We thereby aim to improve the understanding of hydro-climatological processes implying mesoscale atmospheric situations and hydrological processes generating flooding events in central Western Europe.

3.2 Study area and data

Our study area is the Moselle river basin in central Western Europe covering parts of Germany, France and Luxembourg (Fig. 3.2.1). Spanning a reasonably long period of data from 1954 to 2018, we had to rely on station data at a daily temporal resolution. For seasonal analyses, the data has been split in two groups: Summer (May-September) and winter (October to April). The range of the summer months was chosen based on the potential occurrence time of flash floods in the study area (Marchi et al., 2010).

Daily precipitation data was collected for 98 stations located in Germany (DWD), France (MétéoFrance) and Luxembourg (AGE, ASTA, LIST, MétéoLux) (Fig. 3.2.1). Based on the warning levels of the German Weather Service for heavy storms that lie within the range of precipitation amounts exceeding 40 l/m^2 in 1 hour or exceeding 60 l/m^2 in 6 hours (DWD, 2024a), we chose a threshold value of 50 mm/d to define an extreme precipitation event. Here, precipitation events are defined per station, that exceeded the daily precipitation amount of 50 mm/d. A large-scale precipitation event that exceeds the threshold at several stations is therefore counted as often as the number of stations exceeding 50 mm/d. While this adds a bias in favour of large-scale precipitation events, this weighting of larger events accounts for potentially more severe overall hydrologic situations.

We analysed streamflow data from three stations located in Luxembourg: Winseler (Wiltz), Ettelbrück (Alzette) and Gemünd (Our) (Fig. 3.2.1) from 1955-2021.

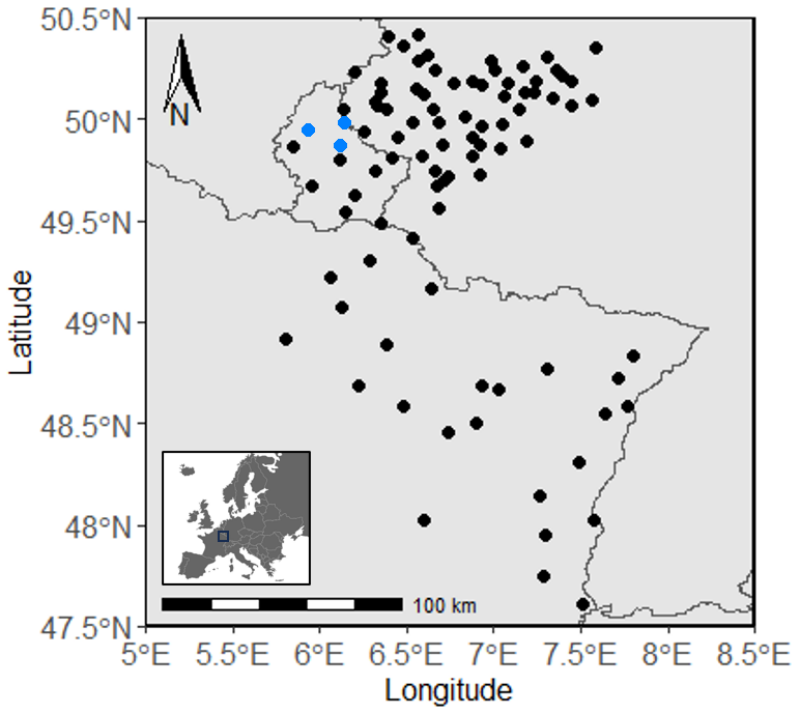

Figure 3.2.1: Study area with climate stations (black dots) and stream gauges (blue dots).

While the data is available only at a daily resolution from 1955 to 1996, streamflow is recorded at a 15-minute resolution since 1996. As flash floods often occur in small streams, or even outside streams at temporal scales of less than a day, we relied on a compiled inventory of flash floods described in Subsection 4.2.2 and Table S3.1.

To reflect upon the atmospheric circulation patterns that trigger extreme precipitation events as well as flash floods and stream flow peaks, we rely on the weather pattern classification by Hess and Brezowsky (1977). The 29 weather patterns and the one transitional class are listed in Table 3.2.1 and described in detail in Gerstengarbe et al. (1999). The weather patterns are further grouped into three overarching circulation categories (Table 3.2.1): (1) The zonal circulation, that includes atmospheric flows from West to East along which low pressure systems and frontal zones move, from the Eastern North-Atlantic to the European mainland; (2) Mixed circulation, where zonal and meridional flow components offset one another notably during a North-South air mass exchange that is strongly deviated by zonal components; (3) Meridional circulation, that often proceed from stationary and blocking high pressure systems between 50 and 65° latitude or North-South aligned trough constellations. For the analyses in this study, the weather patterns are grouped into five circulation types: Zonal West, High/Low central Europe, North and Northwest, High Scandinavia and Meridional South.

Table 3.2.1: Translated definitions of the circulation patterns by Hess and Brezowsky (1977). Translations adapted from James (2007). The circulation patterns are grouped in five circulation types (GWT): (1) Zonal West, (2) High/Low Central Europe, (3) North & Northwest, (4) High Scandinavia, (5) Meridional South.

GWL		Translated Definition	GWT
Zonal circulation form			
1	WA	Anticyclonic Westerly	1
2	WZ	Cyclonic Westerly	1
3	WS	South-Shifted Westerly	1
4	WW	Maritime Westerly (Block E. Europe)	1
Meridional circulation form			
5	SWA	Anticyclonic South-Westerly	5
6	SWZ	Cyclonic South-Westerly	5
7	NWA	Anticyclonic North-Westerly	3
8	NWZ	Cyclonic North-Westerly	3
9	HM	High over Central Europe	2
10	BM	Zonal Ridge across Central Europe	2
11	TM	Low (Cut-Off) over Central Europe	2
Meridional circulation form			
12	NA	Anticyclonic Northerly	3
13	NZ	Cyclonic Northerly	3
14	HNA	Icelandic High, Ridge C. Europe	3
15	HNZ	Icelandic High, Trough C. Europe	3
16	HB	High over the British Isles	3
17	TRM	Trough over Central Europe	3
18	NEA	Anticyclonic North-Easterly	4
19	NEZ	Cyclonic North-Easterly	4
20	HFA	Scandinavian High, Ridge C. Europe	4
21	HFZ	Scandinavian High, Trough C. Europe	4
22	HNFA	High Scandinavia-Iceland, Ridge C. Europe	4
23	HNFZ	High Scandinavia-Iceland, Trough C. Europe	4
24	SEA	Anticyclonic South-Easterly	5
25	SEZ	Cyclonic South-Easterly	5
26	SA	Anticyclonic Southerly	5
27	SZ	Cyclonic Southerly	5
28	TB	Low over the British Isles	5
29	TRW	Trough over Western Europe	5
30	U	Transition	6

3.3 Methods

To assess the long-term variability of summer and winter extreme precipitation events, the time series of the annual precipitation events were evaluated using 11-year moving averages. The precipitation occurrences and amounts were then correlated with the underlying circulation patterns to identify the ones relevant for summer and winter precipitation respectively. This correlation was then analysed over time.

To evaluate the correlation of winter peak flow and zonal circulation patterns found by Pfister et al. (2000, 2004), we followed the same protocol. At first, the maximum annual streamflow was identified. About 90% of the annual maxima occurred during winters. In the years, in which the highest event occurred during the summer, the highest winter peak flow was selected. These maximum winter daily peak flows were correlated with the annual precipitation sum during the zonal circulation patterns WZ (Cyclonic Westerly), WS (South-Shifted Westerly), SWZ (Cyclonic South-Westerly), TRM (Trough over Central Europe), and TRW (Trough over Western Europe). To identify the underlying circulation patterns during summer flash floods, we relied on the flash flood data base.

Finally, we investigated the long-term fluctuation of the circulation patterns by Hess and Brezowsky (1977) themselves to help explaining some of the accumulation of large-scale floods or summer peak flow. Focussing on the decadal variation, we used the 11-year moving average. This trend analysis was done separately for summer and winter.

3.4 Results

3.4.1 Variation of precipitation events

We analysed the number of precipitation events from 1954-2018 (Fig. 3.4.1). As the interannual variation of the number of annual precipitation events is rather high, ranging from 0 (2014) to 90 (1994), we focused on the 11-year moving average for the trend analyses. During the 1980s and 1990s, more than 40 precipitation events occurred per year, while in the evaluated decades before and after, less than 40 precipitation events occurred. The extra occurrences in the 1980s and 1990s are related to more precipitation events during the winter, while the number of precipitation event occurrences during the summers stayed rather constant.

The number of precipitation events is weighted based on the character of the precipitation event. During intensive large-scale precipitation, that typically occurs during the winter months, more stations are likely to cross the 50 mm/d threshold than during localized thunderstorm events, that occur especially in summer. This effect is shown in Table 3.4.1, where the number of stations for which the daily precipitation classified as precipitation event is compared to the number of days on which one or more stations exceeded the 50 mm/d threshold. While the number of days with precipitation events is still higher during the winter compared to the summer, the number of stations that exceed the threshold during these days is a multiple of the ones in the summer. On average, 2.3 stations surpass the threshold on

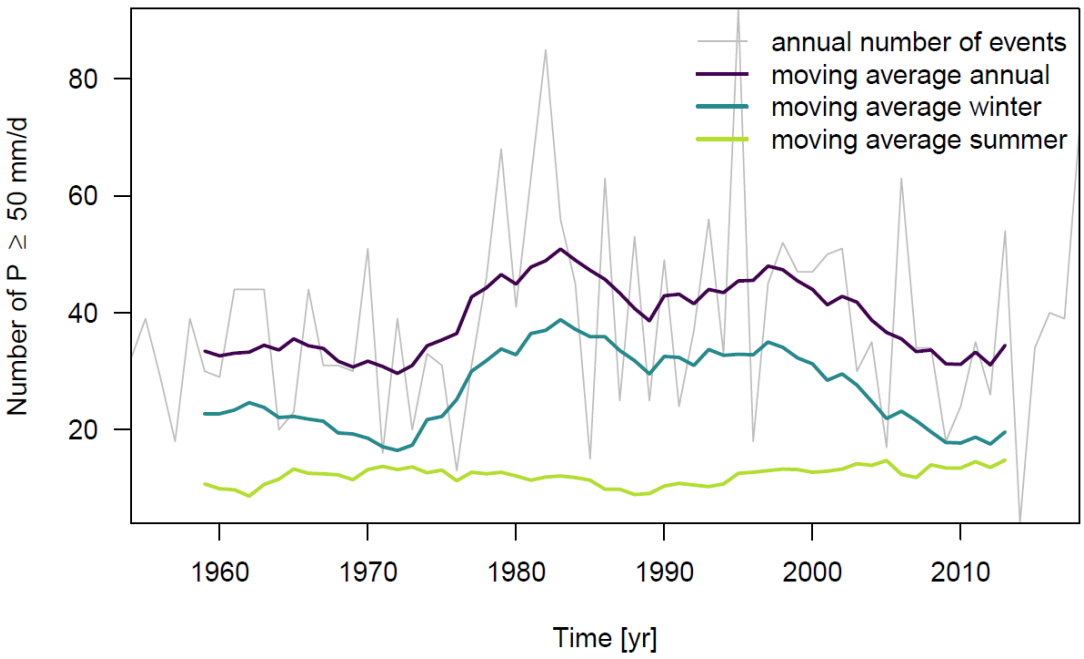

Figure 3.4.1: Annual number of precipitation events, including the 11-year moving average, split in summer and winter, to even out the interannual variations.

a high precipitation day in the summer, while it is 3.6 stations on a high precipitation day in the winter, indicating a larger scale of the events.

Table 3.4.1: Comparison of days with precipitation events and the number of precipitation events at all stations.

	All year	Summer	Winter
Sum of precipitation events $\geq$ 50 mm/d at stations	2505	800	1705
Days with precipitation $\geq$ 50 mm/d at any station	823	343	480

3.4.2 Circulation patterns during precipitation events

As indicated by the number of stations that exceed the threshold of 50 mm/d during a high precipitation day in winter (Table 3.4.1), the zonal circulation types WZ (Cyclonic Westerly), followed by WS (South-Shifted Westerly) and WW (Maritime Westerly) make up for more than 70% of the occurrence of precipitation events in winter (Fig. 3.4.2 c). The predominance of these zonal patterns in winter also affects the annual evaluation of precipitation events (Fig. 3.4.2 a). Two other circulation patterns relevant for precipitation events in winter are the Meridional circulation type SWZ (Cyclonic South-Westerly) and its Northern counterpart NWZ (Cyclonic North-Westerly), that are closely related to the Cyclonic Westerly pattern (WZ),

that causes most of the precipitation. All other circulation patterns are irrelevant regarding extreme precipitation events during the winters.

In summer (Fig. 3.4.2 b), precipitation events occur during almost all circulation patterns. With 81 occurrences throughout the entire study period, is the circulation pattern TM (Low over Central Europe), followed by WZ (Cyclonic Westerly), TRW (Trough over Western Europe) and SEZ (Cyclonic South-Easterly).

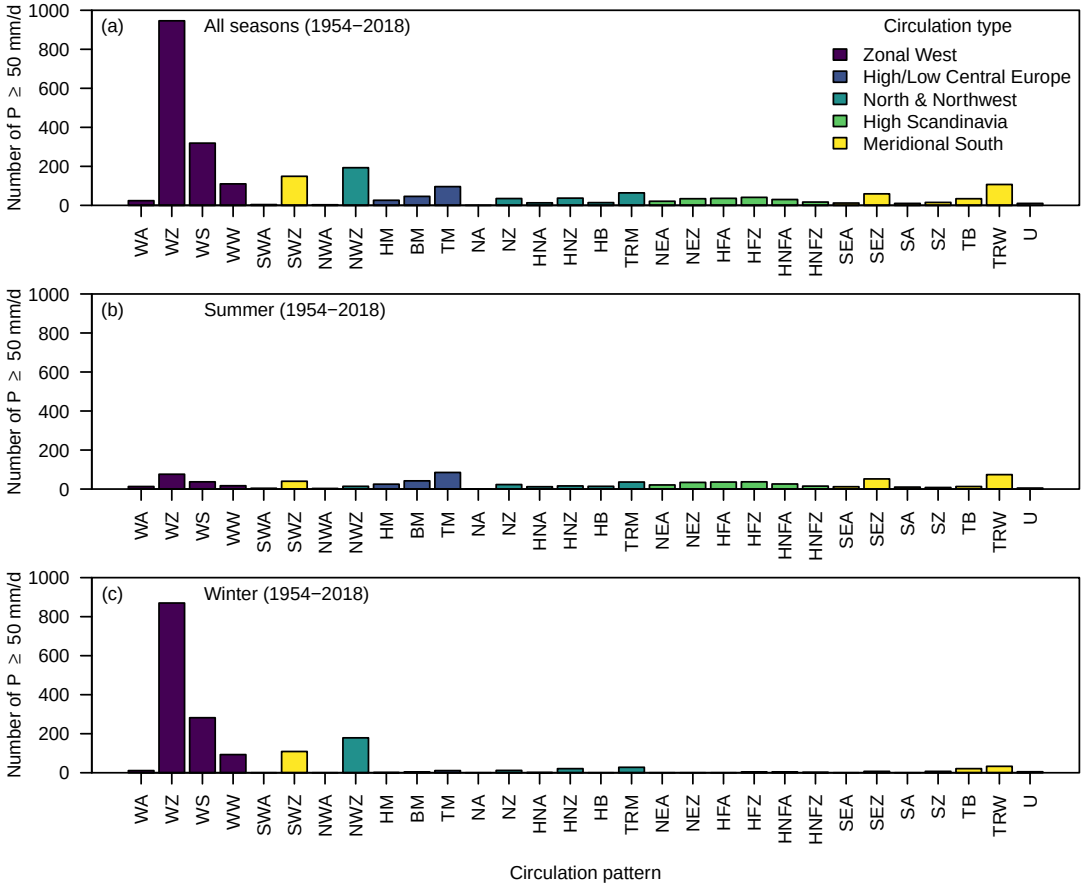

Figure 3.4.2: Circulation patterns sustaining the precipitation events throughout the year (a), in the summers (b) and during the winters (c). Note, that one precipitation event can be counted several times, if several stations were affected.

To add information to the seasonal distribution of the underlying circulation patterns causing the precipitation events, the precipitation amounts and stations affected during a precipitation event are shown in Fig. 3.4.3. This further underpins the finding, that the zonal circulation type brings the most widespread and highest precipitation events in winter. During summer, the five circulation types are almost equally distributed and all of them have the potential to generate high precipitation amounts. The highest absolute precipitation amounts are generally reached during the zonal circulation types.

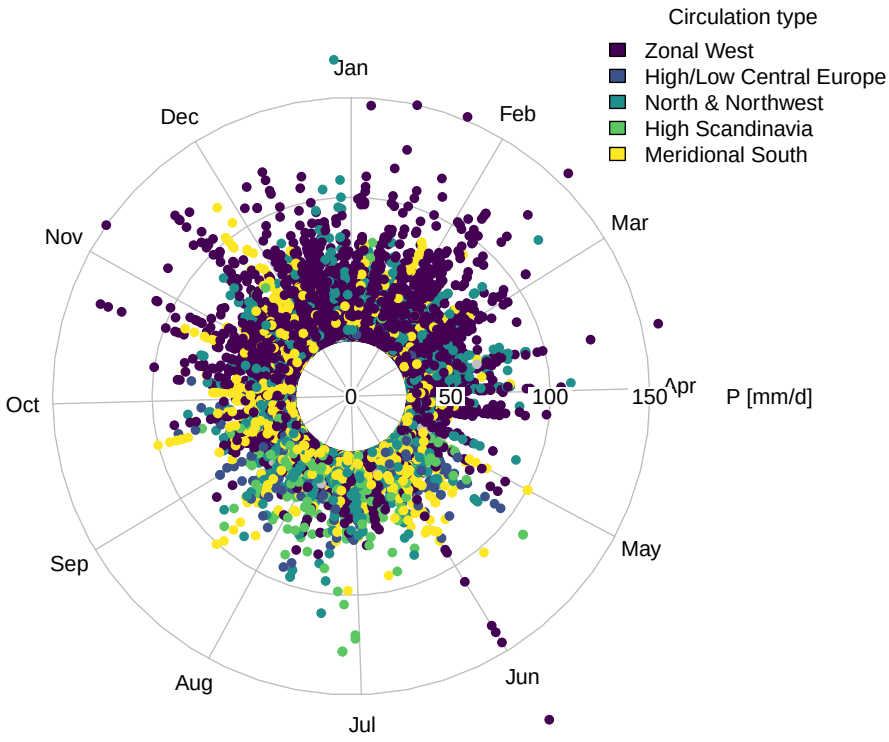

Figure 3.4.3: Interannual distribution of precipitation events between 1954-2018 coloured depending on the underlying circulation type.

3.4.3 Variation of precipitation events and related circulation types

In Fig. 3.4.4, precipitation events and their underlying circulation patterns are shown over time. While the annual maximum precipitation event totals have slightly, but non-significantly increased during the summer precipitation events (subplots a), no such trends could be identified during the winter months (Fig. 3.4.4 c). In winter (Fig. 3.4.4 c, d), the predominance of the Zonal West circulation types prevails across the entire period, with regular occurrences of the Meridional South circulation type. During summer (Fig. 3.4.4 a, b), the underlying circulation types are much more diverse. While there are no long-term trends visible, there is an accumulation of precipitation events triggered during configurations characterized by a high over Scandinavia in the 1970s. Besides this fact, we noted an accumulation of precipitation events occurring during Meridional South circulation types in the early 2000s.

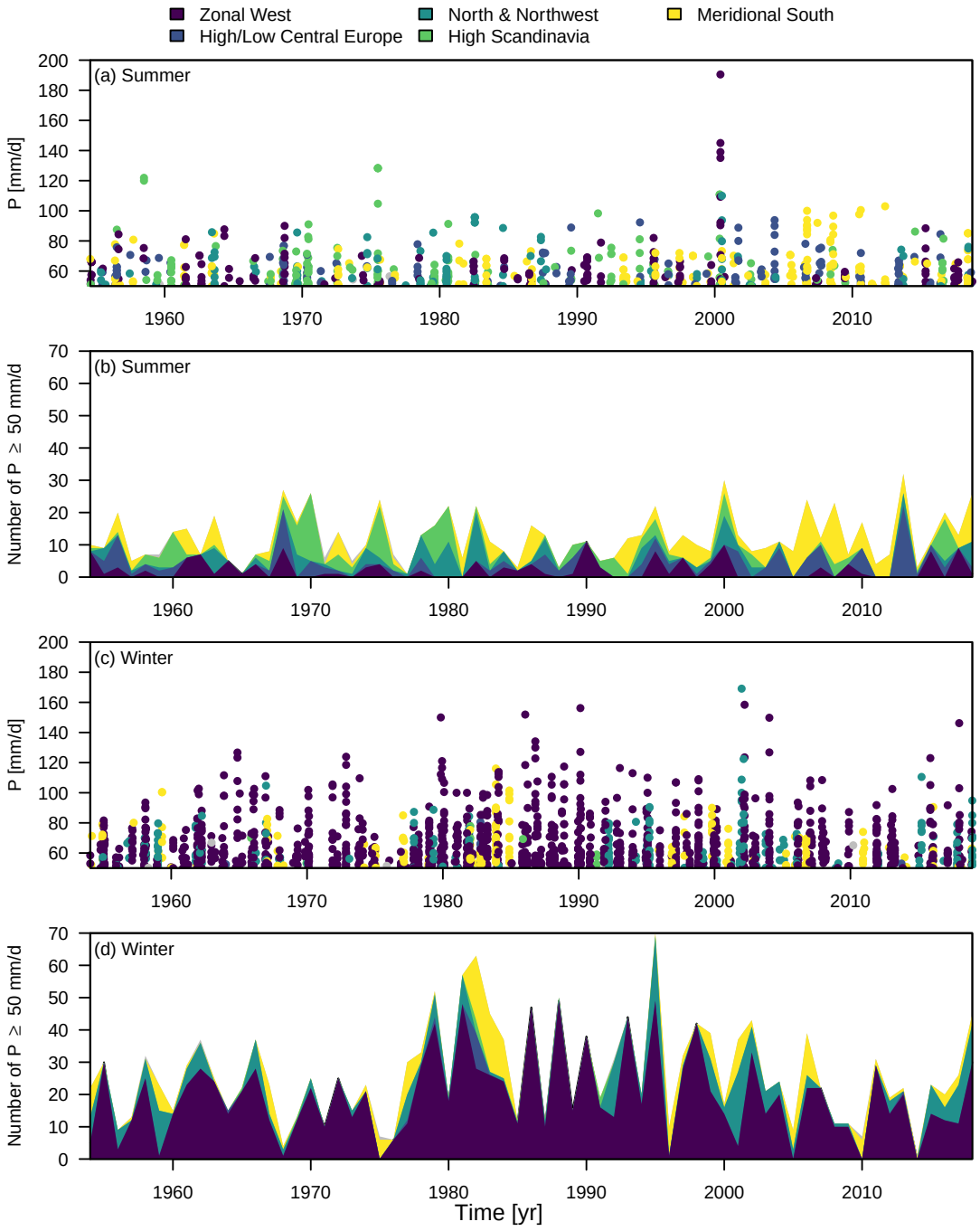

Figure 3.4.4: Distribution of the precipitation events and the underlying circulation types over time (1954-2018) during the summers (a-b) and winters (c-d).

3.4.4 Correlation of streamflow and atmospheric circulation patterns

Our analysis shows that winter maximum daily discharge levels remain strongly linked to westerly atmospheric circulation types (including WZ (Cyclonic Westerly), WS (South-Shifted Westerly), SWZ (Cyclonic South-Westerly), TRM (Trough over Central Europe), and TRW (Trough over Western Europe)), with correlation coefficients (R^2) comprised between 0.45 and 0.51 for the Wiltz, Alzette, and Our rivers (Fig. 3.4.5, Fig. 3.4.6, Fig. 3.4.7). These correlation coefficients are much higher than those found between winter maximum daily discharge and annual precipitation (R^2 between 0.13 and 0.31).

The circulation patterns during flash floods vary widely across all circulation forms (Table 3.4.3). The most important flash flood series in 2016 and 2018 occurred under SEZ (Cyclonic South-Easterly) and HFZ (Scandinavian High, Trough C. Europe), as well as HNFZ (High Scandinavia-Icelandic, Trough C. Europe). While for HNZ and HNFZ precipitation amounts are higher than average during summer, SEZ has unstructured precipitation patterns (Gerstengarbe et al., 1999). What the diverse selection of patterns have in common are meridional flow components from the Mediterranean or North-South ridges along which the events form. A few of the flash flood events can also be allocated to zonal circulation patterns as during the winters. Noteworthy is the atmospheric river, that caused the flash flood in the Hupselse beek, just north of out study area (Brauer et al., 2011).

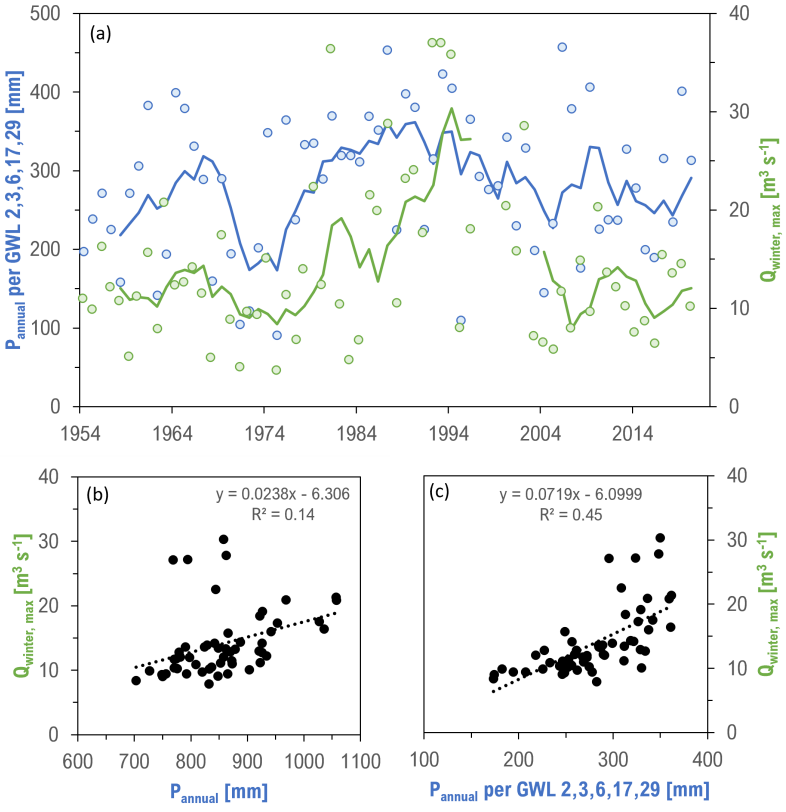

Figure 3.4.5: Correlation between maximum discharge during winters (Wiltz River near Winseler) and annual precipitation related to zonal atmospheric circulation patterns 2 (WZ), 3 (WS), 6 (SWZ), 17 (TRM), and 29 (TRW). The blue and green lines represent the 5-year moving averages.

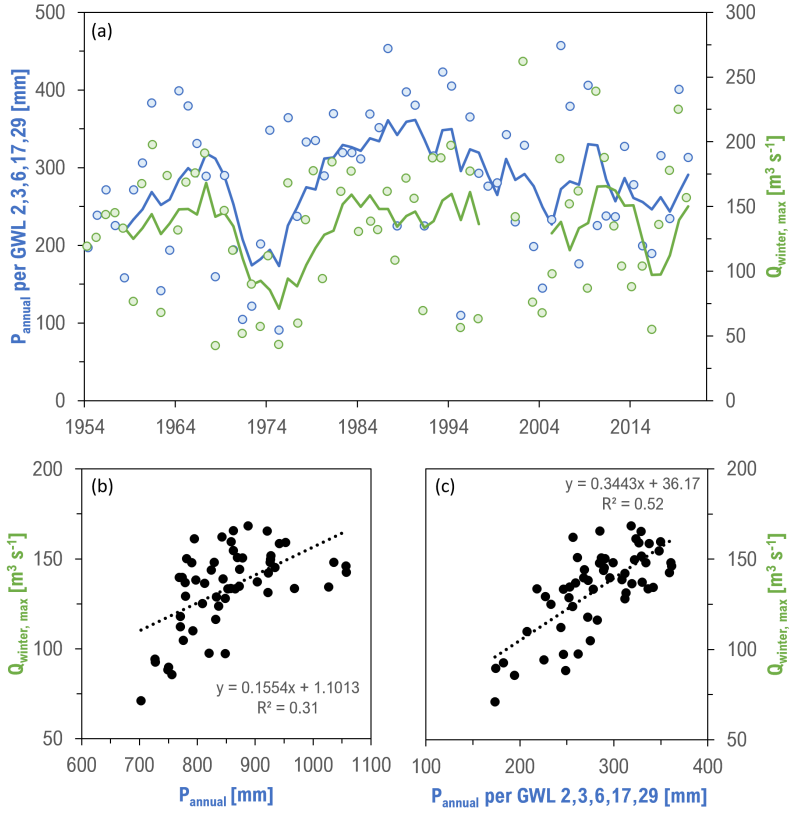

Figure 3.4.6: Correlation between maximum discharge during winter (Alzette River near Ettelbruck) and precipitation related to zonal atmospheric circulation patterns 2 (WZ), 3 (WS), 6 (SWZ), 17 (TRM), and 29 (TRW). The blue and green lines represent the 5-year moving averages.

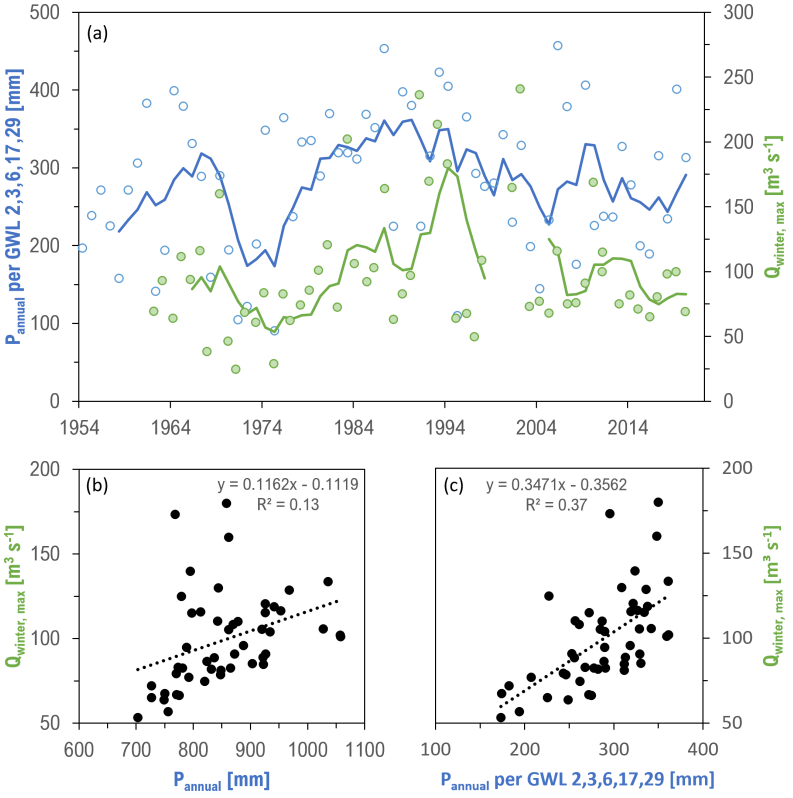

Figure 3.4.7: Correlation between maximum discharge during winter (Our River near Gemünd) and precipitation related to zonal atmospheric circulation patterns 2 (WZ), 3 (WS), 6 (SWZ), 17 (TRM), and 29 (TRW). The blue and green lines represent the 5-year moving averages.

Table 3.4.3: Circulation patterns during central European flash flood events (Flash floods listed in Table S3.1).

GWL		Circulation pattern	Occ.	Days	Events
25	SEZ	Cyclonic South-Easterly	9	2	2018 (8), 2008 (1)
21	HFZ	Scandinavian High, Ridge C. Europe	7	2	2019 (1), 2016 (6)
23	HNFZ	High Scandinavia-Iceland, Trough C. Europe	5	3	2018 (3), 2016 (1), 2008 (1 - Starzel, Ruiz-Villanueva et al., 2012)
29	TRW	Trough over W. Europe	3	3	2015 (1), 2014 (1), 2010 (1)
6	SWA	Anticyclonic South-Westerly	2	2	2019 (1), 2015 (1)
10	BM	Zonal Ridge across C. Europe	2	2	2008 (1), 2006 (1)
14	HFA	Scandinavian High, Ridge C. Europe	2	1	2019 (2)
11	TM	Low (Cut-Off) over C. Europe	2	1	2016 (2 - Braunsbach, Bronstert et al., 2018)
1	WA	Anticyclonic Westerly	2	2	2016 (2)
2	WZ	Cyclonic Westerly	2	2	2015 (1); 2010 (1 - Hupselse beek, Brauer et al., 2011)
15	HNZ	Icelandic High, Trough C. Europe	1	1	2009 (1)
6	SWZ	Cyclonic South-Westerly	1	1	2010 (1)
17	TRM	Trough over C. Europe	1	1	2013 (1 - Weißeritz, Tarolli et al., 2013)

3.4.5 Fluctuation of circulation patterns

We have analysed the annual fraction of circulation patterns with an 11-year moving average and identified a few variations over the study period (Fig. 3.4.8). Throughout the year, the Zonal West circulation types are present around 20% of the time. Yet, in the 1980s and 1990s, winter Zonal West circulation types cover a fraction of 30%. Other circulation patterns that have had a significant variability throughout the time period from 1954 to 2018 are: (1) BM "Zonal Ridge across Central Europe", where high pressure zones South-West and East of central Europe grow together to form a band of high pressure across central Europe, that is generally not associated with large precipitation amounts, yet with hail; (2) SWZ "Cyclonic South-Westerly", where a South-West frontal zone lies over Central Europe that tends to bring especially high precipitation amounts and hail; (3) TRM "Trough over Central Europe" and (4) TRW "Trough over Western Europe", are both slightly differently

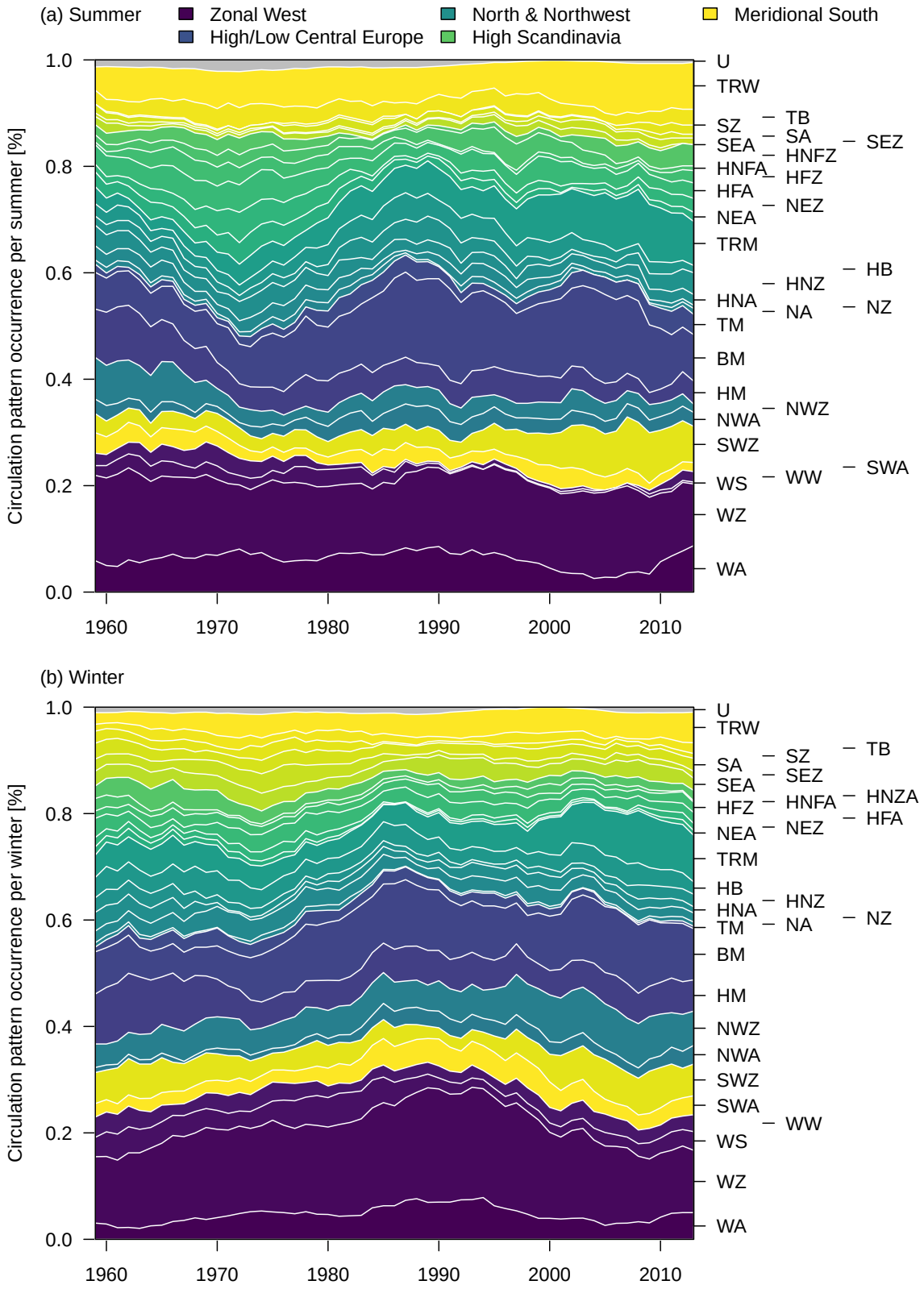

Figure 3.4.8: 11-year moving average of the percentage of weather pattern occurrences during the summer (a) and the winter (b).

located trough weather patterns, that are both associated with high rainfall amounts (Gerstengarbe et al., 1999; Kunz et al., 2009).

3.5 Discussion

To test the first part of our hypothesis, stating that there is a recent accumulation of extreme precipitation events, we analysed daily precipitation station data above 50 mm/d from 1954 to 2018. However, it is difficult to isolate fluctuations and trends regarding both, the events' precipitation amounts and their occurrence frequency. Apart from the higher frequency of precipitation events during the winters in the 1990s, we were not able to identify trends. While Koutsoyiannis (2020) confirmed the absence of trends in precipitation station data across Europe, other studies were able to extract trends from measured data. Rauthe et al. (2020) analysed precipitation events above 20 mm/d in Germany during the last 70 years and found a slight increase in the intensity and frequency of precipitation. However, these findings only apply to winter months, while there are no clear signals in summer months. The authors suggest that this might be due to counteractive effects of a decreasing number of days with precipitation and an increasing intensity of the fewer events. An explanation for the lack of trends in our study could be the coarse station network that misses potentially increasing local thunderstorm events in summer. To improve this shortcoming, we have analysed highly resolved radar precipitation data in Chapter 4.

To root for the cause of extreme precipitation, we have identified and analysed the atmospheric circulation patterns present during the events. During the winters, the main precipitation causing circulation types are zonal circulation types, arriving from the West or North-West/South-West variations. This precipitation distribution is well known and recognized in Gerstengarbe et al. (1999). The situation during the summers is more complex. While the same patterns can be observed as in the winters, localised thunderstorm events add to the precipitation. Thunderstorm events do not only have a different precipitation characteristic, but also differing underlying circulation patterns. Generally, meridional south circulation patterns, that bring warm and moist air from the Mediterranean, are associated with intense summer precipitation events (Van Delden, 2001). Yet, for extreme precipitation events we were not able to identify specific underlying circulation patterns as the variety is high. Kunz et al. (2009) isolated three hail relevant circulation patterns: SWA, SWZ and BM. While hail is connected to thunderstorms, these circulation patterns only partly overlap with the circulation patterns during extreme precipitation. A very general explanation for the wide variation of weather patterns that sustain precipitation events during the summers could be that warmer air masses can hold more absolute moisture, following the Clausius-Clapeyron relationship, potentially leading to higher rainfall totals.

The correlation of high streamflow and atmospheric circulation patterns is closely related to the circulation patterns related to extreme precipitation events. Winter floods were and are highly correlated with the occurrence of zonal circulation patterns (Pfister et al., 2000, 2004). The large winter floods in the region affecting Moselle

and Rhine in the 1990s were all associated with large-scale, long-lasting precipitation, saturated soils and eventually flooding in receiving rivers that was triggered by zonal circulation (Pfister et al., 2000, 2004; Mansell, 1997). The following decline in the zonal circulation type's occurrence implied a reduction of flood events in the following years.

The observation of accretive flood events during the summer, is less easily attributed to specific atmospheric circulation types. The synoptic constellations duing the flash flood event series in 2016 and 2018 are described in detail in Mathias (2019, 2021); Piper et al. (2016); Mohr et al. (2020). According to Hess and Brezowsky (1977) HFZ and SEZ were the underlying circulation patterns during the relevant days and they have remained stable over time. While the flash flood events of our database occur widespread through differing circulation patterns, it can also be observed that the events occur in consecutive days during differing circulation patterns. This hints towards the importance of the composition of the air masses rather than the circulation pattern. Following this path, we have analysed the atmospheric conditions during extreme events in Chapter 4. We further conjecture that an increase in generally precipitation bringing circulation patterns might increase soil moisture conditions, that set the scene for a quick soil saturation favouring fast runoff processes following precipitation events, that are in themselves not more extreme than others. Also a different sequence of weather patterns or blocking situations, that might elevate pre-event soil moisture conditions could be a cause for the recent flash flood event series.

Regarding the overall fluctuation of atmospheric mesoscale circulation patterns, the phase with increased zonal circulation during the decade spanning from the late 1980s and early 1990s has already been evaluated to a large extent (e.g. Pfister et al., 2000, 2004; Mansell, 1997). The circulation patterns that occurred more frequently in the following decade are the two trough constellations TRM and TRW. The frontal zone, a U-shape over Europe, guides air masses to the South, where they are warmed and enriched with moisture over the Mediterranean before being transported northward. Both bring more than average precipitation on the Eastern flank of the trough. Especially the Vb-situation, that occurs during TRM, is known for abundant rainfall and summer floods, such as the Elbe-Flood in August 2002 (Fritzschner and Lux, 2002), the July 2021 flood in Western Europe (Mohr et al., 2023) or the flood in the beginning of June 2024 in Southern Germany and Austria (Bauer, 2024).

3.6 Conclusions

In this chapter we have related strong precipitation and flood events to atmospheric circulation patterns as per the Hess and Brezowsky (1977) classification. Our first hypothesis is based on findings by Pfister et al. (2000, 2004) and states that the strong correlation between atmospheric circulation types and winter discharge observed in the second half of the 20^{th} century for central Western Europe still prevails today. After having leveraged 25 years of additional data (1996-2021), we can clearly confirm this hypothesis. The winter flood series that had affected the Rhine and Moselle

valley in the 1990s was linked to an increased occurrence of zonal weather patterns.

In addition to winter events, we were also interested in the relation between atmospheric circulation patterns in summer related to extreme precipitation and flood events. Here, we hypothesized that the recent accumulation of extreme precipitation and flash flood events in central Western Europe was also triggered by a change in atmospheric circulation patterns.

Our analysis of daily precipitation data covering 64 years (1954-2018), did not confirm the conjectured accumulation of (recent) summer precipitation occurrences towards the end of this time period. The interannual variation is high, both for the annual number of precipitation events and the maximum daily precipitation levels. However, due to the often local nature of thunderstorm cells, event peaks may not be well accounted for in the coarse station network. Note, that an accumulation of winter precipitation events was however confirmed for the late 1980s and early 1990s. The conjectured accumulation of flash flood events is developed further in Chapter 4.

While the correlation of winter precipitation and zonal circulation patterns is predominant, the origin of summer extreme precipitation events or flash flood events is very diverse. A few summer events can be attributed to zonal circulation like most winter events. Meteorological conditions favouring thunderstorms are in many cases related to air masses originating in the Mediterranean area. However, they do not systematically relate to meridional circulation patterns on the event day itself.

Through the analysis of fluctuations in circulation patterns, we found a few categories with substantial increases in occurrences in recent years: BM (Zonal Ridge across Central Europe), SWZ (Cyclonic South-Westerly), TRM (Trough over Central Europe) and TRW (Trough over Western Europe). The two trough circulations form a U-shaped pattern over the European continent. On the back side of the trough, warm and moist air from the Mediterranean is guided northward. The closely related SWZ acts comparably by channelling Mediterranean air masses northward. This constellation clearly has the potential to contribute to precipitation events in summer. Note that the flash floods observed in 2016 and 2018 were however not observed during these circulation patterns. Changes in atmospheric circulation patterns can therefore not be directly linked to changes in extreme precipitation events.

As a consequence, we conjecture that other factors also come into play, such as increased pre-event soil moisture due to altered sequences in circulation patterns, or longer-lasting, e.g. blocked atmospheric situations. In order to test this conjecture, we have worked with highly resolved precipitation data and parameters representing atmospheric conditions in Chapter 4.

4

Atmospheric Conditions Favouring Extreme Precipitation and Flash Floods in Temperate Regions of Europe

To get a better grasp of the common atmospheric conditions present during extreme precipitation and flash flood events, we moved from the circulation patterns analysed in Chapter 3 to a more detailed analysis of atmospheric parameters. We identified and analysed atmospheric proxy parameters representing high atmospheric moisture, sufficient latent instability, and weak thunderstorm cell motion. These three components are considered the main ingredients for rain-intense thunderstorms that can eventually trigger flash floods. Similar to the circulation patterns analysed in Chapter 3, the analysis of the atmospheric proxy parameters allows drawing conclusions on changing climate conditions with respect to the probability of supporting strong, rain-intense thunderstorms.

This chapter is based on:

Meyer, J., Neuper, M., Mathias, L., Zehe, E., and Pfister, L.: Atmospheric conditions favouring extreme precipitation and flash floods in temperate regions of Europe, Hydrol. Earth Syst. Sci., 26, 6163–6183, doi: 10.5194/hess-26-6163-2022, 2022.

Author contribution:

JM, MN, LP, and LM conceptualized the study. JM collected the flash flood and ERA5 data, carried out the analysis, and wrote the first draft of the paper. MN provided the processed precipitation radar data. All the co-authors (JM, MN, LP, LM, and EZ) contributed to and edited the manuscript.

4.1 Introduction

Flash floods mostly originate from deep moist convection and rank among the most destructive hazards, leading to economic losses, damage to infrastructure, and high mortality rates (Gaume et al. (2009); Hall (1981); Llasat et al. (2014), WMO, 2017). They are often accompanied by massive erosion and other geomorphologic processes, such as landslides (Bucała-Hrabia et al., 2020; Vogel et al., 2017). While flash floods remain rather exceptional, their occurrence has more than doubled in Europe since the beginning of the 21^{st} century in comparison to the late 1980s (Marchi et al., 2010; Owen et al., 2018). Flash floods in central western Europe typically affect relatively small areas (a few kilometres to 100 km^2) and generally last less than 7 h (Marchi et al., 2010). Caused by conditionally unstable atmospheric conditions, mainly between May and July, they do not substantially affect the annual water balance. High pre-event soil moisture – caused by rainy weather in the preceding days – may lead to the rapid saturation of soils and the swift onset of an extreme runoff response (Marchi et al., 2010). Examples of flash floods in recent years occurred in Luxembourg in June 2018 (Pfister et al., 2020) and July 2016 (Pfister et al., 2018), in Braunsbach (Germany) in May 2016 (Bronstert et al., 2017, 2018), and in the Starzel River, which flooded in June 2008 (Ruiz-Villanueva et al., 2012). While large-scale winter inundations were the most common flood type in western Europe until the 1990s (Pfister et al., 2004), flash flood events have increasingly occurred over the last 15 years (Göppert, 2018; Marchi et al., 2010). This raises questions about the origin of this change in flood type (Bertola et al., 2020, 2021). In this study, we conjecture that changes in the average atmospheric conditions may more often lead to flash-flood-prone meteorological conditions.

The definitions of flash floods are manifold and sometimes even equivocal in the literature. In this study, we focus on pluvial floods triggered by intense (convective) rainfall during summer – typically lasting for a few hours. The response times to peak discharge lie within a similar range. The flood characteristics refer to a comprehensive set of extreme and small-scale floods with rapidly rising and falling limbs of the hydrograph and a high impact in terms of damage to infrastructure and/or casualties in the worst case. The largest floods in our database involved catchments (of the White Ernz and Starzel rivers) with a size of just over 100 km^2, and the smallest events had affected hillslopes of a few hundred metres, where major surface runoff had been reported. We prefer to keep the definition simple and not precisely quantify or limit it to specific processes, as little is understood about the underlying processes. The US National Weather Service defines a flash flood in a similarly broad fashion: "a rapid and extreme flow of high water into a normally dry area, or rapid rise in a stream or creek above a predetermined flood level, beginning within six hours of the causative event" (NWS, 2021).

Precipitation events potentially causing flash floods are characterized by high rainfall amounts over a sufficient period. This condition is met by high rainfall intensities that typically last between 30 min and a few hours (Doswell et al., 1996; Markowski and Richardson, 2010). This is mostly the case during rainfall events of convective origin. In particular, slow-moving or quasi-stationary multicellular storms can combine both high rainfall intensities and a sufficiently long duration. Combined

effects of several physical processes can cause the most severe rainfall, eventually initiating flash floods. One of these effects consists of storm training, where the storm cells move consecutively in a line-parallel direction over the same area, which may then cause high precipitation totals. Another comparable effect leading to abundant precipitation or a prolonged event duration is the so-called "back-building" effect, where the forward movement is cancelled out by the continuous backward development of new cells, thereby leading to a slow ground-relative movement of the whole precipitation area. During the flash flood events in Luxembourg in 2016 and 2018, upscale growth also had a distinctive impact on the precipitation processes (Mathias, 2019, 2021). As a result of this merging of two or more individual convective cells to form a multicell storm, the initial raindrop sizes and dynamics of merging cells are often varied, which can, in turn, cause downdraughts, producing extremely high precipitation intensities (Doswell et al., 1996; Markowski and Richardson, 2010).

Atmospheric conditions associated with excessive convective rainfall have three major characteristics: (1) sufficient latent instability, (2) high moisture content, and (3) a slow storm motion and organization (Van Delden, 2001; Doswell et al., 1996; Markowski and Richardson, 2010; Taszarek et al., 2021a). First, for deep moist convection to occur, the tropospheric lapse rates need to be sufficiently steep, and a lifting mechanism is required (Van Delden, 2001). Second, the moisture content in the boundary layer needs to be abundant in order to supply water vapour for condensation during the lifting process. High to moderate values of relative humidity in the lower to middle troposphere can further nurture convective cells by limiting water vapour losses due to evaporation and entraining dry air around convective cell boundaries (Doswell et al., 1996; Markowski and Richardson, 2010; Púčik et al., 2015). The same effect – limiting the diminishment of specific humidity by entrainment – is realized by a wide updraught. Additionally, high freezing levels and low cloud-base heights enhance the warm-cloud depth and, thus, allow the warm-rain process of collision and coalescence to be more dominant. This leads to a higher precipitation efficiency and is associated with higher rainfall rates (Doswell et al., 1996; Markowski and Richardson, 2010; Schroeder et al., 2016). In continental Europe, high values of total column water vapour are often related to the advection of warm Mediterranean air masses (Van Delden, 2001) or air masses from the subtropical region of the northern Atlantic (Mathias, 2021; Mohr et al., 2020). Lastly, to ensure a sufficient duration of the rainfall event, a large rainfall system or slow storm motion is needed (Van Delden, 2001). This generally occurs in the case of very weak pressure or geopotential gradients when the mean wind speed and the bulk shear between the surface and the lower to middle troposphere are weak. This process is often enhanced by orography, which influences the near-surface wind field channelling convergence zones (Whiteman, 2000). Moreover, a decoupled flow (a rapid vertical shift in the prevailing wind directions by at least 90°) between the lower and middle troposphere can significantly reduce storm motion in some cases, as analysed by Mathias (2019).

Proxy parameters from climate reanalysis data are regularly used to identify the atmospheric conditions described above during convective events (Brooks, 2009; Groenemeijer and van Delden, 2007; Púčik et al., 2015; Taszarek et al., 2017; Westermayer et al., 2017). The main parameters used in these studies are the bulk wind shear, to estimate the thunderstorm cell organization and precipitation efficiency,

and convective available potential energy (CAPE), to identify atmospheric instability. Púčik et al. (2015) and Westermayer et al. (2017) found that heavy precipitation occurred across a wide range of deep-layer wind shear (DLS; bulk shear between the surface and 6 km height). CAPE, as a proxy for latent instability, needs to be reasonably high for thunderstorms to develop (Púčik et al., 2015; Westermayer et al., 2017). When focussing on heavy-precipitation events within the range of thunderstorms, high specific or relative humidity are parameters to identify moisture content at different atmospheric levels (Púčik et al., 2015; Westermayer et al., 2017). To date, studies have only included the wind speed in the form of wind shear as a proxy parameter for the potential organization of convective systems, which is important for hail, severe gusts, and tornadoes. However, the development of flash floods relies on longer-lasting, extreme precipitation. Therefore, the storm motion must be slow, which is dependent on a weak flow in the lower to middle troposphere. Hence, we consider the wind speed as a relevant parameter when assessing the flash flood hazard via a slow storm motion.

The identified atmospheric parameters can be analysed over a longer period for trends or oscillations. Therein, especially trends in atmospheric instability are debated. While several studies have found increasing CAPE in reanalysis data, recent studies by Rasmussen et al. (2017), Chen et al. (2020), and Taszarek et al. (2021a) have pointed out that CAPE is opposed by increasing convective inhibition (CIN). However, higher CIN levels may lead to higher CAPE values because CIN prevents the premature initiation of convection potentially inhibiting the development of stronger CAPE and, thus, possibly increasing the potential of more intense storms. In contrast, decreasing relative humidity levels at low levels of the atmosphere, connected to rising temperatures, could potentially reduce the number of thunderstorms (Taszarek et al., 2021a). Absolute humidity is, however, expected to increase under warmer conditions and can potentially release higher precipitation totals (Lenderink and Van Meijgaard, 2008; Martinkova and Kysely, 2020; Mishra et al., 2012). Changes in wind shear were found to be minor (Rädler et al., 2018). Rädler et al. (2018) concluded, that the frequency of thunderstorms had not increased significantly over the past 40 years in central western Europe but that they are more likely to produce severe weather.

To date, most studies have focussed on thunderstorm conditions in general or on convective hazards related to lightning, hail, tornadoes, or wind gusts. Here, we focus on thunderstorm events that cause extreme precipitation and, especially, flash flood events. Forecasting potential heavy precipitation based on atmospheric conditions remains a major challenge, as different atmospheric constellations (e.g. back-building multicells, chaotic cell clustering, and atmospheric rivers) can cause heavy-precipitation events, while large hail, for example, is mostly associated with supercells and is, therefore, less challenging to identify (Púčik et al., 2015).

In view of these recent findings, we hypothesize that a change in atmospheric conditions has led to more frequent extreme precipitation events that have subsequently triggered flash flood events in central western Europe. Prior to hypothesis testing, we first compiled a comprehensive set of 20 to 40 years worth of hydro-climatological observation series – including extreme precipitation events, related atmospheric conditions, and documented flash flood occurrences. We then leveraged this data set

to investigate a potential increase in extreme precipitation events in central western Europe. Second, we relied on proxy parameters, such as CAPE, specific humidity, and wind speed, to identify the atmospheric conditions that had prevailed during extreme precipitation and related flash flood events. Third, we applied a trend analysis to the identified set of atmospheric parameters using the ERA5 reanalysis data (Hersbach et al., 2020) for the past (1981–2020). The overarching goal of our study is to contribute to a better understanding of climate change effects, as expressed through modifications in the frequency and severity of extreme precipitation events in a temperate climate – more specifically in an area where flash floods used to be an extremely rare phenomenon until recently.

4.2 Data and methods

4.2.1 Study area and period

Our study area comprises central western Europe (50.5° N–47.5° S and 10° E–5° W) including Luxembourg, south-western Germany, and north-eastern France (Fig. 4.2.1 a, b, c, d). The study period spans the summer months from May to August, which exhibit the most favourable conditions for thunderstorms and the onset of flash floods (Van Delden, 2001; Rauber et al., 2008), between 1981 and 2020.

4.2.2 Database

We downloaded the ERA5 atmospheric reanalysis data from the Copernicus Climate Data Store (CDS) at single levels (Hersbach et al., 2018a) and at different pressure levels (Hersbach et al., 2018b). In addition, we downloaded land data from ERA5 (Muñoz Sabater, 2019) to analyse the pre-event wetness state of soils in catchments. Within the summer months from May to August for the period from 1981 to 2020, selected parameters (see Sect. 4.2.3) were retrieved at a 1 h time step. The horizontal grid spacing of the atmospheric data is 0.25×0.25, whereas the horizontal grid spacing of the land data is 0.1×0.1.

The extreme precipitation event database was created based on the "Radar-based Precipitation Climatology" (RADKLIM) data set from the German Weather Service (DWD, version 2017.002 – Winterrath et al., 2018). This is a processed version of the operational RADOLAN "Radar-Online-Adjustment" radar data set from the DWD (Weigl et al., 2004; Weigl and Winterrath, 2009; Winterrath et al., 2017). Data are available from 2001 to 2020 and were considered from May to August. The data set has a $1\,\mathrm{km} \times 1\,\mathrm{km}$ grid size and a temporal resolution of 5 min. Unfortunately, the south-western part of the study area is not covered by the RADOLAN data (Fig. 4.2.1 b). Although the original RADOLAN product has already been quality checked and corrected and is, consequently, of high quality, we applied some additional quality control and correction when needed; this included – next to a thorough visual check of the data – the detection and correction of possible anomalous propagation (anaprop) echoes, further ground clutter detection and removal, and an extended rain gauge adjustment with supplementary local rain gauges. The last

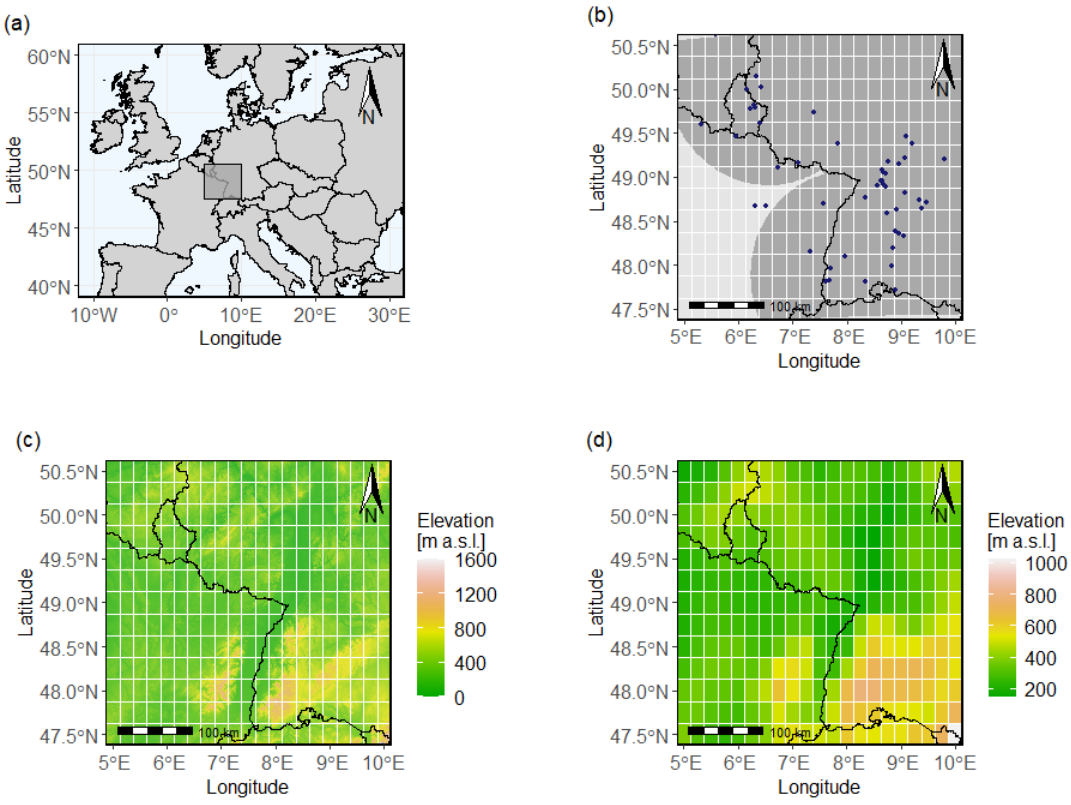

Figure 4.2.1: **(a)** Location of the study area (dark-grey square) within Europe. **(b)** Map of the study area including data points of flash floods that have occurred and the range of the German Weather Service (DWD) RADOLAN precipitation radar data in dark grey. The white grids show the grid width of the ERA5 reanalysis data set. Panel **(c)** shows a digital elevation model of the area at a $1\,\mathrm{km} \times 1\,\mathrm{km}$ resolution, and panel **(d)** presents the model topography within the study area based on the ERA5 surface geopotential.

operation was done to achieve a further densification of the measuring network (in comparison to the original product), which is especially important when dealing with flash floods that often exhibit large spatial precipitation sum gradients. To ensure a comparable standard, we used the same methodology for the rain gauge adjustment as used for the generation of the original RADOLAN/RADKLIM data set: the best combination of the multiplicative and the additive adjustments (Weigl et al., 2004; Wilson and Brandes, 1979; Wood et al., 2000). The adjustment interval was 1 h. In Luxembourg, the extra stations used were mainly the stations of the ASTA (Administration des Services Techniques de l'Agriculture) network (ranging from 7 to 40 extra stations); in Germany, the stations of the agricultural–meteorological network of the state of Rhineland-Palatinate (ranging from 10 to 50 extra stations) were used. The additional rain gauge data were quality controlled based on Sevruk (1986) and Michaelides (2008). We extracted the precipitation events (P events) for the database from the radar database by identifying $1\,\mathrm{km} \times 1\,\mathrm{km}$ grid cells with precipitation amounts $\geq 40\,\mathrm{mm\,h^{-1}}$. Connected grid cells with a maximum of one

cell (1 km distance) in between two or more cells exceeding the threshold and a maximum of a 30 min time gap were clustered to account for one P event (Fig. 4.2.2). The threshold of 40 mm h^{-1} was used according to the definition of extreme precipitation events by the DWD, 2021. This approach led to a total of 3835 P events between 2001 and 2020 (Table 4.2.1). For every P event, we extracted the maximum hourly precipitation intensity as well as the maximum 5 min precipitation intensity at one location within the P event. Moreover, the temporal (time of the first threshold exceedance in one of the grid cells of the P event to the time of the last exceedance) and spatial (area of the number of grid cells that are part of a P event) distribution of the events were identified. Atmospheric conditions during P events were identified at the beginning of an event, as atmospheric conditions should be the most characteristic at the onset the event. To receive a spatially representative value, the mean of each atmospheric ERA5 grid cell of the P event itself was calculated as well as a buffer zone around the event, according to the schematic representation in Fig. 4.2.2. For a small standard P event that lies within one ERA5 grid cell, atmospheric data were averaged over that particular ERA5 grid cell and the eight surrounding cells. Precipitation events at the boundary of the study area do not include the full buffer zone, and larger P events covering multiple grid cells include a buffer zone around the ERA5 grid cells of the actual P event. A more detailed description of this procedure and its special cases are documented in the Supplement S5.

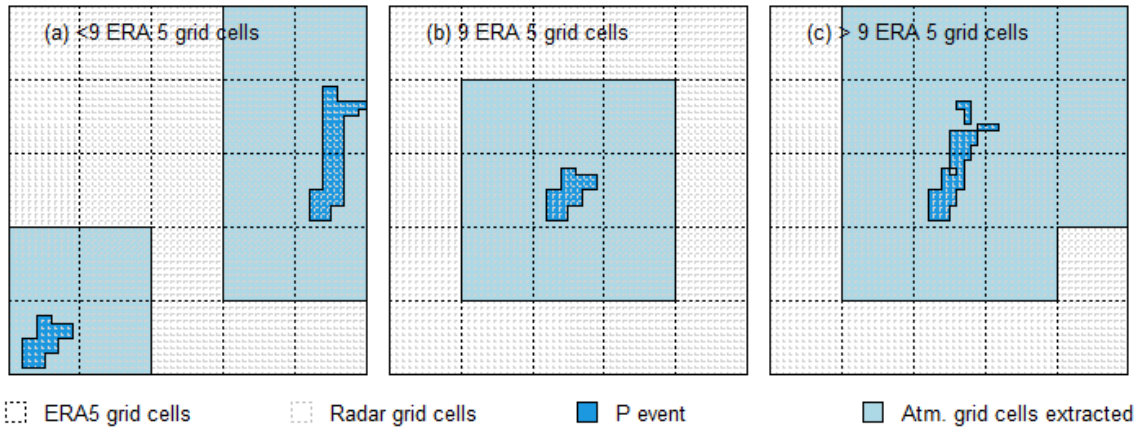

Figure 4.2.2: Schematic representation of the ERA5 grid cells (0.25 × 0.25, ∼ 25 km × 25 km) that were averaged to calculate representative atmospheric conditions during P events (grid width 1 km × 1 km). The grid of the ERA5 cells (black) and the radar cells (grey) is marked with dashed lines. The radar grid cells marked in blue are those exceeding the precipitation threshold during a P event. The surrounding ERA5 grid cells marked in light blue are those that were used to average the atmospheric conditions. Panel **(b)** shows the standard case of a buffer zone of a one-ERA5-grid-cell P event, panel **(a)** shows some possible exceptions at the boundary of the study area, and panel **(c)** shows the procedure for larger P events covering multiple ERA5 grid cells.

The flash flood database was compiled via a search through case studies in the

scientific literature (Brauer et al., 2011; Bronstert et al., 2018; Van Campenhout et al., 2015; Eden et al., 2018; Göppert, 2018; Ruiz-Villanueva et al., 2012), water agency reports (Johst et al., 2018; Pfister et al., 2018, 2020), reinsurance data (CCR - Caisse Centrale de Réassurance, 2021), personal communication (engineering consultants WALD + CORBE – Catharin Schäfer and Hans Göppert), and news archives (Franceinfo, 2021; Luxemburger Wort, 2021). We included floods in streams, fields, or on streets that are spatially (maximum of 30 km) and temporally (same day) linked to an extreme P event exceeding the threshold of 40 mm h^{-1}. If a flood was triggered by a rainfall event not identified as extreme in the radar data, the flood was not considered. Despite a careful and comprehensive query, the database is likely non-exhaustive. Nevertheless, we think that this approach of site inspections is the most inclusive. Sufficient discharge time series are mainly available for larger rivers and bigger stream gauges than those in which flash floods occur. Moreover, data availability in the past has often been limited to a daily resolution, which can easily miss capturing peak flows during flash floods. Relying on high-flow water levels in the past also makes it difficult to distinguish flash floods from slowly developing floods, which have occurred regularly in the past, especially in the mountainous parts of the study area. A particular example of the limits of a discharge time-series-based approach are the flash floods in Luxembourg (Pfister et al., 2018, 2020), which were detected by stream gauges only to a limited extent within an overall time series that is too short for any long-term analyses. A list of the 40 events that were eventually included in this study spanning the period from 2002 to 2020 can be found in the Supplement S3. To extract atmospheric parameters during flash flood events, we identified the triggering P event within a 30 km range and proceeded according to the approach for P events (as shown in Fig. 4.2.2). By using this approach, we found 37 of the total of 3835 P events to be associated with flash floods (Table 4.2.1). This is less than the number of flash floods themselves, as two flash floods were triggered by the same P event in 2008 (Rangendingen and Jungingen, Ruiz-Villanueva et al., 2012), and three floods were triggered by the same P event in 2018 (Rhineland-Palatine, Johst et al., 2018).

Table 4.2.1: The total number of P events and the number of P events that were associated with flash floods (FFs).

	P events	P events associated with FF	FF events
No. of events	3835	37	40

4.2.3 Identification of atmospheric parameters favouring extreme precipitation and flash floods

Referring to work done by Van Delden (2001), Westermayer et al. (2017), Taszarek et al. (2017), and Púčik et al. (2015), we selected relevant atmospheric parameters to represent (1) instability, (2) the moisture content, and (3) storm motion and

organization; additionally, we extracted (4) soil moisture content from the ERA5 data set to get an indication of the wetness state of the catchment before the onset of an extreme precipitation event (Table 2.2.1).

As proxy parameters for atmospheric instability, we used the convective available potential energy (CAPE, in $\mathrm{J\,kg^{-1}}$), which is provided within the ERA5 single-level data sets. In addition, we also considered convective inhibition (CIN, in $\mathrm{J\,kg^{-1}}$). Given its recognized potential as a flash flood proxy, we used the K index (in °C) that is provided within the ERA5 data set. The K index (George, 1960) is defined as follows:

$$\begin{aligned}\text{K index} = (T_{850\,\mathrm{hPa}} - T_{500\,\mathrm{hPa}}) + T_{\mathrm{d}\,850\,\mathrm{hPa}} - (T_{700\,\mathrm{hPa}} \\ - T_{\mathrm{d}\,700\,\mathrm{hPa}}),\end{aligned} \tag{4.1}$$

where T is the air temperature at differing pressure levels, and T_d the dew point temperature (in °C).

The K index is a stability index that is based on the vertical extent of low-level moisture and the vertical temperature lapse rate of the lower and middle troposphere. While the operational use of stability indices alone is limited (Doswell and Schultz, 2006), indices can provide additional value when assessing severe-weather potential. The K index was originally developed to assess potential air mass thunderstorms, or thunderstorms without a dynamic triggering mechanism (George, 1960). Most importantly, it shows some special skill in forecasting the potential of thunderstorms related to heavy precipitation (Funk, 1991; Junker et al., 1999). Regarding the potential for heavy precipitation, it can be generally stated that the higher the K-index value, the greater the potential for heavy rain. Generally, K-index values above 20 °C indicate thunderstorms, while there is no thunderstorm potential for values below 20 °C. K-index values are further subcategorized into isolated thunderstorms (20–25 °C), widely scattered thunderstorms (25–30 °C), scattered thunderstorms (31–35 °C), and numerous thunderstorms (> 35 °C). Note that the highest category with K-index values above 35 °C is, however, extremely rare in central western Europe (< 0.5 % within the study area and period, as calculated based on the ERA5 data used).

To reach a sufficiently high rainfall rate causing heavy precipitation and consequent flash floods, the atmosphere's moisture content is pivotal. We opted for the total column water vapour (TCWV, in $\mathrm{kg\,m^{-2}}$) as well as specific humidity (q, in $\mathrm{kg\,kg^{-1}}$) and relative humidity (RH, in %) at the pressure level of 700 hPa as atmospheric moisture content proxies. The pressure level of 700 hPa was chosen because it is approximately the middle of the lower, weather-relevant part of the atmosphere between the surface and 500 hPa.

To assess the storm motion, we computed the wind speed (WS) from the square root of the squared northward direction wind vector $\vec{u}$ (in $\mathrm{m\,s^{-1}}$) and the squared eastward direction wind vector $\vec{v}$ (in $\mathrm{m\,s^{-1}}$) at the pressure level of 700 hPa. In addition, the mean of the wind speed between 10 m a.g.l. and the pressure level of 500 hPa was calculated. Low-level wind shear (LLS, in $\mathrm{m\,s^{-1}}$) was likewise computed based on the square root of the differences in the vectors $\vec{u}$ and $\vec{v}$ near the ground and at about 1.5 km height (850 hPa). Accordingly, we calculated the deep-layer

wind shear (DLS, in $m\,s^{-1}$) as the difference in the wind vectors near the ground and at about 6 km height (500 hPa). The wind shear allows an assessment of the organizational mode of deep moist convection.

We considered soil moisture parameters for assessing the pre-event wetness state of a catchment. Therefore, we extracted soil moisture (Swvl, in $m^3\,m^{-3}$) at depths of 0–7, 7–28, and 28–100 cm from ERA5 a total of 24 h before the onset of identified P events and the onset of flash-flood-triggering P events respectively.

To identify extreme precipitation and flash-flood-relevant proxy parameters, we extracted their respective values from the ERA5 atmospheric data set at the time step and grid cell of initially identified events. Next, we created thresholds for every proxy parameter that makes the occurrence of precipitation events possible. Therefore, we chose the 75^{th} or 25^{th} percentile as the respective upper or the lower boundaries, including either the lower or the upper three quartiles of all values of extreme events respectively. These percentiles were chosen as the statistical standard, as also used in Schroeder et al. (2016). This analysis leads to the determination of the thresholds (in Table 4.3.1) used to classify atmospheric conditions as extreme precipitation and potentially "flash flood favouring". We used these thresholds as well as the three parameters identified as the most suitable from the groups of moisture, instability, and storm motion and organization to eventually conduct trend analyses.

4.2.4 Trend analyses

We carried out linear trend analyses to test the different parts of our working hypothesis – linking a potential increase in atmospheric conditions triggering extreme precipitation events to a rise in the occurrence of extreme precipitation events in central western Europe. We applied the linear models to our precipitation event database as well as to the occurrence frequency, precipitation amount, and intensity of identified extreme precipitation events. Likewise, we applied linear models to the flash-flood-relevant parameter ranges of the identified set of ERA5 atmospheric parameters as well as to the simultaneous occurrences of the three most relevant parameters.

4.3 Results

4.3.1 Flash flood occurrences

Fig. 4.3.1 shows flash flood occurrences in central western Europe. While barely any events were reported before 2006, two remarkable summers are 2016 and 2018, when flash floods occurred particularly often in the study area (8 and 11 occurrences respectively). As the temporal inconsistencies in the data set do not allow one to draw conclusions on any robust trends, this flash flood data compilation cannot support the conjectured increase in frequency of flash floods. Note that several events often occurred within a few days (Fig. 4.3.1 b) under the same mesoscale atmospheric constellation, in the same area, or even in neighbouring catchments, and are, therefore, not completely independent of one another. For example, two

flash floods in 2008 (Rangendingen and Jungingen, Ruiz-Villanueva et al., 2012) and three floods in 2018 (Rhineland-Palatine, Johst et al., 2018) occurred during the same large-scale P event.

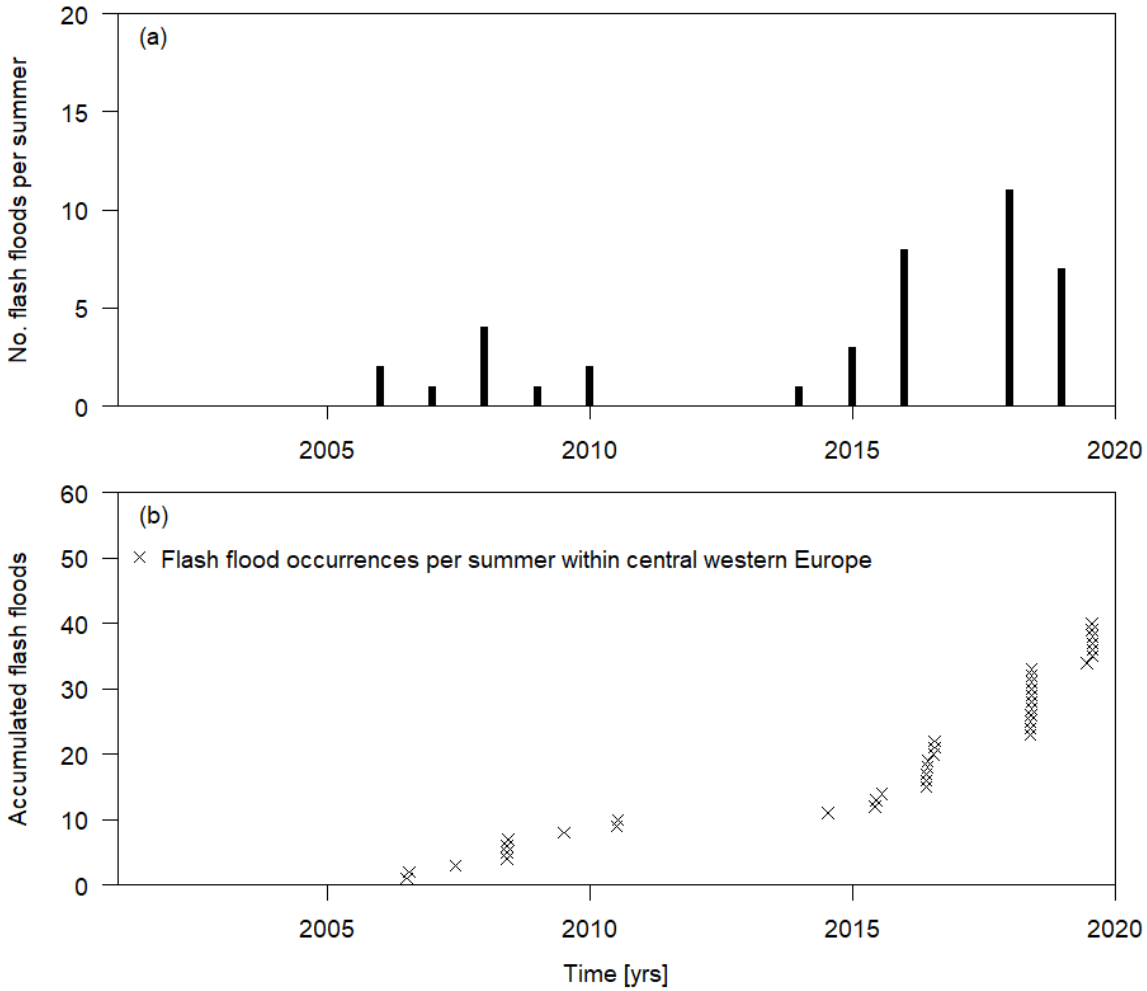

Figure 4.3.1: Occurrence of flash flood events within central western Europe between 2001 and 2020. Panel **(a)** shows the number of flash flood occurrences per summer, and panel **(b)** maintains the exact occurrence date of the flash flood event.

4.3.2 Extreme precipitation event characteristics

Within our study area, we extracted extreme P events with precipitation intensities $\geq 40\,\mathrm{mm\,h^{-1}}$ from the DWD radar data set. Between 2001 and 2020, we observed a slight but insignificant increase in the number of events per summer (Fig. 4.3.2 a). Note that the interannual variance is very high and that this increase includes two extreme years, 2006 and 2018, when precipitation events $\geq 40\,\mathrm{mm\,h^{-1}}$ occurred particularly often. Similar to the flash flood occurrences, many of the extreme precipitation events happened on the same days over a wider region. This is particularly the case for 2008 and 2018: the multiple rainfall events from 2018 overlap with a

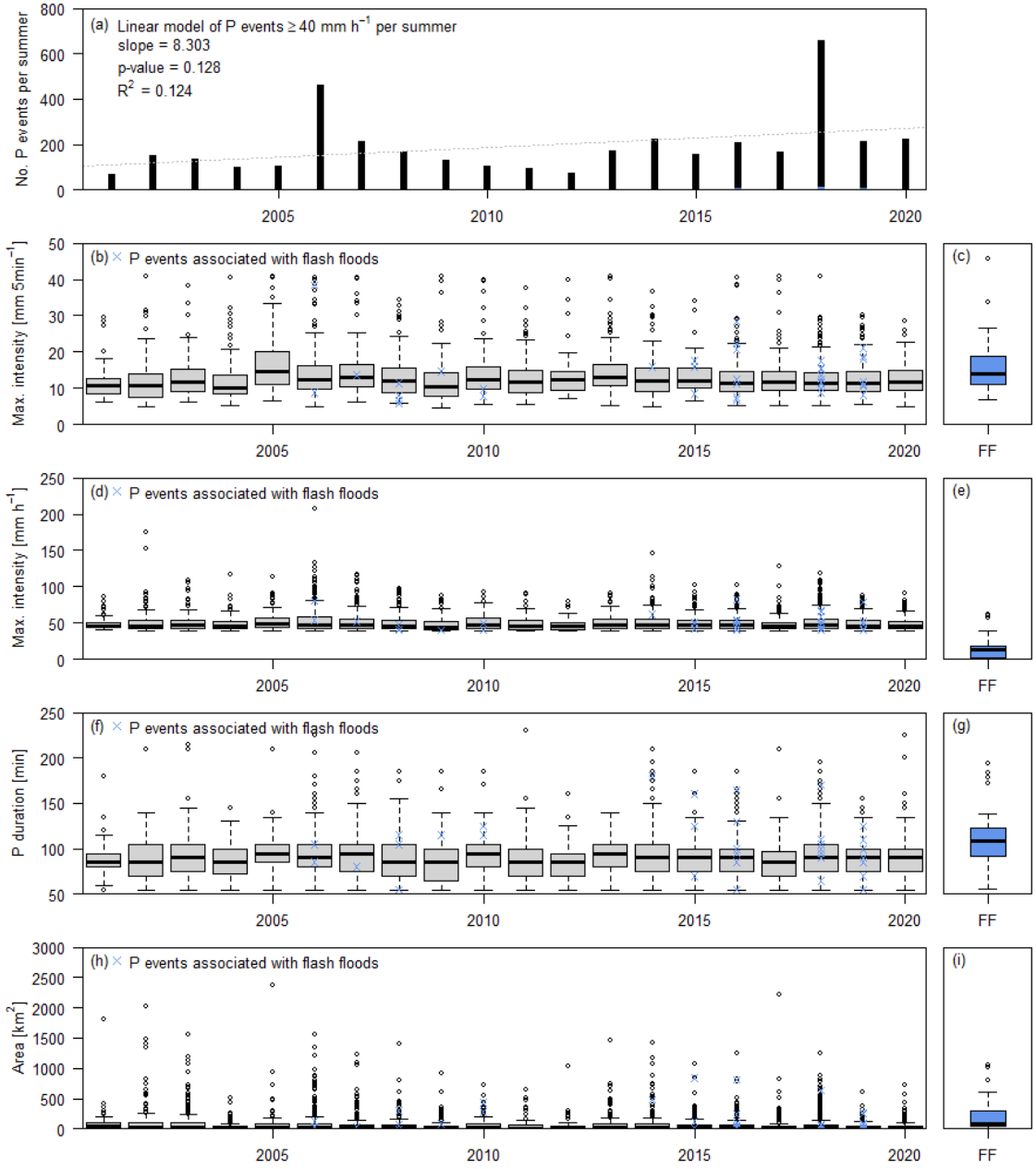

Figure 4.3.2: Occurrence of extreme precipitation events ($\geq 40\,\mathrm{mm\,h^{-1}}$) within central western Europe. The panels in the left column **(a, b, d, f, h)** show the precipitation event characteristics per summer between 2001 and 2020. The blue crosses and the right column **(c, e, g, i)** show the precipitation characteristics of the events that are associated with a flash flood. Panel **(a)** shows the number of precipitation events per summer. Panels **(b)** and **(c)** show the P events' maximum precipitation intensity per 5 min, and panels **(d)** and **(e)** show the P events' maximum precipitation intensity per hour. Panels **(f)** and **(g)** show the temporal extent of the identified events, whereas panels **(h)** and **(i)** show the spatial extent of the identified events.

high number of flash floods. For the precipitation amounts, we could not identify significant trends in the maximum 5 min precipitation intensities (Fig. 4.3.2 b) nor

in the maximum hourly intensities per event (Fig. 4.3.2 d) for the 2001–2020 period. P events that eventually led to flash floods (Fig. 4.3.2 c, e) did not differ in the range of precipitation intensities from P events that did not cause flash floods, but their median was around 3 mm h^{-1} higher. The event duration of P events that caused flash floods was, however, slightly longer compared with the other extreme P events (Fig. 4.3.2 f, g). The largest difference between P events causing flash floods and other P events was, however, the temporal and spatial extent: P events that caused flash floods were often longer-lasting and larger in comparison with extreme P events that did not lead to flooding (Fig. 4.3.2 h, i). Neither the temporal nor the spatial extent of the P events shows trends over the study period of 20 years (Fig. 4.3.2 f, h).

4.3.3 Identification of atmospheric parameters favouring extreme precipitation and flash flood events

To identify parameter ranges that favour flash floods, we considered all hourly values of the parameters between May and August irrespective of any identified events, as events could only be identified within the last 20 years of the study period. Moreover, we extracted the parameters present during the time of extreme P events and the selection of P events that led to flash flood occurrences (Fig. 4.3.3). The data emphasize the occurrence of extreme events under conditionally unstable atmospheric conditions. Most extreme precipitation and flash flood events occurred within the upper quartile of CAPE values (Fig. 4.3.3 a). Sufficient values of CAPE are often accompanied by moderate values of CIN. Both extreme precipitation and flash flood events occurred over a wide range of CIN, with a slightly higher median value at the onset of an event compared with the general values (Fig. 4.3.3 b). However, both CAPE and CIN appear to be widely scattered within the spectrum of their possible ranges. The K index, in contrast, proves to be a reliable index, and more than 80 % of all extreme precipitation and flash flood events occur within the thunderstorm-relevant categories of the index above 28 °C (Fig. 4.3.3 c). Moisture conditions during extreme precipitation and flash flood events were found to be mostly within the upper percentiles of the overall simulated values. Especially the specific humidity (q) and total column water vapour (TCWV) range clearly within the upper quartile of all values during events (Fig. 4.3.3 d, e). Relative humidity (RH) also proves to always be high during extreme events (Fig. 4.3.3 f). All moisture parameters, especially RH, tend to be even higher during flash flood events compared with general extreme precipitation events (Fig. 4.3.3 d, e, f). The wind-related parameters considered to analyse storm motion and organization are generally low during extreme precipitation and flash flood events; specifically, the $WS_{10\,m-500\,hPa}$ (Fig. 4.3.3 h) stands out, with most of the values observed during extreme events being in the lower quartile of the full range of occurrences. Tendencies regarding $WS_{700\,hPa}$, DLS, and LLS (Fig. 4.3.3 g, i, j) are less clear but show the same pattern. In addition to atmospheric parameters, soil moisture conditions were evaluated 24 h before identified events. Often, soil moisture within the upper and lower soil layer ($Swvl1_{0-7\,cm}$ and $Swvl3_{7-100\,cm}$ respectively) is higher during flash flood events compared with general extreme P events (Fig. 4.3.3 k, m). Especially the higher top-level soil moisture might hint to preceding rainfall events that could help explaining some of the quick

runoff formation present during flash floods. The mid-level soil layer ($Swvl2_{7-28\,cm}$) shows lower soil moisture before flash flood events (Fig. 4.3.3 l).

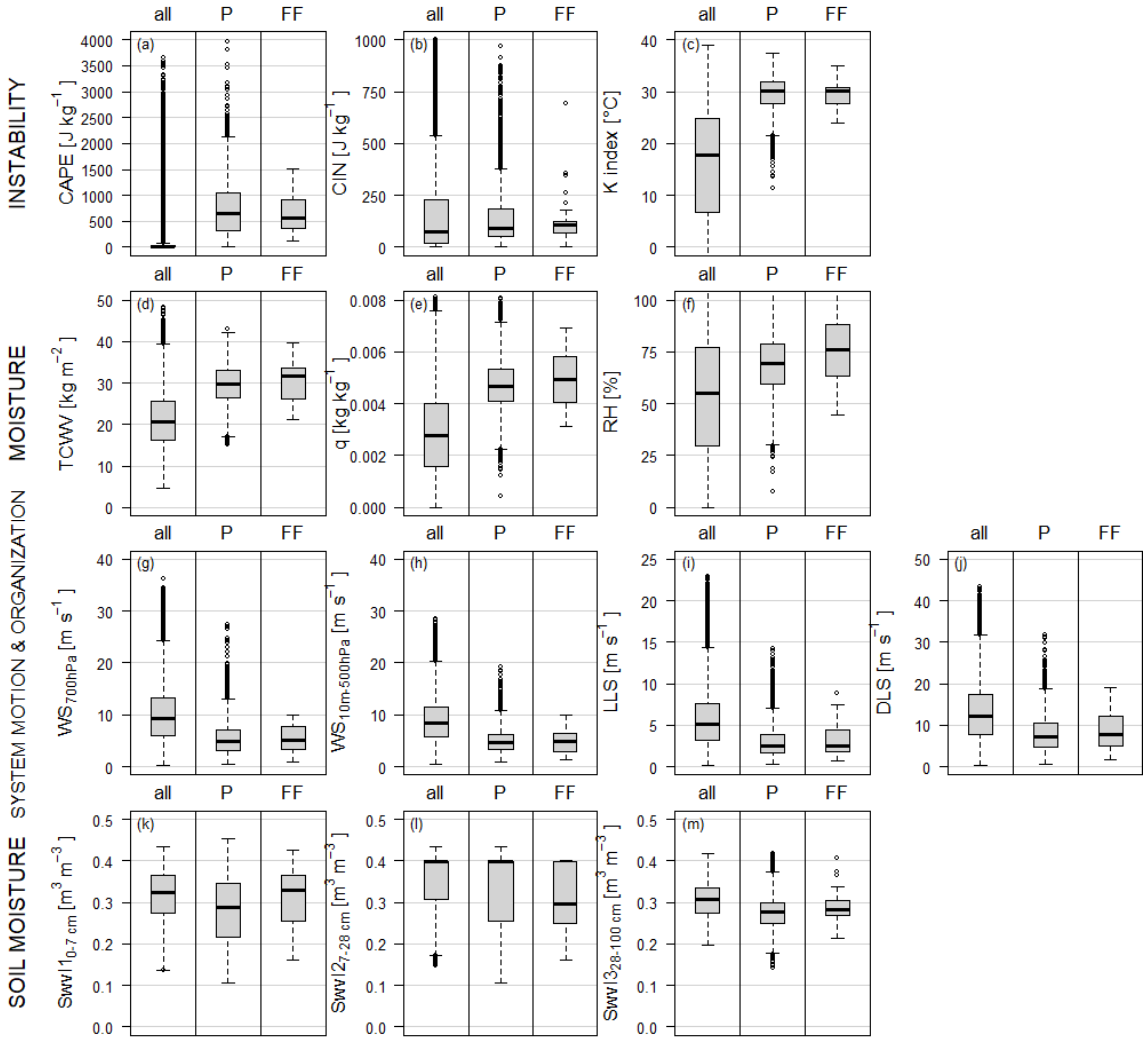

Figure 4.3.3: All hourly values of the proxy parameters **(a–j)** during the entire period (all), before extreme precipitation events (P), and before flash flood events (FF). Soil moisture **(k–m)** was extracted 24 h before the onset of identified P events or 24 h before the onset of FF-triggering P events.

This analysis leads to the determination of the thresholds in Table 4.3.1 to classify atmospheric conditions as extreme precipitation and potentially flash flood favouring. Sufficient CAPE, high q, and weak $WS_{10\,m-500\,hPa}$ were identified as the most clearly distinguishing parameters per category to characterize extreme precipitation events, including 75 % of all extreme precipitation events and excluding around 75 % of all generally occurring parameters' values.

4.3.4 Changes in atmospheric parameters between 1981 and 2020

Instability, as shown representatively by CAPE above 326.9 J kg^{-1}, has increased between 1981 and 2020. The number of hours with high enough instabilities to support the occurrence of thunderstorms increased by up to 5 h per summer (Fig. 4.3.4 a). These findings were particularly significant in the northern part of the study area (Fig. 4.3.4 b). Moreover, there are significant increasing trends regarding the actual values of CAPE above 326.9 J kg^{-1} in the north-western and mid-southern part of the study area (Fig. 4.3.4 c, d). Another measure of the atmosphere's instability and capability to produce rain-intense thunderstorms is the K index, shown in Fig. A1. The occurrence of the K-index values above 27.8 °C is strongly increasing between 1981 and 2020 throughout the study area and is significant in the northern part of the study region. Furthermore, the values of the K index above the threshold have increased, which indicates an increased intensity of rain-intense thunderstorm events. This trend is significant over the Belgian part of the study area.

The observed increase in high atmospheric moisture content, represented by q above 0.004 kg kg^{-1} (Fig. 4.3.4 e, g), is highly significant over the entire study area (Fig. 4.3.4 f, h). High-moisture-content conditions became up to 8 h per summer more frequent, especially over south-western Germany; however, the absolute increase in conditions with a very high moisture content is small (Fig. 4.3.4 g).

The storm motion potentially decreases with weak $WS_{10\,m-500\,hPa}$ that tends to occur more often in the study area (Fig. 4.3.4 i). The values below the threshold of 6.2 m s^{-1} appear to become higher in the western part of the study area and lower within the eastern part. However, these trends are insignificant over the entire study area (Fig. 4.3.4 j, l), and $WS_{10\,m-500\,hPa}$ is considered to remain largely unchanged.

Table 4.3.1: Threshold values determined as extreme precipitation and flash flood favouring based on the lower/upper quartile of their range of occurrence during extreme precipitation events, including all P events, whether they are associated with a flood or not.

Proxy for	Parameter	Threshold	Unit
Instability	CAPE	≥ 326.9	J kg^{-1}
	CIN	≤ 183.5	J kg^{-1}
	K Index	≥ 27.8	°C
Moisture	TCWV	≥ 26.5	kg m^{-2}
	q	≥ 0.004	kg kg^{-1}
	RH	≥ 59.4	%
Storm motion and organization	$WS_{700\,hPa}$	≤ 7.1	m s^{-1}
	$WS_{10\,m-500\,hPa}$	≤ 6.2	m s^{-1}
	LLS	≤ 3.8	m s^{-1}
	DLS	≤ 10.4	m s^{-1}

The complete set of analysed atmospheric parameters is shown in Appendix 4.6.1.

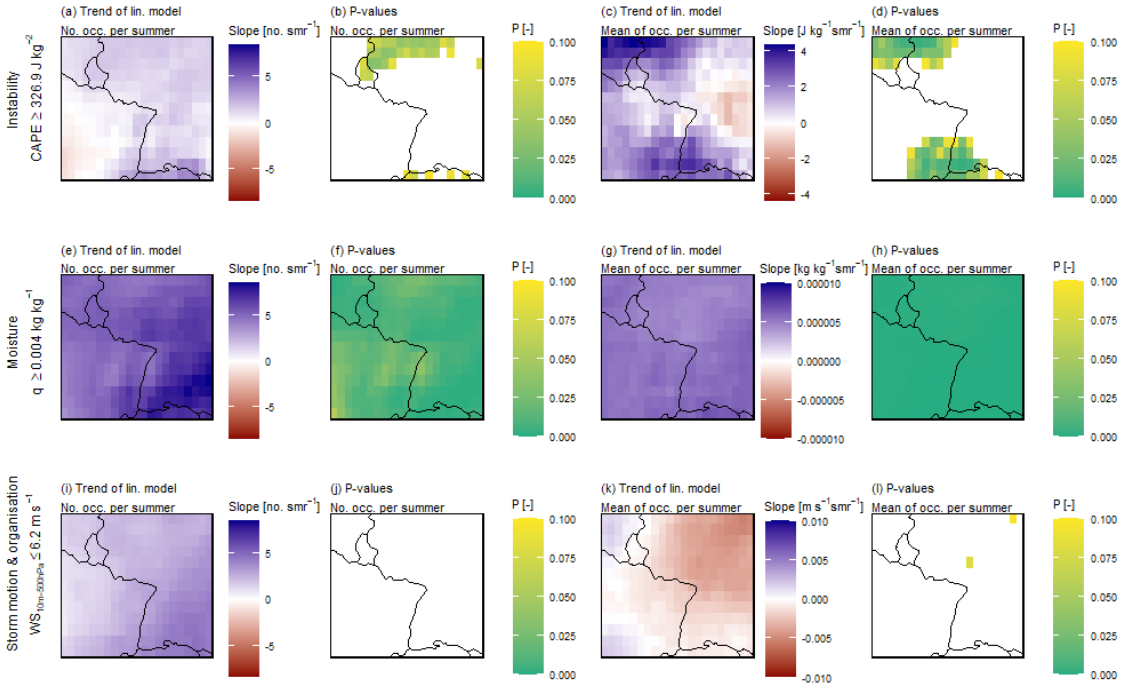

Figure 4.3.4: Trend analysis of the most suitable variables for instability (convective available potential energy, CAPE), moisture (specific humidity, q), and storm motion and organization (wind speed, $\mathrm{WS}_{10\,\mathrm{m}-500\,\mathrm{hPa}}$). The first column **(a, e, i)** shows the trends in the numbers of hourly occurrences of values above or below their respective threshold, and their significance levels are given in the second column **(b, f, j)**. The third column **(c, g, k)** shows the trends in the mean values of all hourly occurrences above or below the threshold, and the last column **(d, h, l)** displays their respective significance levels. White areas denote insignificance.

4.3.5 Spatial distribution of atmospheric conditions favouring extreme precipitation and flash flood events

The simultaneous occurrence of the three most characteristic identified atmospheric parameters from each component (CAPE, q, and $\mathrm{WS}_{10\,\mathrm{m}-500\,\mathrm{hPa}}$) within extreme-event-favouring parameter ranges is correlated with topography (Fig. 4.2.1 c). Favourable atmospheric conditions occur most frequently over the Vosges Mountains in France and in south-western Germany, compared with the rest of the study area. Over eastern Belgium, favourable atmospheric conditions have occurred less than half as often between 1981 and 2020 (Fig. 4.3.5 a). Within this period, the occurrence of favourable atmospheric conditions changed very little. Over south-western Germany, the simultaneous occurrence of these three parameters occurred only 1–2 h per summer more often, while over north-eastern France these conditions occur slightly less often (Fig. 4.3.5 b). There is, however, no significance in trends with respect to these combinations (Fig. 4.3.5 c). Splitting the 40-year period in two,

1981–2000 (Fig. 4.3.5 d, e, f) and 2001–2020 (Fig. 4.3.5 g, h, i), shows a decreasing trend within the first 20 years and a positive trend within the last 20 years. As these seem to be clear tendencies, they more or less level out over the entire time period. In line with the large variation in the number of occurrences of favourable atmospheric conditions per summer, none of the calculated trends are significant (Fig. 4.3.5 f, i).

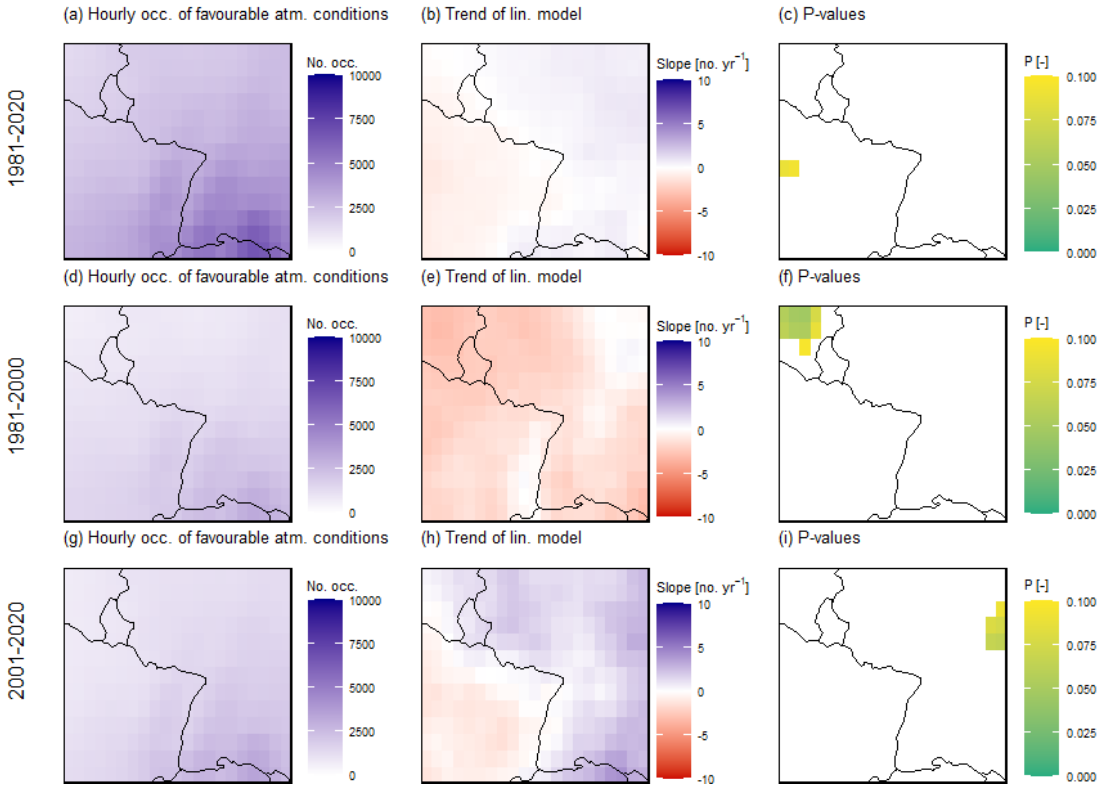

Figure 4.3.5: Panel **(a)** shows the overall number of hourly occurrences of atmospheric conditions favouring extreme precipitation and flash flood events during the summer months between 1981 and 2020, panel **(b)** illustrates the positive trends in atmospheric conditions favouring extreme precipitation and flash flood events per year, and panel **(c)** presents the significance of the linear model. White areas denote insignificance. Panels **(d)** to **(f)** show the same as panels **(a)** to **(c)** respectively, although for the time period from 1981 and 2000; panels **(g)** to **(i)** present the same information for the period from 2001 to 2020.

4.4 Discussion

We numbered P events as one event when the temporal distance between two events exceeded 30 min and the spatial distance exceeded 2 km. This method does not always account for connected events, such as the back-building effects of thunderstorm cells, and may lead to an artefact of counting too many P events. In the case of several P events per day on which a flash flood was identified, only the spatially closest or first P event was determined as flash flood triggering, which may sometimes underestimate the P characteristics leading to a flash flood. However, these phenomena

are considered neglectable in central western Europe, where slow-moving single-cell thunderstorms are the main cause of flash floods, as indicated by the low DLS values identified. This characteristic is in contrast with larger events in the Mediterranean (Gaume et al., 2009) or the US (Gochis et al., 2015).

In the Mediterranean area (Llasat et al., 2016) and lowland catchments of Alpine regions, increases in flash floods have been observed (Sikorska-Senoner and Seibert, 2020). In central western Europe, there is also an increase in the number of reports and scientific publications on flash floods (e.g. Bronstert et al., 2018; Van Campenhout et al., 2015; Marchi et al., 2010; Ruiz-Villanueva et al., 2012). However, as per their nature, flash floods are rare phenomena. Therefore, we are not able to detect any trends based on the data that we have collected. The method of data collection is influenced by the progress of digitalization, which might make recent years appear more often in search engines. Additionally, we browsed through historical archives but did not find further entries. Moreover, any identified trend would be strongly influenced by 2 years in which especially many events occurred: 2016 and 2018 (and possibly the July 2021 floods, which were not considered in this paper but may further strengthen a possible increasing trend). During these event series, atmospheric conditions were characterized by exceptionally long-lasting weather patterns associated with very moist and unstable air masses. These conditions led to the extraordinarily high number and severity of thunderstorms with substantial flooding in central western Europe (Mohr et al., 2020; Piper et al., 2016).

Based on the DWD's RADOLAN data set, we were not able to detect any linear trends in the number of precipitation events per year nor their maximum hourly or 5 min intensities between 2002 and 2020. These findings are in line with similar analyses done by the DWD and GDV (2019). As the detection of extreme precipitation events remained challenging due to their localized occurrence, large-scale data were only available through the deployment of a dense radar station network as of 2002. Note that this observation period remains rather short and does not allow one to infer solid conclusions on potential trends. Also, while weather radars provide precipitation data of high spatial resolution, various sources of uncertainty may prevail, such as those related to precipitation type and intensity, topography, and distance to the radar source (Meischner, 2014; Strangeways, 2007; Winterrath et al., 2017). We accounted for some of these potential effects (e.g. rain gauge adjustments, detection, and correction of possible anomalous propagation echoes). However, perhaps trends in extreme precipitation events could also be detected when considering preceding decades. Müller and Pfister (2011) analysed longer time series starting in 1980 and indeed found an increase in intense rainstorms during the summer months in western Germany (Emscher–Lippe catchment). However, precipitation generally varies considerably on an interannual basis and makes trend analyses challenging. In previous work (Meyer et al., 2020), we analysed 98 daily precipitation station data in the Moselle catchment, which is situated in the west of the study area, over a 65-year period and could not find trends in the daily precipitation maxima nor the number of days with precipitation amounts above $50\,\mathrm{mm\,d^{-1}}$. While the daily precipitation sum should be a reliable indicator of extreme precipitation amounts, the coarse station network probably missed high rainfall amounts that fell in between stations. As both the long-term coarsely resolved data set and the highly resolved

short-term data set did not show clear trends, we could not confirm the hypothesis of an increase in extreme precipitation events within the study area.

We found that atmospheric conditions favouring extreme precipitation and subsequent flash flood events became slightly more frequent, and the intensities of relevant atmospheric parameters increased. The most significant increases were found for the moisture parameters, in line with the assumption of the Clausius–Clapeyron relationships (Lenderink and Van Meijgaard, 2008; Martinkova and Kysely, 2020; Mishra et al., 2012). Both TCWV and q increased significantly over central western Europe, indicating potentially higher precipitation amounts. However, rising air temperatures inhibit an increase in higher RH (Rädler et al., 2018). The increase in q also causes instability parameters, such as CAPE and the K index, to increase at a significant level in some areas. This matches well with the findings of (Taszarek et al., 2021b), who documented an increase in CAPE over central Europe. Trends in CIN are, however, ambiguous within the same period. While favourable conditions do occur more often in some areas, there are indications that CIN increases as well. This increase in CIN might offset some of the instability increases due to CAPE (Taszarek et al., 2021a). In this study, we did not analyse the simultaneous occurrences of CAPE and CIN in detail, but Chen et al. (2020) found highly complex interactions, suggesting that future moist convection and rainstorms may become less frequent but more intense. Regarding low wind speeds and weak DLS, we found sightly increasing but barely significant trends. Increasing trends in weak LLS are significant in the south-eastern part of the study area. Overall, the proxy parameters used for the assessment of organization and motion of storm systems remained largely unchanged, with tendencies favouring the occurrence of extreme precipitation. Studies looking at substantial DLS for other convective hazards, such as hail or tornadoes, also did not identify significant trends in the past over Europe (Púčik et al., 2017; Rädler et al., 2018). Studies investigating future conditions across the US, however, even suggest decreases in DLS (Brooks, 2013; Diffenbaugh et al., 2013). Wind speed and shear are not directly relevant for triggering precipitation, but they can slightly increase the duration of an event; thus, they can potentially contribute to the development of flash floods. The coarse resolution of the ERA5 atmospheric data might miss smaller-scale wind features related to orography. Even though extreme precipitation and flash floods tend to occur locally, they happen during conditions favouring mesoscale to large-scale circulation, which should be well captured by the reanalysis data.

The values of the considered atmospheric parameters cover the expected ranges of occurrence. However, to include 75 % of all precipitation and flash flood events, we had to include an even wider parameter range. This holds especially true for the respective lower and upper thresholds of CAPE and CIN, which appear low and high compared with common values present during thunderstorms respectively (Púčik et al., 2015; Taszarek et al., 2017). In the ERA5 data, both parameters showed an extremely high variability in space and time. This variability in CAPE also leads to a relatively low number of hours with all parameters within their ranges, as shown in Sect. 4.3.5 (Fig. 4.3.5). However, the consistently low values of DLS are striking. While we stated in the beginning, that DLS can be either low or high, this does not seem the case in this region. Extreme rainfall and flash flood events seem to be

consistently caused by slow-moving single-cell thunderstorms. In the US, in contrast, many flood-producing storms are larger and more organized mesoscale convective systems (Ashley and Ashley, 2008; Dougherty and Rasmussen, 2019; Schumacher and Johnson, 2006). The floods considered in US studies are, however, related to rather large and deadly flash floods, whereas flash floods in central Europe generally do not reach comparable dimensions.

The focus of our work was the attempt to link atmospheric conditions, extreme precipitation, and flash floods: we hypothesized that the conjectured increase in flash floods is a consequence of more intense or more frequent precipitation events that are initiated by thunderstorm-favouring atmospheric conditions. However, the reality seems to be a lot more complex. While atmospheric conditions tend to become more unstable and overall warmer air masses potentially possess a higher amount of water vapour, the expected increase in (convective) precipitation events was not obvious from the 20 years of analysed data.

Factors other than those that we have considered in this study may influence the development of flash floods. One such factor could be the duration of thunderstorm-favouring atmospheric conditions. Both remarkable flash flood series from 2016 and 2018 occurred during atmospheric blocking situations (Mohr et al., 2020; Piper et al., 2016) that stymied the movement of the atmosphere, ultimately causing weather constellations to last longer and, thus, creating extreme situations. In recent years, such situations have been increasingly observed, especially in summer (Detring et al., 2021; Kreienkamp et al., 2021; Lupo, 2020). This could hint at a change in the intra-annual distribution of precipitation, while the number of precipitation events as well as their maximum 5 min and hourly intensity stayed – apart from their large intra-annual variations – at a similar level between 2001 and 2020. Sequences with abundant rainfall may eventually cause a catchment's soil moisture to rise and may accelerate the development of a flood event. While low top-level soil moisture before the precipitation events might show the typical pattern of central Europe, where thunderstorms mostly occur after a few warm and dry days, this does not seem to not be the case when flash flooding is caused. The soil moisture is then already elevated at the top layers of the soil to the "average" level by previous rainfall and causes a faster runoff response, including infiltration excess overland flow. Flash floods in continental regions mostly occur when soil moisture is high at the onset of an event (Marchi et al., 2010; Pfister et al., 2020). Moreover, catchment-specific parameters such as topography, land use, soil properties, geology, or other factors may equally impact the development of flash floods (Marchi et al., 2010).

4.5 Conclusions

The goal of our study was to identify and analyse the atmospheric conditions prevailing during extreme precipitation and flash flood events in temperate regions of central western Europe. For this purpose, we compiled a flash flood database based on scientific literature, water agency data, and information from local consultants, and we analysed it using linear regression models. For the identification of extreme precipitation events that could potentially trigger flash floods, we relied on a 5 min

radar data set (RADOLAN, DWD) and analysed all precipitation events exceeding the threshold of 40 mm h^{-1} statistically considering maximum hourly and 5 min precipitation intensities as well as the temporal and spatial coverage of events. The identified flash flood and precipitation events were then connected to convection-relevant atmospheric parameters of the ERA5 reanalysis data set representing instability, moisture content, and storm motion and organization. We leveraged these data for testing our hypothesis that a change in atmospheric conditions has led to more frequent extreme precipitation events that have subsequently triggered flash flood events in central western Europe. It should be noted that the conjectured increase in the occurrence of flash floods could not be tested due to inconsistencies in the database. We tested our hypothesis in two steps:

1. An increase in the frequency and intensity of extreme precipitation events could not be supported with the available database and analysis, due to a large interannual variation in events and a relatively short period of 20 years. Future analyses could incorporate the intra-annual temporal distribution of extreme precipitation events. Perhaps, rainfall events that were formerly evenly distributed now tend to occur in a more condensed fashion (within a few days).

2. Via proxy parameters, we did find changes in the occurrence of atmospheric conditions favouring extreme precipitation and flash flood events. High absolute moisture content (specific humidity, q, and total column water vapour, TCWV) increased significantly between 1981 and 2020, while relative humidity (RH) decreased slightly. Proxy parameters representing sufficient instability (convective available potential energy, CAPE, and the K index) also increased also increased; moreover the convective inhibition (CIN) increased, which might oppose some of the instability gains of CAPE (Taszarek et al., 2021a). Parameters determining weak storm motion and organization (wind speed, $WS_{10\,m-500\,hPa}$, and deep layer shear, DLS) did not show significant changes, but the occurrence of weak low-level shear increased slightly. Overall, the most important components favouring flash-flood-relevant atmospheric conditions, abundant moisture, and sufficient latent instability have become more frequent, and higher values indicate possibly more severe events.

Consequently, only sub-hypothesis 1 is supported, and sub-hypothesis 2 is rejected. Hence, the simple causal chain between atmospheric conditions, extreme precipitation, and flash floods assumed in the overarching hypothesis does not do justice to the entire complexity of problems. Interconnections seem far more complex than hypothesized. In addition to the hypothesis, we mostly found higher upper-layer (0–7 cm) and lower-layer (28–100 cm) soil moisture during flash flood events compared with general extreme precipitation events. These results might point us in other directions, possibly to changes in intra-annual temporal patterns of rainfall and, consequently, different pre-event soil moisture conditions. Another explanation might be non-atmospheric, catchment-specific parameters that were not considered in this study.

To the best of our knowledge, this work is nonetheless among the first studies focussing on the convective hazard of extreme precipitation that has often been

neglected, giving priority to hail or tornadoes. As extreme precipitation is extremely variable in space and time and can derive from many different weather constellations, it remains a challenge to pinpoint atmospheric conditions that trigger these events. This makes possible assumptions about the future extremely challenging.

4.6 Appendix

4.6.1 Spatial trends in atmospheric parameters within central western Europe

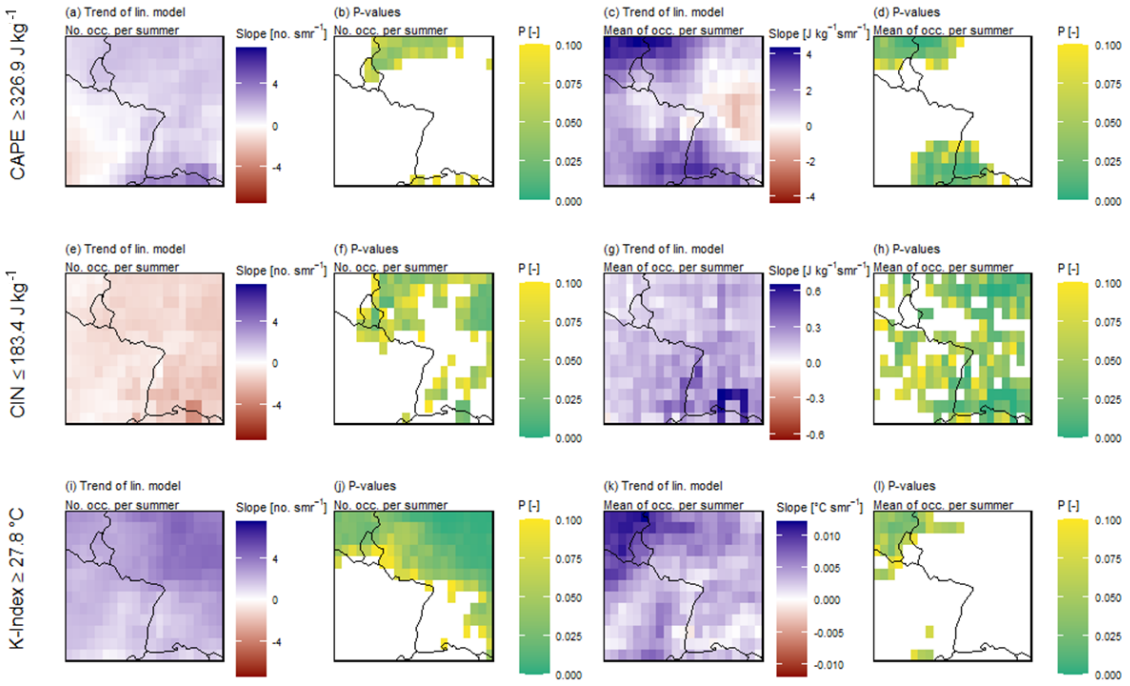

Figure 4.6.1: Trend analysis of the three variables for instability (CAPE, CIN, and the K index) per summer (smr). The first column **(a, e, i)** shows the trends in the numbers of hourly occurrences of values above their respective threshold, and their significance levels are given in the second column **(b, f, j)**. The third column **(c, g, k)** shows the trends in the mean values of all hourly occurrences above the threshold, and the last column **(d, h, l)** presents their respective significance levels. White areas denote insignificance.

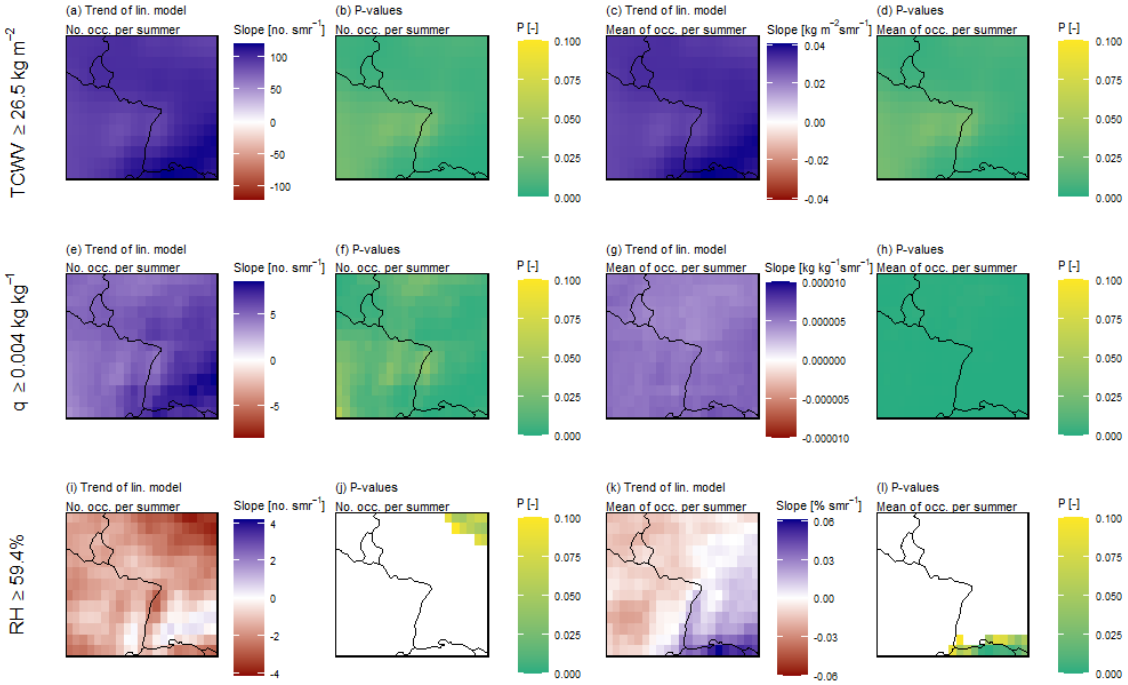

Figure 4.6.2: Trend analysis of the three variables for moisture (TCWV, q, and RH) per summer (smr). The first column **(a, e, i)** shows the trends in the numbers of hourly occurrences of values above their respective threshold, and their significance levels are given in the second column **(b, f, j)**. The third column **(c, g, k)** shows the trends in the mean values of all hourly occurrences above the threshold, and the last column **(d, h, l)** provides their respective significance levels. White areas denote insignificance.

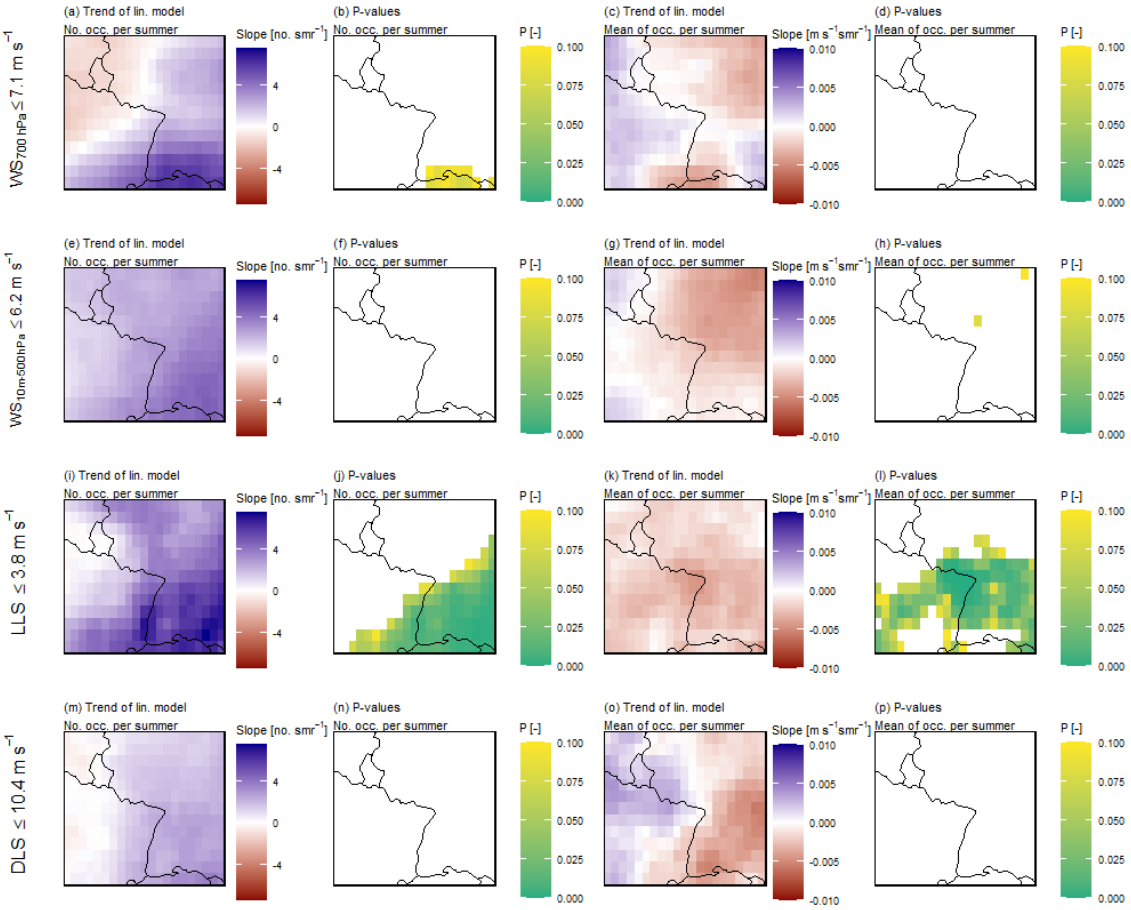

Figure 4.6.3: Trend analysis of the four variables for storm motion and organization ($WS_{700\,hPa}$, $WS_{10\,m-500\,hPa}$, LLS, and DLS) per summer (smr). The first column **(a, e, i, m)** shows the trends in the numbers of hourly occurrences of values above their respective threshold, and their significance levels are given in the second column **(b, f, j, n)**. The third column **(c, g, k, o)** shows the trends in the mean values of all hourly occurrences above the threshold, and the last column **(d, h, l, p)** presents their respective significance levels. White areas denote insignificance.

5

Challenging LSTMs in Summer Flood Modelling in Central Western Europe

The simulation or even forecasting of flash floods becomes increasingly important under potentially intensifying hydrological conditions. The simulations of these events are however very difficult due to the rare nature of the events and the incomplete understanding of runoff mechanisms during extreme precipitation events. We therefore challenge LSTMs in summer flood modelling to test, whether the machine learning algorithm is potentially able to extract the relevant mechanisms needed for an accurate simulation of summer peak flow. We set up the model based on the CAMELS-LUX data set presented in Chapter 2. To additionally improve the representation of thunderstorm conditions, we make use of the understanding of the underlying atmospheric conditions gained in Chapter 4 and provide the atmospheric parameters as input. This relation between atmospheric proxy parameters and discharge can barely be mapped in conceptual hydrological models.

This chapter is based on:

Nijzink, J., Loritz, R., Zoccatelli, D. and Pfister, L.: Challenging LSTMs in summer flood modelling in central western Europe (Luxembourg) [in preparation].

Author contribution:

JN, RL, DZ conceptualized the study. RL provided the model code. JN did the simulations and analyses and wrote the first draft. All the co-authors (JN, RL, DZ) contributed to and edited the manuscript.

5.1 Introduction

The robust simulation and forecasting of flash floods is a major challenge in hydrology due to their rapid and localized nature (Marchi et al., 2010). Within recent years, this issue became increasingly relevant, as weather conditions leading to intense convective precipitation and subsequent flash flooding have caused great disturbances in central western Europe (Pfister et al., 2018, 2020; Johst et al., 2018). In the preceding decades, floods in this region had been characterised by slowly developing large-scale inundations during the winter rather than faster runoff responses following thunderstorms (Pfister et al., 2000). Most hydrological model structures are therefore designed to capture the dimensions of storage-controlled winter floods in mesoscale catchments and struggle to translate the signals of convective events that potentially trigger flash floods in smaller streams. This mis-representation of flash floods is mostly owed to the rare nature of these events in central western Europe and the differing and poorly understood runoff mechanisms.

Within recent years, data-driven neural networks have demonstrated in various cases that they can reproduce hydrological relationships, such as catchment-wise rainfall-runoff behaviour (Lees et al., 2021; Frame et al., 2021; Kratzert et al., 2019b). Among the differing neural networks, Long Short-Term Memory (LSTM) models are particularly suitable for hydrologic modelling, as the two memory states represent faster runoff components and base flow respectively (Kratzert et al., 2019a). The data-based LSTMs process large amounts of information with which they reproduce the output of hydrological systems free of predefined assumptions about the underlying conceptual or physical processes. This opens opportunities to take advantage of the ever-increasing amount of available data, that are related in complex physical or conceptual ways that remain poorly understood. However, relying purely on data, the amount and quality of the training is crucial. To feed the need for training data, LSTMs are trained across multiple basins. This has advantages when simulating extreme events, as the chance, that the LSTM has already been trained on a comparable extreme event within in another catchment is much higher when considering many catchments. This transferability might help to overcome the difficulties involved with rare events (Bertola et al., 2023; Nearing et al., 2024).

The skills of regional LSTMs remain however limited with regard to the simulation of flash floods. The prediction error generally increases with the height of the flood peak (Frame et al., 2021; Oddo et al., 2024). However, Frame et al. (2021) found that data-driven models generally performed better than their benchmarking models in many cases. They outperformed them during flood peaks that were below the maximum flood peak in the training data set but also for peaks exceeding this maximum. Feng et al. (2020) simulated flashy streams in arid basins in Texas applying an LSTM trained on the CAMELS-US data set (Addor et al., 2017). Yet, even applying additional data integration techniques to the LSTM, they were not able to improve the simulations of these peak flows. Oddo et al. (2024) set up an LSTM in a river network known for the regular occurrence of flash floods in Maryland, US. They could improve the model error during peak flow by 26% using a hybrid Convolutional LSTM. They further found, that a shorter sequence length can improve the peak simulations in some cases. Another study focussed on the

simulation of flash floods triggered by tropical cyclones in the Wu River in Taiwan (Jhong et al., 2024). To further improve the LSTM they optimized the LSTM using a genetic algorithm. With this set up they also found that the simulations becomes more accurate the shorter the lead time. This is due to the optimization algorithm that focusses on surface runoff processes and does not have to consider subsurface flow components. Song et al. (2020) trained LSTM models solely on flood events (in total 75) in the Anhe catchment in south-eastern China, directly neglecting any sub-surface or base flow components during the rest of the year. With this approach a quite accurate simulation of the floods was achieved. However, the latter and more successful studies do not simulate floods at a temporally continuous and spatially extended scale.

Because of the sudden changes of discharge within hours, which is typical for summer peak flows, it is crucial for models to represent sub-daily temporal intervals. So far, only a few studies applied regional LSTMs on a sub-daily scale. Gauch et al. (2021) and Wilbrand et al. (2023) compared LSTM performances on multiple time scales and found that the LSTMs are capable of learning hydrological behaviour despite the longer sequence length needed to train hourly models. The results of daily and hourly models vary, but are more or less comparable regarding the overall performance measures.

In this study, we evaluate the performance during flood events of the CAMELS-LUX benchmark LSTM (Sect. 2.6.2) and keep a particular focus on the simulation of summer peak flow events. Our first hypothesis is therefore: An hourly resolution improves the model performance during summer peak flow events. Making use of the LSTMs flexible model structure, we additionally include atmospheric variables in the modelling process to better characterize the atmospheric conditions potentially leading to summer peak flow events. This supplementary information can support simulations, when precipitation data is underestimated. Our second hypothesis is that including atmospheric variables relevant for extreme precipitation improves the simulation of summer peak flow events.

5.2 Study area and data

The study area is Luxembourg and the data set used for the study is the CAMELS-LUX data set. For an in-depth description of the study area and the data set, we would like to direct the reader to Chapter 2.

5.2.1 Study area and period

The study area comprises 56 partly nested catchments between 0.458 km^2 and 4256.623 km^2 that contribute to the Luxembourgish stream network. This includes areas from almost all of Luxembourg and a few headwaters in Belgium, France and Germany. The study area can be divided into two broad geographical regions: The Oesling in the North and the Gutland in the South. The Oesling region forms a part of the Ardennes massif. The region is characterized by steep slopes, a schistose geology, extensive forests and is only sparsely populated. The Gutland region, on

the contrary, is characterized by rolling hills in permeable sandstone and marl formations, that create the conditions for extended agriculture and urban areas (Chapter 2). The hydrological response of the catchments is especially determined by the underlying geology (Pfister et al., 2017).

The climate conditions in Luxembourg are homogeneous over the entire study area. The climate is classified as a temperate oceanic climate with annual mean air temperatures between 9 and 10 °C and annual precipitation totals around 850 mm. Slightly higher monthly precipitation amounts fall during the winters and are related to westerly flow patterns (Pfister et al., 2004). Summer precipitation can occur based on advective processes, as well as convective processes. Hydrological processes related to snow are minor (Pfister et al., 2000, 2005).

The study period was set to the hydrological years from 1 Nov 2004 to 31 Oct 2021, as most stream gauges were available during this time. The study period includes several high flow periods, that are linked to both, large-scale winter inundations and short streamflow peaks during the summer. The temporal resolutions of the analyses are daily and hourly.

5.2.2 Hydro-meteorologic time series

We used discharge data from 56 stream gauges that feed into a Luxembourgish river. This inventory comprises stations from the Luxembourgish Water Agency (AGE), the Luxembourg Institute of Science and Technology (LIST) and the Rhineland-Palatine State Office for Environment (LfU-RLP, 2022). The data was aggregated from an original temporal resolution of 15-minutes to hourly and daily time steps. Most major floods in the CAMELS-LUX data set are related to large-scale winter floods, while several flash floods stand out during the last years of the study period. The events differ substantially in their mechanisms being either storage-controlled and stretching over several days in winter or triggered by extreme precipitation events leading to highly dynamic runoff reactions in summer. One outstanding flood occurred in July 2021 and reached new maxima in almost all of the catchments.

Precipitation input data was calculated from the quasi-gauge adjusted radar data set RadKlim of the German Weather Service (Winterrath et al., 2018). The data is available at a 1x1 km spatial resolution at a 5-minute time interval. For each of the study catchments a spatial mean was calculated and the temporal resolution was aggregated to hourly and daily values. We also supplied the 5-minute minimum and maximum grid cell during the temporal interval to better assess the rainfall intensity during events.

Atmospheric and soil moisture data were retrieved from the ERA5 data set (Hersbach et al., 2018b,a; Muñoz Sabater, 2019). According to our previous findings (Meyer et al., 2022), we used a total of 9 proxy parameters (Chapter 2, Table 2.2.1) for atmospheric instability, atmospheric moisture contents, system motion and organization to characterize extreme precipitation events with the potential to trigger flooding. Moreover, we used soil moisture contents at four different depths. The horizontal grid width of the ERA5 atmospheric data is 0.25° x 0.25° and of the land data 0.1° x 0.1°.

The measured data was quality controlled and data gaps were closed. Small

gaps in discharge data were linearly interpolated and larger gaps replaced with the spatially adjusted specific discharge of surrounding stations that behave comparably. Gaps in the RadKlim data set were filled with data from an interpolated station network consisting of 70 stations. Filled data gaps were marked in respective flag columns and supplied as additional input data.

5.2.3 Catchment attributes

To characterize and classify the catchments, static catchment attributes were assigned to each catchment. In this study, we applied:

- Catchment size and geometry: Area [km^2], perimeter [km], Gravelius compactness coefficient (KC) (Gravelius, 1914)
- Five geology classes: Limestone and dolomites, surface deposits, sandstone conglomerates, marl and claystone, schists and quartzites
- Five land use classes: Watercourses, waterbodies and wetlands, forests and natural areas, grassland, agricultural land, urban areas
- Measures for a topographic placement: elevation range, maximum slope, Network Development and Persistence Index (IDPR), topographic wetness index (TWI), Vector Roughness Measure (VRM) that are described in detail in Chapter 2.

5.3 Methods

5.3.1 Long Short-Term Memory network

A Long Short-Term Memory (LSTM) network is a specific type of a recurrent neural network (Hochreiter and Schmidhuber, 1997). The LSTM cell structure is designed in a way, that can maintain two memory states – hidden state and cell state – to simulate short-term and long-term dependencies between input and output data. The two states are updated at every time step depending on the input data that is being passed through three gates. A gate contains a linear activation function that determines the impact of each input sample to the states and the output value. The forget gate determines the percentage of the long-term memory to be remembered depending on the short-term memory and the input. The input gate defines the potential long-term memory as well as the percentage to which it will be remembered. Through the output gate, the short-term memory is updated based on long-term memory and the previous short-term memory. The new short-term memory is the output value (Gauch et al., 2021; Kratzert et al., 2018; Anderson and Radić, 2022). This combination of short-term and long-term memory makes LSTMs especially useful for simulating streamflow, where the short-term memory represents the faster (surface) runoff components compared to the long-term memory, that corresponds to base flow or snow accumulation (Kratzert et al., 2019a, 2018). For more technical details of the functioning of LSTM cells and networks in hydrology, we refer the reader to Kratzert et al. (2018).

5.3.2 Model setup and training

The LSTM hyperparameters used during the training process compare closely to previous studies by Frame et al. (2021), Espinoza et al. (2023), Gauch et al. (2021), Lees et al. (2022). The model target (streamflow) was predicted by a sequence-to-one prediction with a sequence length of 365 days for the daily model. With a batch size of N = 256, samples were drawn from the 56 different basins (b). The LSTM was trained to optimize the area-averaged Nash-Sutcliffe Efficiency NSE*. This adaptation from the Nash-Sutcliffe Efficiency was applied according to Kratzert et al. (2019c) to avoid a higher weighting of large humid catchments compared to catchments with lower mean discharge. It implies a standardization of the NSE based on the standard deviation per basin (s_b). A constant ϵ (ϵ=0.1) is added to anticipate a divergence to negative infinity in catchments with a very low variance of discharge. NSE* is calculated according to the following equation:

$$\mathrm{NSE}^* = \frac{1}{B}\sum_{b=1}^{B}\sum_{t=1}^{T}\frac{(Q_{\mathrm{obs},b} - Q_{\mathrm{sim},b})^2}{(s_b + \epsilon)^2} \tag{5.1}$$

where B represents the number of basins, T the number of time steps per basin, $Q_{\mathrm{obs},t}$ and $Q_{\mathrm{sim},t}$ the standardized observed and simulated discharge of the basins at time step t respectively, s_b the standard deviation of the discharge in basin b. The LSTM was trained during 30 epochs with an initial learning rate of 0.001, that was adapted with a gamma learning rate of 0.8 every 5 epochs. Moreover, a dropout rate of 40% and a hidden size of 64 were applied. Training an hourly model is computationally much more demanding and convergence to a better loss function efficiency can be less monotonous due to longer sequence lengths. In order to find a good balance between a properly trained model, training times and hydrologically relevant time periods, we nonetheless opted for training the model during 30 epochs, as after 20 epochs there was still potential for further improvement in most cases. The sequence length in the hourly model was 720 hours (30 days), which we assumed to be sufficient for this study's focus on summer peak flow. Doubling the sequence length already doubled the calculation times.

Different testing and training periods were tested. For the core of the results we chose a training period from 1 Nov 2008 to 31 Oct 2016. This period was chosen to include a major winter flood (e.g. 2011) and the first few flash floods (2016) occurring later on, assuming to cover the variety of the system. The testing period is accordingly from 1 Nov 2004 to 31 Oct 2008 and 1 Nov 2016 to 31 Oct 2021.

5.3.3 Modelling approach

First, we set up a regional LSTM system for all gauged catchments (56) with relation to Luxembourg using the CAMELS-LUX data set following the model setup and training described above. As input parameters, we relied on basic hydrological parameters (precipitation from radar and station data, including derived maximum intensities and flags, reanalysis temperature data and specific discharge). In order to improve the model performance during peak flows and especially summer peak flows, we tested three approaches: (1) First, we increased the temporal resolution

of the simulations from daily to hourly time steps. This was done to better reproduce the highly dynamic summer peak flows that are often hard to capture with daily time steps. (2) Secondly, we added atmospheric parameters relevant for thunderstorm favouring environments by systematically combining parameter groups for atmospheric instability, atmospheric moisture, atmospheric motion (wind and shear) and also soil moisture data. (3) Last, we have artificially doubled the precipitation input during the periods of four selected events. This was done to exclude a potential underestimation of the precipitation as cause for failing peak flow simulations.

5.3.4 Evaluation measures

Table 5.3.1: Model evaluation measures.

Metric	Description	Equation	Reference
NSE [-]	Nash-Sutcliffe-Efficiency	$\mathrm{NSE} = 1 - \frac{\sum(Q_{\mathrm{obs}} - Q_{\mathrm{sim}})^2}{\sum(Q_{\mathrm{obs}} - \overline{Q}_{\mathrm{obs}})^2}$	Nash and Sutcliffe (1970)
ΔQ_p [-]	Peak distribution Peak flow (1-5%)	$\Delta Q_p = \frac{\left(\frac{Q_{p,\mathrm{sim},1} - Q_{p,\mathrm{sim},5}}{0.99-0.95}\right) - \left(\frac{Q_{p,\mathrm{obs},1} - Q_{p,\mathrm{obs},5}}{0.99-0.95}\right)}{\left(\frac{Q_{p,\mathrm{obs},1} - Q_{p,\mathrm{obs},5}}{0.99-0.95}\right)}$	In Euser et al. (2013)
FHV [-]	Top 2% peak flow bias [Flow duration curve High segment Volume]	$\mathrm{FHV} = \frac{\sum_{h=1}^{H}(Q_{\mathrm{sim},h} - Q_{\mathrm{obs},h})}{\sum_{h=1}^{H} Q_{\mathrm{obs},h}} \times 100$ h = 1, 2,.. .H are the flow indices for flows with exceedance probabilities lower than 0.02.	Eq. A3 in Yilmaz et al. (2008)
$\mathrm{RE}_{Q5\%}$ [-]	Absolute percentual error of peak height	$\mathrm{RE}_{Q5\%} = \mathrm{mean}\left(\frac{\lvert Q_{p,\mathrm{obs}} - Q_{p,\mathrm{sim}}\rvert}{Q_{p,\mathrm{obs}}}\right)$	As used in Frame et al. (2021)
Δt_{Qp} [h]	Mean peak time lag between observed and simulated peaks	$\Delta t_{Qp} = t_{\mathrm{peak},Q_{\mathrm{obs}}} - t_{\mathrm{peak},Q_{\mathrm{sim}}}$	Appendix B in Kratzert et al. (2021)

Q_{obs}: observed discharge; Q_{sim}: simulated discharge; Q_p: peak discharge

We evaluated the LSTM model performance during the testing periods using different evaluation measures (Table 5.3.1). As basic measure for general model performance, the Nash-Sutcliffe-Efficiency (NSE) was used (Nash and Sutcliffe, 1970). To assess the peak flow, different specific evaluation measures were analysed. The first and most general measure is the peak distribution (ΔQ_p) (Euser et al., 2013).

To calculate it, all local maxima (as well as the ones during summer and winter months respectively) of the observed and simulated discharge are sorted. The resulting curves are then analysed with respect to the difference in slope between the highest 1% and 5% of the sorted peaks to account for high flow conditions. Apart from that, the top 2% peak flow bias (FHV) evaluates the error of the highest 2% of the flow duration curve of the simulations (Yilmaz et al., 2008). The absolute percentual error of peak height ($RE_{Q5\%}$) evaluates the peak difference per event (Frame et al., 2021). We considered the top 5% of all local maxima as peaks for the annual analyses and the top 5% of the local maxima during summer and winter months respectively. Moreover, we determined the peak timing (Δt_{Qp}) - the difference between the time of the observed and the time of the corresponding simulated peak. Each evaluation measure was calculated for the entire year, as well as in the summer (May-August) and the winter (September-April). The selection of the summer months was based on the flash flood data base (Table S3.1). For an additional analysis regarding extreme flood events, we have compared the absolute maxima of differing training and testing periods of the observed and simulated data.

5.4 Results

5.4.1 Summer and winter flood evaluation

A significant difference in performance was found between summer (May-August) and winter (September-April) (Fig. 5.4.1, and Appendix Fig. 5.7.1 - Fig. 5.7.3). The simulations during the winter generally reach very high NSE, ranging above 0.8 with very little variation among the 56 catchments (Fig. 5.4.1 a). In contrast, during the summer, the variation of NSE values shows a quite high range among the catchments and is on average lower, mostly ranging between an NSE value of 0.6 and 0.8. This remarkable difference in performance is particularly evident when evaluating peak flows in Fig. 5.4.2 (a-b exemplary for a well-simulated winter flood, and c-k for three different summer peak flows). The first winter peak (Fig. 5.4.2 a-b) is well simulated, whereas the summer peak flows are completely missed (Fig. 5.4.2 c-k). The absolute percentual error of peak height ($RE_{Q5\%}$) is notably higher for peak flows in summer compared to the peak flows during the winter (Fig. 5.4.1 d). Differences between summer and winter peak flows are less pronounced regarding the peak distribution for the 1% to 5% highest discharge values (Fig. 5.4.1 b). Comparing the flood volumes, the top 2% peak flow bias (FHV) indicates a continuous underestimation of the peak flows, that is more pronounced in summer (Fig. 5.4.1 c).

5.4.2 Improving summer peak flow modelling

Increasing the temporal resolution of the model

Increasing the temporal resolution of the model simulations from daily to hourly results in minor reductions of the overall model efficiency measured by the NSE (Fig. 5.4.1 a). When comparing the performance of the highest flows $\Delta Q_{p,1-5\%}$ and FHV, the performance of both, the daily and the hourly model are quite comparable in

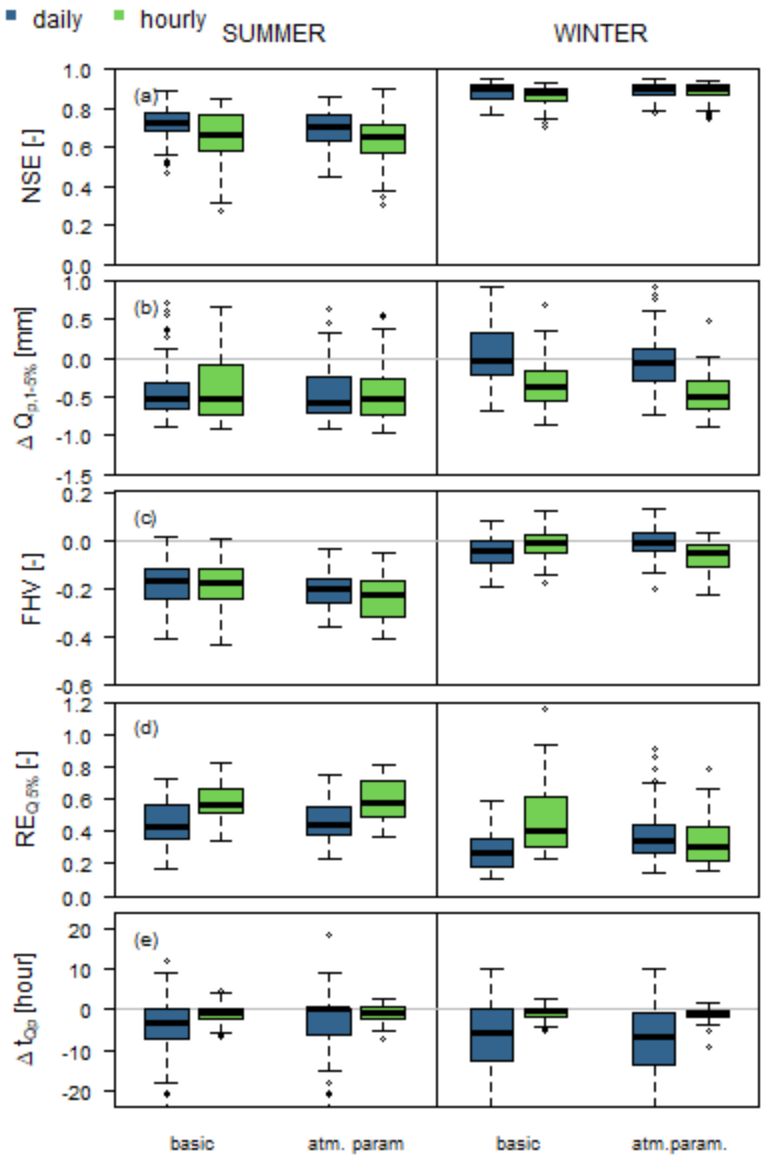

Figure 5.4.1: Performance measures of the evaluated model runs for all catchments comparing summer (left column) and winter (right column) performances. The left boxplots (blue) of each group show the daily resolution and the ones on the right (green) the hourly resolution. While the first groups are model runs based on only basic input parameters (precipitation, air temperature), the second group includes all parameters (atmospheric and soil moisture).

summer Fig. 5.4.1 b, c). Yet, during winter events the hourly model (green boxes) underestimates the peaks slightly more than the daily model (blue boxes). The absolute percentual error of peak height ($RE_{Q5\%}$) is slightly higher for the hourly simulations (Fig. 5.4.1 d). The hourly simulations are much more precise, when comparing peak timing (Δt_{Qp}), that is mostly met within 1-2 hours (Fig. 5.4.1 e). The daily resolution naturally shows a wider spread due to the coarser temporal

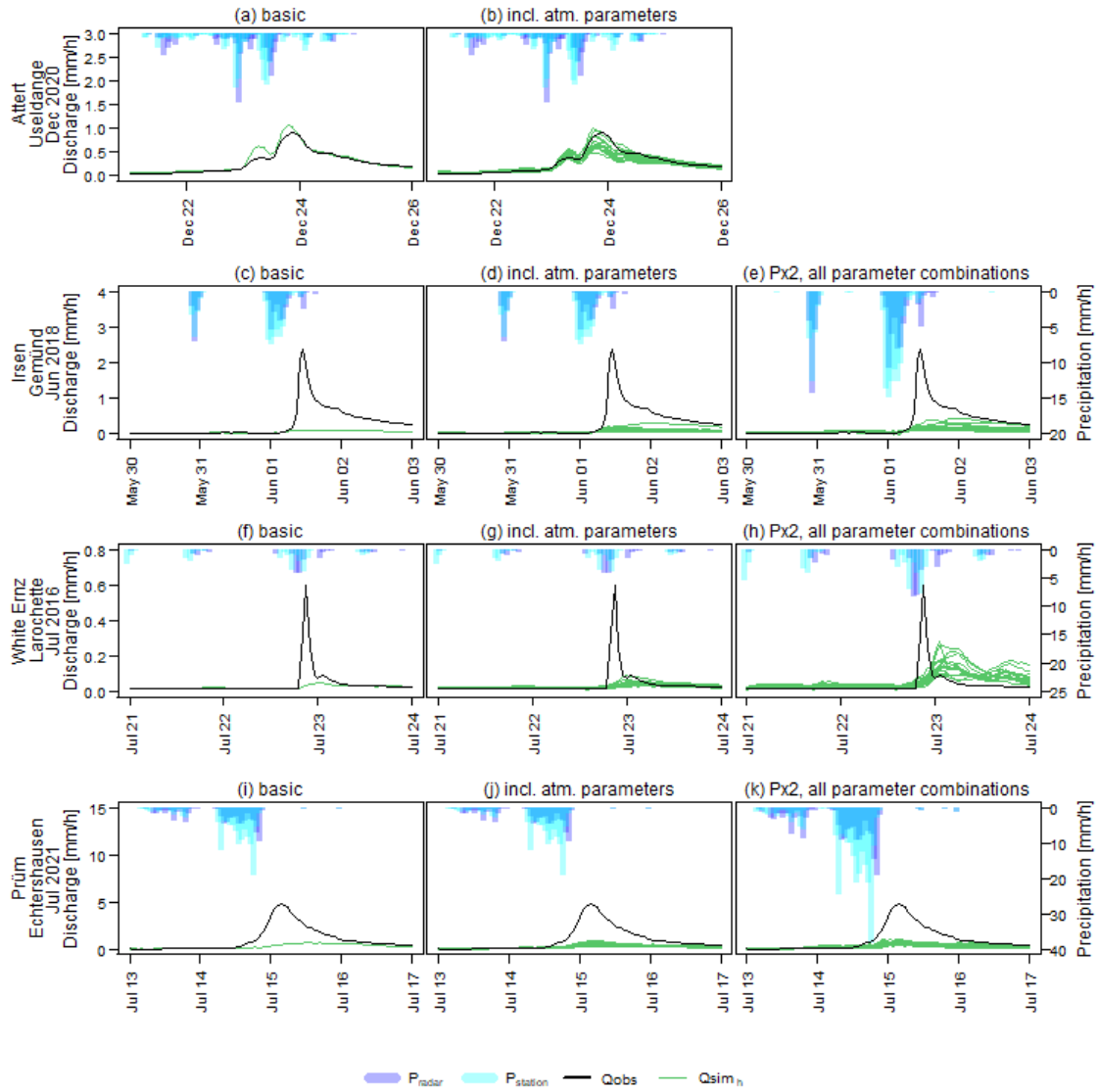

Figure 5.4.2: Exemplary selection of a few specific floods within the data set. Each row belongs to one event described on the left. The simulations show the hourly resolution.

resolution, but most peaks are timed within the range of a day before or after.

Including atmospheric parameters

Additionally including soil moisture and atmospheric parameters that further characterise and identify thunderstorm environments does not substantially improve the simulations of (specific) summer peak flows being triggered under thunderstorm conditions (Fig. 5.4.1, Fig. 5.4.2, d, g, j). The most substantial improvements are found for the parameter combination including the parameter sets representing atmospheric instability, atmospheric moisture, and wind (Appendix Fig. 5.7.2). These improvements are however not translated into all model evaluation measures and do not

make the model significantly better than the others. All these model runs show similar results to the previous model runs without atmospheric input parameters, which raises confidence in the general robustness of the LSTM.

Artificially doubling precipitation in the input data

In order to account for potentially underestimated precipitation input, we have performed test runs with doubled precipitation input data for a selection of summer peak flows that were totally missed by the model (Fig. 5.4.2 e, h, k). With that input, we were able to trigger runoff reactions during the flooding events. Yet, none of these reach up to the actual observed discharge.

5.4.3 Extreme peak flow events (July 2021)

Simulating the extreme and widespread flood event of July 2021, caused major problems for the LSTM. While this event was captured to a certain extent when it was in the training data set, leaving the event out of the training data set and extrapolating was not successful. In all catchments, where the specific discharge during the event was high, the model underestimated the flood peak. Even artificially doubling the rainfall amounts during the highest events did not result in higher discharge maxima (Fig. 5.4.2 k). Assessing the maxima of the training and testing periods (Table 5.4.1), it is clear, that the LSTM did not simulate discharge close to the maxima reached in the observed data. The highest simulated discharge was achieved with 37 mm/d, in the model run that included the July 2021 flood event in the training data. However, discharge higher than 37 mm/d was observed in 11 catchments during the this flood event.

Table 5.4.1: Maximum daily observed ($Q_{obs,max}$ [mm/d]) and simulated ($Q_{sim,max}$ [mm/d]) discharge and maximum hourly observed ($Q_{obs,max}$ [mm/h]) and simulated ($Q_{sim,max}$ [mm/h]) discharge during different training and testing periods.

	Training 2004-2013	Testing 2013-2021	Training 2013-2021	Testing 2004-2013	Training 2008-2016	Testing 2004-08 &16-21
$Q_{obs,max}$, daily	33.67	68.16	68.16	33.67	33.67	68.16
$Q_{sim,max}$, daily	23.28	21.27	37.16	24.58	25.48	23.21
$Q_{obs,max}$, hourly	3.21	7.78	7.78	3.21	3.21	7.78
$Q_{sim,max}$, hourly	2.45	2.24	4.92	3.46	2.53	2.31

5.5 Discussion and Outlook

Just as the benchmark model presented in Chapter 2, also slight variations with respect to the input time series or the temporal resolution still led to reasonable

model performances throughout the study area. The general model performance of the daily and hourly annual NSE evaluation between 0.4 and 0.9 is in line with the performance range of LSTMs based on the CAMELS data set (Kratzert et al., 2021), while the LSTM based on CAMELS-GB yields slightly better performances (Lees et al., 2021). The model performance clearly diverges under summer and winter conditions.

To a large extent, winter floods are well simulated by the LSTM model. The storage-controlled floods, that are triggered by large-scale precipitation events and accumulated soil moisture are characteristic for the winter in Europe. These characteristics make them generally a bit easier to predict than very local extreme precipitation triggered peak flows. Moreover, the sample size of storage-controlled floods (i.e. the number of these flood events) is much higher in the CAMELS-LUX data set, giving the data-based model higher chances to learn the flood pattern. The lower performances in the hourly simulations during higher flow conditions in the winter might be linked to the relatively short sequence length of just 30 days, that might not fully do justice for a good representation of the base flow and storage level.

Simulating summer peak flow appears much more complex. The general peak flow evaluation measures are continuously lower than for the winter peak flow events. The signals of some events were even completely missed. Increasing the temporal resolution from daily to hourly simulations helped to better capture the peak timing, which is not very surprising considering the dynamic nature of the events. Assuming that the quality of the precipitation input might not be enough to trigger the resulting peak flow, we have added soil moisture data and atmospheric proxy parameters characterizing thunderstorm environments. However, even with this additional information about summer peak flows, simulations did not improve significantly.

One possible explanation as to why the LSTM has completely missed a few of the summer peak flows might be, that the precipitation is underestimated during peak events in the RADKLIM data set (Kreklow et al., 2019; Pöschmann et al., 2021). Accounting for that, we additionally provided the 5-minute maximum intensity and precipitation station data incorporated in the CAMELS-LUX data set. While heavy precipitation events often appear weaker on the radar because of the high intensity, the coarse station network might miss the centre or timing of localized storm cells. Yet, even artificially doubling the precipitation input did not increase the flood peaks to reach the observed discharge in a few cases. This confirms the difficulties of the LSTM to capture the flood peaks in general. Another explanation could be the often drier conditions during summers. Kratzert et al. (2018, 2019b) indicated that less rainfall-runoff information is available in arid regions due to long low flow periods. Also in the for the relatively dry South-East of Great Britain (compared to the rest of the CAMELS-GB data set)(Lees et al., 2021) and in arid Southern Texas, where intermittent streams are "activated" in flash floods (Feng et al., 2020), LSTMs are not performing well. Luxembourg is not an arid region, yet, we hypothesize that the underlying model problems, of not well capturing possible mechanisms of hydrophobic soil reactions, infiltration excess overland flow or other mechanisms might be related to the drier conditions in summer. However, these conditions are rare and possibly not well represented in our training data set.

The number of 56 catchments for the modelling may be considered relatively low.

However, it is not exactly clear how many catchments are needed to have a good sample for large-scale hydrology (Kratzert et al., 2024; Wilbrand et al., 2023). In addition, we argue, that the wide geological variety of catchments adds a good component of diversity. The climate is homogeneous throughout the study area, so we consider the setup a valid approach for regional modelling in temperate Europe. Regarding extreme summer peak flows, which remain rare by nature, it could, however, be beneficial to include more catchments to increase the sample size of these events (Qi and Majda, 2020; Bertola et al., 2023). Tests of varying our training period have shown how important it is to include the extreme events between 2016 and 2021 in the training data, even though no testing is possible. Especially, with potentially increasing occurrences of extreme summer peak flow, more extreme events, possibly from other catchments, should be included in the training data set for reliable training. Very simple (and not shown) attempts of artificially increasing precipitation and discharge in either just one or ten catchments of the CAMELS-LUX data set in order to have training data outside the range of the observed data did not lead to the result of an improved simulation of extreme peak flow.

Regarding the simulation of the extreme large-scale flood event in July 2021, we seem to have reached the saturation of the LSTM. The discharge simulations of the LSTM always remain under the actual values that were observed in the training period. In addition, there were generally no extrapolations beyond the training data. These findings contradict a previous study by Frame et al. (2021), where it was shown that extreme, out-of-sample events can be simulated better than with conceptual models. The saturation problem is likely irrelevant when using enormous global data sets including enough catchments of all climate zones, such as the LSTM run on the FloodHub by Google (Nearing et al., 2024), but it is a major limitation at the smaller scale. Basically, it excludes the use of LSTMs at regional scale for predictions outside the range of the training data, such as under non-stationary climate conditions.

Nonetheless, we consider the presented LSTM model a basic and functioning benchmark model, that has the potential to be extended in many directions. An even higher resolution of the data is available for CAMELS-LUX. While the computational power to train an LSTM at the 15-minute resolution is very demanding, one could adjust the model structure by keeping daily data in the cell state for seasonal catchment connectivity and storage. These cell states can be passed on to hourly and 15-minute resolutions at a certain value of the sequence length to better account for the fast runoff components (Gauch et al., 2021). This could substantially reduce the sequence length, giving the model a chance to learn both, annual hydrology and direct runoff reactions to precipitation. Another way forward could be the training efficiency. Here, the area-averaged Nash-Sutcliffe efficiency was used, that is being biased towards well capturing flood events with high volumes. A stronger weighting of summer floods in the later epochs of the training could sensitize the LSTM to react to flashy peak flow in relatively dry conditions. The finetuning of the training process should be guided by expert knowledge (Nearing et al., 2019). In case the LSTM succeeds at capturing summer peak flow events, it would moreover be interesting to extract the information about the mechanisms that the LSTM learnt and applied when simulating them (Lees et al., 2021).

5.6 Conclusion

Considering the increasing importance of a precise simulation of summer peak flow events, the goal of this study was to analyse and improve the simulation of summer peak flow events in and around Luxembourg. We therefore challenged the LSTM set up based on the CAMELS-LUX data set and tested two approaches:

First, we tested the hypothesis that an hourly resolution improves the model performance during summer peak flow events. Increasing the temporal resolution naturally improved the hydrograph reconstruction of highly dynamic summer peak flow events. However, the overall performance of the LSTM considering the flow volume and peak height during peak flow conditions decreased slightly compared to the daily data. Yet, the precision gained by the smaller time step is crucial, even though the evaluation measures show slightly lower values.

Secondly, we tested, whether we could compensate for potentially underestimated precipitation by further characterizing the atmospheric conditions during thunderstorm events. To do so, input parameters were included that represent a combination of parameters for atmospheric moisture, atmospheric instability, system motion and organization as well as soil moisture at four depths. With these input variables, we tested our hypothesis that including atmospheric variables relevant for extreme precipitation improves the simulation of summer peak flow events. While during some events adding the additional parameters helped the simulation of peak flow, it did not for other events. Neither was any specific combination of parameters performing consistently better. Overall, we have to reject our hypothesis as the atmospheric parameters did not substantially improve the simulations to capture the flood peak.

Focussing on extreme events, we found a continuous underestimation of flood peaks. This underestimation was more evident for extremer events. We therefore conjecture that this saturation occurs due to the rare nature of extreme events, because there are not enough comparable events in the data set to properly train the LSTM for their simulation.

We therefore conclude, that correct precipitation data is absolutely crucial to properly simulate summer peak flow events. Moreover, we conjecture, that the differing runoff mechanisms during summer peak flow compared to storage-controlled winter floods are not sufficiently represented in the training data set. To get extreme events right, the training data would have to be extended to a higher number of events within the high range - either by including more catchments or by using synthetic data.

5.7 Appendix

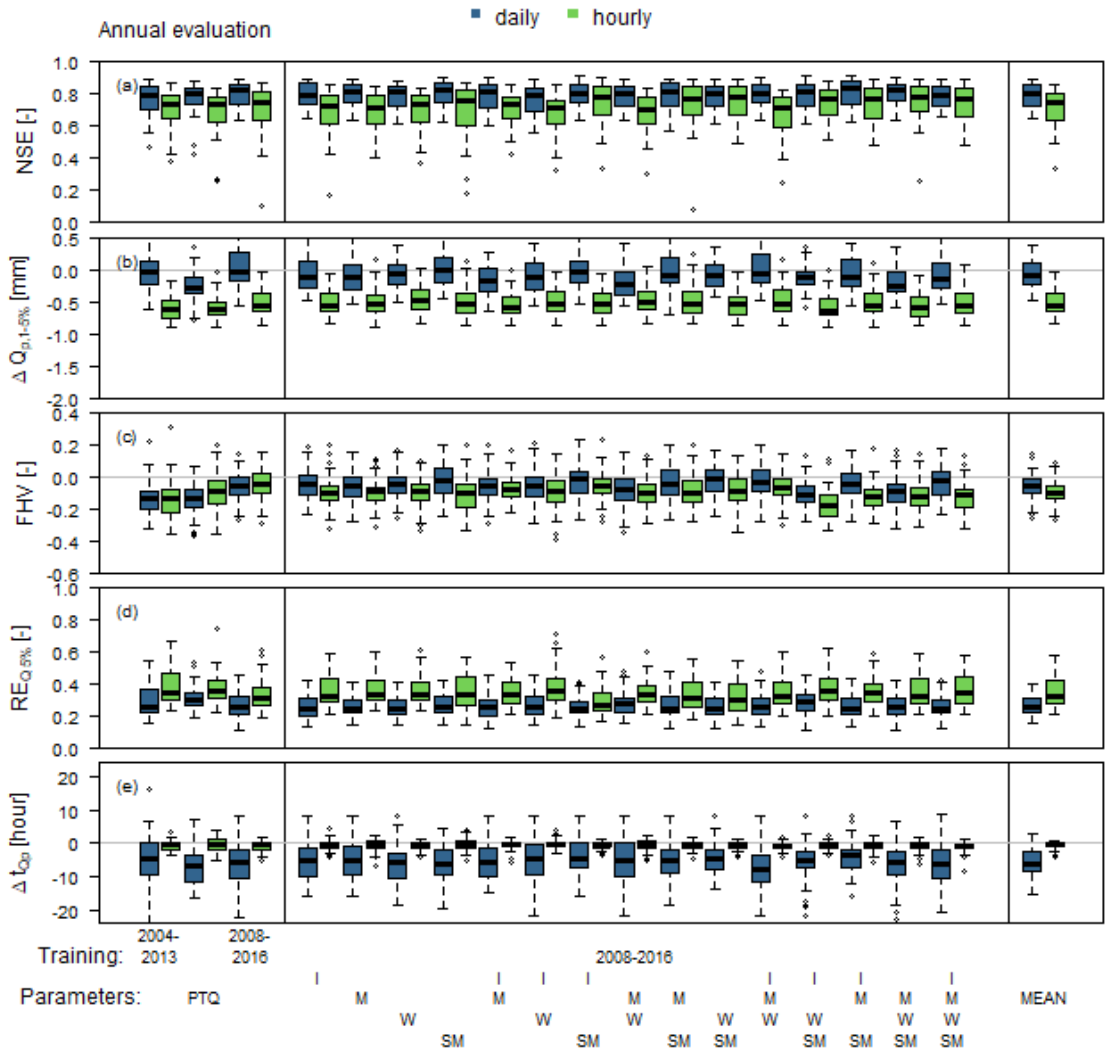

Figure 5.7.1: Annual evaluation measures for all model runs. While the blue boxplots show the daily data, the green ones on their right show the results of the same model settings, but at hourly resolution. The parameter combinations all involve precipitation, air temperature and specific discharge (PTQ) for training. In addition, atmospheric parameters are added at the model runs shown in the middle column referring to atmospheric instability (I), atmospheric moisture (M), wind speed (W), and soil moisture (SM). On the right the mean of all model runs on the left is shown.

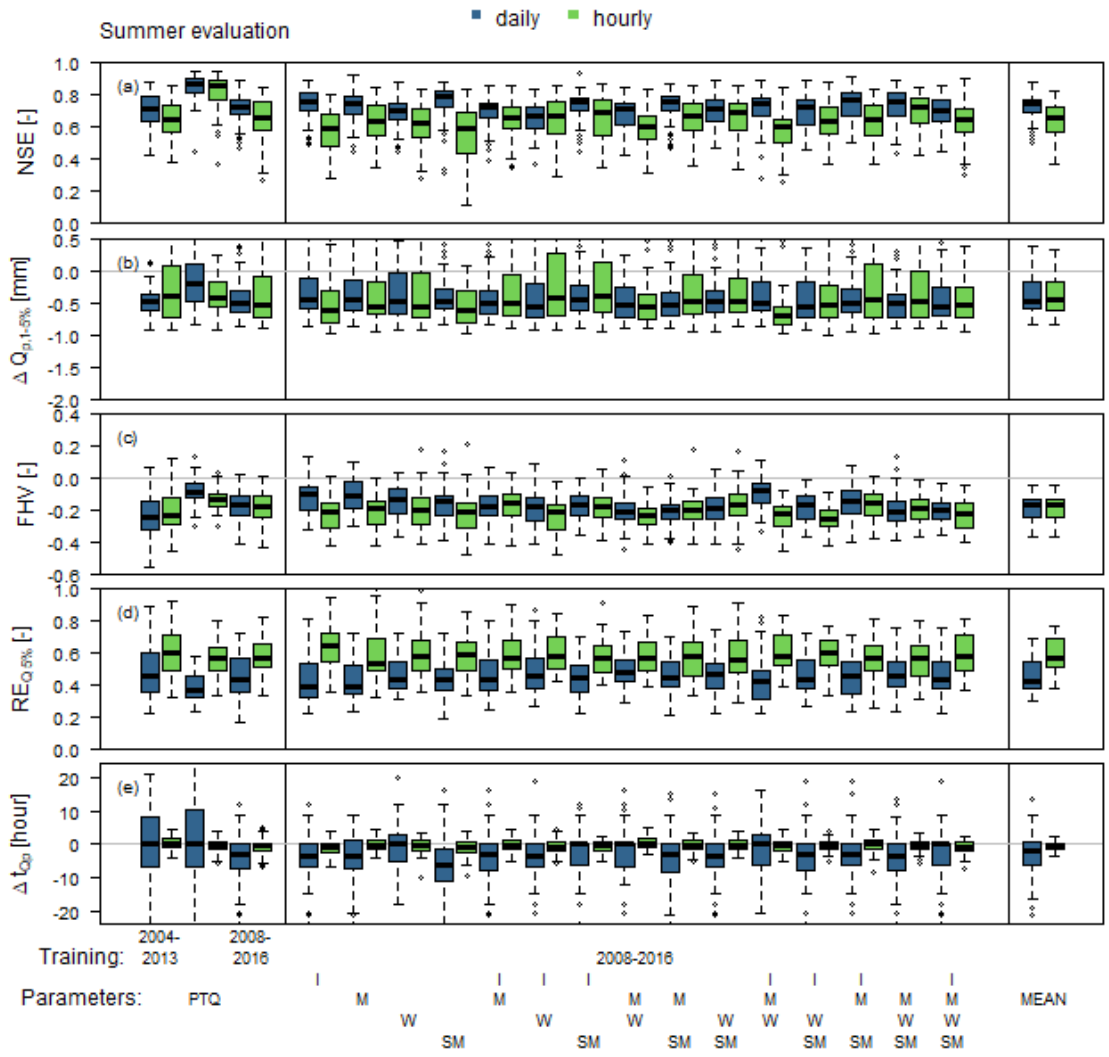

Figure 5.7.2: Summer (May – August) evaluation measures for all model runs. While the blue boxplots show the daily data, the green ones on their right show the results of the same model settings, but at hourly resolution. The parameter combinations all involve precipitation, air temperature and specific discharge (PTQ) for training. In addition, atmospheric parameters are added at the model runs shown in the middle column referring to atmospheric instability (I), atmospheric moisture (M), wind speed (W), and soil moisture (SM). On the right the mean of all model runs on the left is shown.

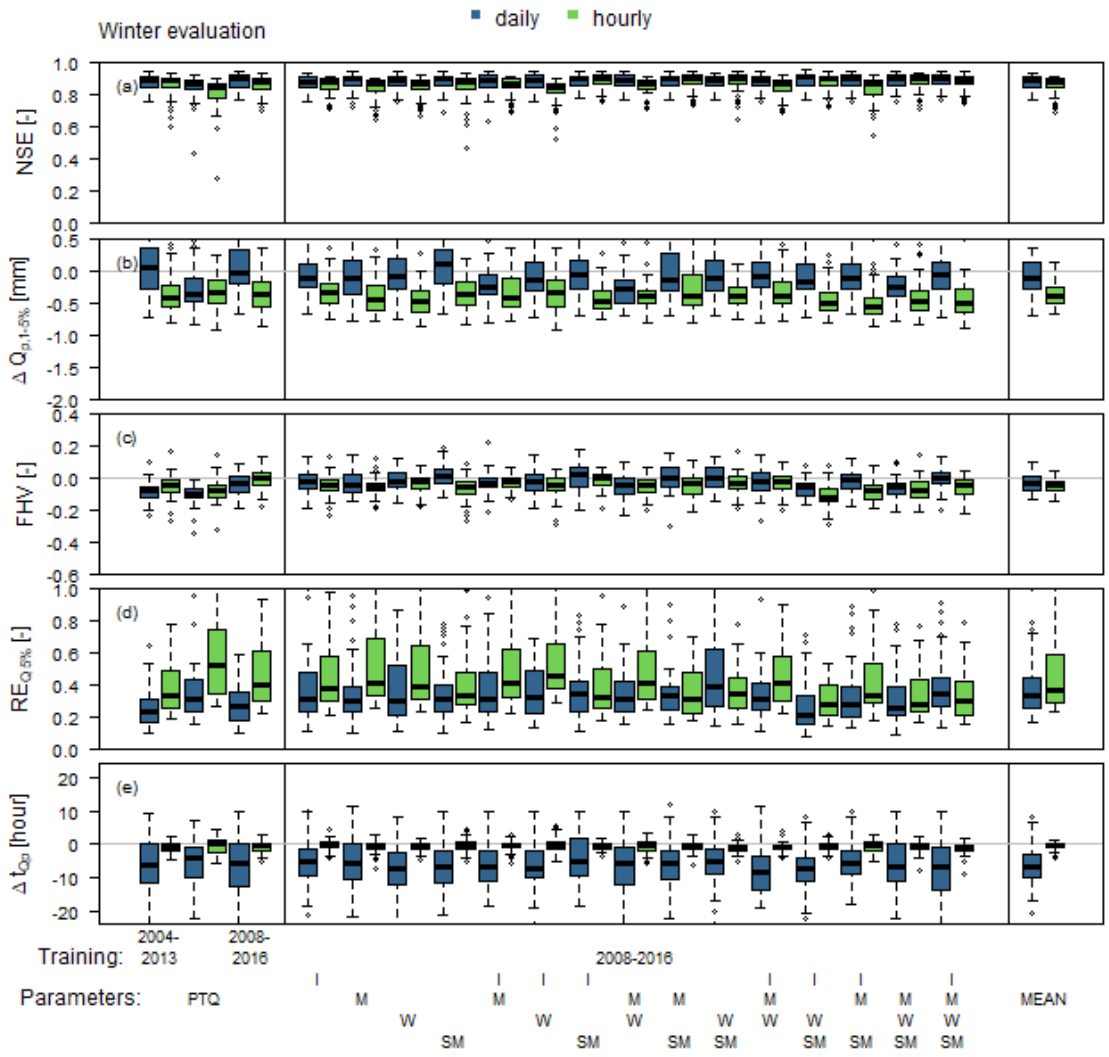

Figure 5.7.3: Winter (September – April) evaluation measures for all model runs. While the blue boxplots show the daily data, the green ones on their right show the results of the same model settings, but at hourly resolution. The parameter combinations all involve Precipitation, Temperature and specific discharge (PTQ) for training. In addition, atmospheric parameters are added at the model runs shown in the wide middle column referring to atmospheric instability (I), atmospheric moisture (M), wind speed (W), and soil moisture (SM). On the right the mean od all model runs on the left is shown.

6

General Discussion and Outlook

6.1 Intensification of the hydrological cycle

We investigated how the recent series of extreme precipitation and flash flood events in Luxembourg relate to a larger trend: namely, the intensification of the hydrological cycle driven by global climate change. While the concept of the intensification of hydrological extremes in terms of frequency, magnitude and volume (e.g. Donat et al., 2016; Wu et al., 2013; Yang et al., 2021) as well as an increasing event-to-event variability (Ficklin et al., 2022; Madakumbura et al., 2019) are widely accepted, there are diverse local variations of this alteration.

Precipitation generally varies considerably on an interannual basis and makes a confirmation of the conjectured intensification towards more frequent and more extreme events challenging. In our study, potentially weak signals of a changing climate could not be recognized due to the interannual variations and potential measurement biases. When analysing daily precipitation data for the frequency and magnitude of extreme precipitation events above 50 mm/d, we found increasing annual precipitation maxima during the summer, but the signal is not strong enough to consider it as a robust and significant trend. Assuming that the coarse station network misses some of the highest precipitation amounts and intensities of local thunderstorm cells, we also included highly resolved and comprehensive radar data (RADOLAN) in our analysis. The high frequency measurements only exist since 2002, which implies a 20-year timespan of data. Within our set of 20 years of precipitation radar data, we could not identify any trends in event frequency, intensity (5 min, 1 h) or duration. These findings might however be biased as the radar data - even though thoroughly corrected - still contains various sources of uncertainty, that underestimate precipitation especially during extreme events (Meischner, 2014; Strangeways, 2007; Winterrath et al., 2017; Kreklow et al., 2019; Pöschmann et al., 2021). A 20-year period is moreover rather short for climate analyses, that usually rely on at

least 30 years of data. This causes conclusions on potential trends to remain rather questionable. From the results of the 20 years of highly resolved data and of the almost 70 years of daily station data, we could not confirm our hypothesis about an increase in extreme precipitation events. Many global studies (e.g. Alexander, 2016; Donat et al., 2016; Kunkel and Frankson, 2015; Fischer and Knutti, 2016) suggest an increase in extreme precipitation event occurrence. Likewise, Müller and Pfister (2011) suggest an increase in extreme precipitation on a local scale for the Emscher-Lippe catchment in western Germany (1959-2009). These studies are however contradicted by analyses conducted by the DWD and GDV (2019) for Germany, not confirming any trends on the regional scale or on the global scale Koutsoyiannis (2020). Koutsoyiannis (2020) especially points to the fluctuations of precipitation demonstrating the weakness of simplified conclusions.

Isolating a potential increase in summer peak flow or even flash flood events is equally difficult. Long-term analyses based on daily discharge data at three stations in Luxembourg are not doing justice to summer peak flow, as peaks pass so quickly, that they are likely not measured to their full extent in the observations. Sub-hourly measurements have only become available since the mid-1990s for smaller catchments. For an analysis targeting localized flood events, often outside streams, streamflow data was considered to not be appropriate. Instead, an inventory of extreme discharge events (Supplement S3), that we defined as flash floods, was compiled. Achieving consistency in the database seems however an impossible task, when considering a recently increased awareness of flash floods, better documentation of recent events as well as an increased hazard due to expanding urban areas. Nevertheless, the suite of extreme events in 2016 and 2018, as well as in 2021 is a fact. Each event related to persisting atmospheric conditions that triggered extreme precipitation and flooding events over a larger region. The compiled events are however not sufficient to test for the conjectured trend. An expansion of the database beyond the regional limits following examples by Marchi et al. (2010) or Bertola et al. (2023) might help to mitigate its deficiencies, yet the temporal inconsistencies would most likely remain.

Understanding the flooding behaviour as an integration of atmospheric circulation patterns, we analysed their occurrence during high precipitation and flood events. Especially the zonal circulation type is correlated to annual precipitation amounts and major large scale floods. A phase of increased occurrences of the zonal circulation type during the late 1980s and 1990s can be clearly linked to a series of floods within that decade (Mansell, 1997; Pfister et al., 2000, 2004). Within recent years, the annual percentage of trough weather types and the related SWZ circulation form increased. During the trough constellation air masses meander in a U-shape, bringing warm and moist air from the Mediterranean area to central Europe on the Eastern flank of the system. Typical situations are the Vb-weather situation or the Spanish plumes that are often related to abundant rainfall (Gerstengarbe et al., 1999). These constellations are connected to some of the largest inundations of recent years, such as the Elbe-Flood in August 2002 (Fritzschner and Lux, 2002), the July 2021 flood in Western Europe (Mohr et al., 2023; Junghänel et al., 2021) or the flood in early June 2024 in Southern Germany and Austria (Bauer, 2024). The circulation patterns that sustained the flash floods in our database are manifold, reaching from

larger scale flood favouring conditions to very isolated thunderstorm events. While in many cases the floods in our database are not directly linked to the increased trough constellations, we conjecture, that they nonetheless increase soil moisture levels, supporting a potential flood. The circulation patterns themselves can hardly be isolated as "flash flood favouring" which is why we proceeded to the atmospheric characteristics related to the thunderstorms.

Investigating the atmospheric conditions during extreme precipitation and flash flood events, we found relevant changes in their occurrence. Especially high absolute atmospheric moisture contents have increased significantly in both, amount and frequency, during the summers between 1981 and 2020. This is in line with thermodynamics summarized in the Clausius-Clapeyron relationship, that project an increase of 6-7% of the global atmospheric water vapour per Kelvin degree air temperature increase (Allan et al., 2020). Additionally, we found positive trends assessing the instability of the atmosphere that we had analysed via the proxy parameter CAPE (convective available potential energy). While some of these increases in CAPE are offset by slightly increased convective inhibition (CIN) (Taszarek et al., 2021a), the overall increasingly favouring instability conditions prevailed. The wind components relevant for system motion and organization have remained constant over time. In combination, the most important components of extreme precipitation and flash flood favouring atmospheric conditions, namely abundant moisture and sufficient latent instability, have become more frequent reaching higher values which indicates potentially severer events. Thus, an intensification of the hydrological cycle can be attested with regard to the absolute atmospheric water contents.

The increasing occurrence of extreme precipitation and flash flood favouring atmospheric conditions was hypothesized to potentially lead to increasing precipitation intensities (Giorgi et al., 2019; Pfahl et al., 2017; Tandon et al., 2018; Trenberth et al., 2003) and subsequent flash flooding. This link could however not be traced down for extreme precipitation events during summer and appears to be too simple for the complex relationships and interactions within the water cycle. Changes could therefore be caused by changes in intra-annual temporal precipitation patterns and subsequently differing pre-event soil moisture conditions. Synoptic patterns lasting several days over one region and thereby amplifying the effect of the weather are often associated with atmospheric blocking situations. It is assumed that, as arctic regions warm faster than the tropics, the north-south air temperature gradient decreases and the compensating stream - the deviated jet steam - weakens and meanders more. These meanders, the Rossby-waves, constitute atmospheric blocking situations that block synoptic constellations over several days over the same region resulting in persistent weather conditions. While in the 1990s there were less blocking situations, they have increased to previous levels again since. An overall increasing trend can not be confirmed (Stendel et al., 2021; Lupo, 2021; Woollings et al., 2018). Other explanations might be of non-atmospheric origin and related to catchment-specific parameters that were not taken into account.

6.2 Data-based simulations under non-stationary conditions

Under the assumption of non-stationary hydrological systems, the simulation of potentially increasing occurrences of summer peak flow becomes more relevant. While conceptual models often struggle with the simulation of isolated peak flow events, we tested the information gain and performance of the application of data mining and machine learning algorithms, that have been applied successfully in the field of large-scale hydrology. Within recent years, CAMELS data sets (Catchment Attributes and Meteorology data for Large-sample Studies) were thriving, nourishing the idea of unified data sets characterizing many catchments. Following this trend, we compiled streamflow and precipitation time series from 56 physiographically described nested catchments over Luxembourg and complemented them with ERA5 reanalysis data. Based on the resulting CAMELS-LUX data set, we were able to set up a regional LSTM for Luxembourg, simulating many of the catchments for the first time. The benchmark model performance reaches reasonable Nash-Sutcliffe Efficiencies between values of 0.4 and 0.9. These model performances are comparable to the LSTM trained on the original CAMELS data set (NSE median around 0.7-0.8) (Kratzert et al., 2021), but are slightly lower than the LSTM trained on CAMELS-GB, that reached a median NSE value of 0.88 (Lees et al., 2021). Some of the weaker performing catchments in Luxembourg lose groundwater to deep percolation or through mining galleries, which prevents their water balance from closing. While one could expect the flexible model structure of LSTMs to compensate for inconsistencies in the water balance, the performance remains weaker, as also experienced in the benchmark model based on CAMELS-GB (Lees et al., 2021). Other than in Great-Britain, the runoff characteristics that are determined by the catchments' underlying geology type or varying topography seem to not cause systematic difficulties for the LSTM. In Great-Britain karstic areas performed worse as a group which is likely related to differing subsurface flow behaviour and connected to the non-closed water balance (Lees et al., 2021). Luxembourg does not have comparable geologic formations.

Major limitations of the LSTM for Luxembourg were identified for peak flow. While storage-controlled large-scale winter floods were well captured in both, flood height and volume, summer peak flows were not well captured and sometimes the flood signal was even completely missed. We attempted to improve the performance by increasing the temporal resolution of the LSTM model to an hourly time step. While the hourly values better reproduce the shape of the hydrograph during events, their performance with respect to the magnitude or flood volume is slightly poorer. This contradicts results from the US, where the peak timing of hourly values decreased, whereas the NSE remained unchanged (Gauch et al., 2021). Additionally, we added extreme precipitation relevant atmospheric proxy parameters and soil moisture to better characterize the atmospheric conditions sustaining the peak flow. While the atmospheric parameters and soil moisture were able to slightly improve the simulation for a few events, they do not lead systematically to better results. These findings are in contrast with experiments by Frame et al. (2021), who were able to

simulate peak flow events, even beyond the range of training data. Their study area was however spanning differing climate zones, which might train the model better. Limitations of the LSTM under dry and arid conditions are however known and have been described for intermittend streams in Southern Texas (Feng et al., 2020) and for less humid regions of South-East Great-Britain (Lees et al., 2021). Even though Luxembourg does not have an arid climate, summer conditions might be comparable to drier conditions. Kratzert et al. (2018, 2019b) suggested that the rainfall-runoff information for times with long low flow periods is difficult to learn.

Possible explanations as to why summer peak discharge was not well simulated in our case are manifold. While there should have been enough short storm flow peaks in the data set for the LSTM to learn the mechanism, we still seem to miss the right information as the model predictions fail. One major shortcoming is most likely the quality of the precipitation input data. Trying to compensate for possible deficiencies, we have provided several precipitation-related variables for the LSTM to choose from: the RADKLIM radar data, the minimum and maximum 5-minute precipitation intensities of the radar data as well as interpolated station data, and ERA5 reanalysis data. While weather radars form a comprehensive network, they still have deficiencies, especially during high rainfall intensities, when the backscatter is too high, so that areas further away become invisible (Kreklow et al., 2019; Pöschmann et al., 2021). Yet, some floods are purely missed, also for events where the precipitation data can be assumed to be of good quality, or even for events where the precipitation was artificially doubled.

Another shortcoming of the LSTMs is the failure to simulate values outside the range of training data. This artefact is introduced in the first step of an LSTM, when the training data is normalized. Even simulating values close to the minimum and maximum of the training data, did not happen in our approach. While the regional CAMELS-LUX data set only covers similar catchments within one climatic zone, an extension of the data set to other climate zones with a higher specific discharge might mitigate the effects of this artefact. These effects seem neglectable when using enormous global data sets (Nearing et al., 2024). In contrast, regional data sets do not contain enough extreme events in the training due to their rare nature (Bertola et al., 2023). Basically one would need events well beyond the value of the peak one wants to simulate. Several tests (not shown) about adding a catchment with artificially increased precipitation and discharge data in order to extend the general range did not bypass the saturated gradient problem.

While LSTMs perform usually very well during “normal” flow conditions and high flows of storage-controlled floods, they have evident deficiencies during summer peak flow. Based on our results, regional LSTMs do not seem suitable for simulations under non-stationary climate conditions and can therefore not be applied with the expectations to finally be able to capture unprecedented extreme events. While the static catchment attributes could be adjusted over time (as for example in Nearing et al., 2019), a changed climate beyond the training data cannot be simulated.

6.3 Outlook

For better assessments of variations in flood patterns, the flash flood database could be extended beyond the Greater Region of Luxembourg following examples of Marchi et al. (2010) and Bertola et al. (2023). A more comprehensive data set might allow to statistically group events and characterize them with regard to their pre-event and atmospheric conditions. This might reveal more about underlying conditions, that can usually not be described by the triggering precipitation amounts only. Moreover, unique and local parameters such as the precipitation intensity and duration, its distribution, the pre-event soil states as well as the region's topography could be considered and compared. Obtaining a temporally and spatially consistent database covering a time period long enough for climate studies appears to be a challenging task.

Hydrological advancements through the mining of data, open new possibilities with respect to identifying statistical patterns and relations within the global water cycle. A good scale for the application of data-based algorithms is still debated and can differ depending on the goal of simulations (Kratzert et al., 2024).

Exploring the potential of neural networks as modelling tools in hydrology has been ongoing for a few years. While LSTMs are a practical tool for general hydrological simulations across many catchments, they do have limitations during locally unprecedented flood events, which are implied under non-stationary conditions. For climate change impact studies or the forecasting of extreme events, LSTMs need to be applied on much wider scales, best globally, to be able to exploit their full potential. The setup of a huge global model is ambitiously pursued via the Flood Hub of Google (Nearing et al., 2024). However, it can be considered doubtful, whether such an idealized model would be able to simulate small, localized peak flow in meso- to micro-scale catchments. A further improvement in the quality of real-time precipitation data seems crucial in these attempts.

7 General Conclusion

My thesis has been structured around two major overarching research questions:

1. How can the extreme rainfall and runoff events that recently occurred in Luxembourg and the Greater Region be conceptualized in an era of proven global change?

2. Can we use large-scale data sets and machine learning algorithms to simulate extreme and flash flood events?

With respect to the first research question, we conjectured an intensifying hydrological cycle as the consequence of warmer air temperatures and approached the issue by testing in Chapter 3 the following hypothesis:

> "The recent accumulation of extreme precipitation and flash flood occurrences in central western Europe is triggered by a change in atmospheric circulation patterns."

This hypothesis could not be validated, as the summer extreme precipitation events and flash floods occur under widely differing synoptic settings. The various circulation types that have sustained a flash flood did not show any increasing trends that would confirm a relation with the recent accumulation of peak flow events. Among the recently increasing circulation patterns are many trough constellations, that usually trigger precipitation amounts above the average of all circulation patterns. While there is no direct connection between the trough circulation patterns and summer peak flows, they might nonetheless contribute to an increase in runoff reactions by elevating pre-event soil moisture levels. We could however confirm previous findings by Pfister et al. (2000, 2004), that the annual maximum streamflow is strongly correlated to zonal circulation patterns and precipitation during zonal conditions. This correlation is particularly relevant in winter, when the zonal circulation patterns bring widespread steady rain and subsequent storage-controlled, slowly developing

winter floods. Consequently, the general correlation between atmospheric circulation and discharge as well as the subsequent hypothesis were confirmed:

> "The strong correlation between atmospheric circulation types and winter discharge observed in the second half of the 20^{th} century for central western Europe still prevails today."

Directing the conjecture about an intensifying hydrological cycle into the detailed characterization of extreme precipitation and flash flood favouring atmospheric conditions via proxy parameters, we hypothesized in Chapter 4:

> "A change in atmospheric conditions has led to more frequent extreme precipitation events that have subsequently triggered flash flood events in central western Europe."

The first part of the hypothesis, i.e. a trend towards atmospheric conditions favouring extreme precipitation and flash flood events, was analysed based on three thunderstorm relevant groups of proxy parameters. (1) Abundant absolute atmospheric moisture contents (specific humidity, q, and total column water vapour, TCWV) have increased significantly between 1981 and 2020, whereas relative humidity (RH) decreased slightly. (2) Sufficient atmospheric instability (described by convective available potential energy, CAPE, and the K index) has increased during the study period. However, these gains in CAPE might be offset by likewise increases in convective inhibition (CIN) (Taszarek et al., 2021a). (3) Weak storm motion and organisation (characterized by wind speed, $WS_{10\,m-500\,hPa}$, low level shear, LLS, and deep layer shear, DLS) remained the same over time. In combination, the proxy parameters within the range of extreme precipitation and flash flood favouring atmospheric conditions have become higher and more frequent indicating potentially more and stronger events. We can therefore support this part of the hypothesis. The second part of the hypothesis, i.e. a trend towards more frequent extreme precipitation events, has to be rejected. Within the relatively short period of 20 years (2002-2021), neither the frequency nor the intensity of extreme precipitation events showed signals of an increasing trend. Instead, the interannual variation of precipitation events and their characteristics is very high. The third part of the hypothesis, i.e. an increasing trend in the occurrence of flash floods could not be tested due to inconsistencies in the very small data base.

Our most significant finding is the increase in absolute atmospheric moisture contents, that is in line with the physical understanding of thermodynamic processes described in the Clausius-Clapeyron relationship. However, the increased moisture contents can not be traced down directly to more frequent or more intense precipitation events. Consequently, the line of argument that more precipitation events trigger more flood occurrences cannot be maintained based on the data used in this thesis. The relationship between the three examined components of the water cycle is likely more complex than hypothesized and influenced by other, external factors. Yet, the increase in atmospheric moisture contents confirms the changes and intensification of the hydrological cycle under global change. The increase in atmospheric conditions favouring thunderstorms and extreme precipitation likely contributed to

the flash flood events in July 2016, June 2018 as well as during the large-scale flood events in July 2021. An increase in precipitation or flash flood events could however not be validated during the study period between 2002-2020.

The second part of my thesis focussed on the simulation of summer peak flow events using the compiled large-scale data set CAMELS-LUX and the Long Short-Term Memory (LSTM) machine learning algorithm. In a first step we tested in Chapter 2 and 5:

> "LSTMs are capable of simulating discharge across catchments with contrasted physiographic settings in and around Luxembourg."

The LSTM for Luxembourg achieved overall good efficiencies (NSE 0.4-0.9) throughout the physiographic range catchments, well capturing the hydrologic dynamics. A few catchments show a lower model performance, which is related to non-closing water balances or insufficient training data. While storage-controlled winter floods are simulated with good performances, extreme floods and summer peak flow events were not simulated sufficiently. Flood peaks were largely underestimated and in some cases the flood signals were completely missed. The hypothesis is however validated for the general model performance. In this way the quality of the CAMELS-LUX data set is equally validated to some extent.

Attempting to improve the simulation of summer peak discharge, we expanded the model's input parameter set and increased the temporal resolution of the model further hypothesizing in Chapter 5 that:

> "An hourly resolution improves the model performance during summer peak flow events."

> "Including atmospheric variables relevant for extreme precipitation improves the simulation of summer peak flow events."

Increasing the temporal resolution improved the shape of the hydrographs in many cases, that were not well represented in daily simulations due to the fast nature of the summer peak flow events. While the flood timing was improved in this way, the simulation of the magnitude of summer peak flow remained poor or slightly underestimated at best. Adding atmospheric data potentially sustaining extreme precipitation, slightly improved simulations in some cases, but did not in others. Various combinations of atmospheric parameters did not yield systematically better or worse results. Generally, the gain in skill through the additional input remained low and therefore the hypothesis is rejected.

Unfortunately, we have to conclude that the regional model is not the ideal tool for climate change impact studies. The LSTM, regionally set up for Luxembourg, is not able to extrapolate beyond the training data. For simulations like this, a supra-regional or continental approach would be crucial to include training data with a sufficient number of extreme events. Additionally, non-stationarity of catchments could be depicted using variable climate attributes, as suggested in Nearing et al. (2019). Nonetheless, LSTMs are a promising tool when simulating many catchments within a region at once with relatively little efforts, when the data is available. Data collection and especially the data quality are crucial for good simulations using the purely data-based LSTM models.

Bibliography

ACT - Administration du Cadastre et de la Topographie: LiDAR 2019 - Modèle numérique de terrain (MNT), URL https://data.public.lu/fr/datasets/lidar-2019-modele-numerique-de-terrain-mnt/, accessed: 2024-05-25, 2019.

Addor, N., Newman, A. J., Mizukami, N., and Clark, M. P.: The CAMELS data set: Catchment attributes and meteorology for large-sample studies, Hydrology and Earth System Sciences, 21, 5293–5313, doi:10.5194/hess-21-5293-2017, 2017.

AGE - Administration de la gestion de l'eau Luxembourg : 15-minute Discharge Data, accessed: 2022-04-01, 2022.

Alexander, L. V.: Global observed long-term changes in temperature and precipitation extremes: A review of progress and limitations in IPCC assessments and beyond, Weather and Climate Extremes, 11, 4–16, doi:10.1016/j.wace.2015.10.007, 2016.

Allan, R. P., Barlow, M., Byrne, M. P., Cherchi, A., Douville, H., Fowler, H. J., Gan, T. Y., Pendergrass, A. G., Rosenfeld, D., Swann, A. L., Wilcox, L. J., and Zolina, O.: Advances in understanding large-scale responses of the water cycle to climate change, doi:10.1111/nyas.14337, 2020.

Alvarez-Garreton, C., Mendoza, P. A., Boisier, J. P., Addor, N., Galleguillos, M., Zambrano-Bigiarini, M., Lara, A., Puelma, C., Cortes, G., Garreaud, R., McPhee, J., and Ayala, A.: The CAMELS-CL dataset: Catchment attributes and meteorology for large sample studies-Chile dataset, Hydrology and Earth System Sciences, 22, 5817–5846, doi:10.5194/hess-22-5817-2018, 2018.

Anderson, S. and Radić, V.: Evaluation and interpretation of convolutional long short-term memory networks for regional hydrological modelling, Hydrology and Earth System Sciences, 26, 795–825, doi:10.5194/hess-26-795-2022, 2022.

Andréassian, V., Delaigue, O., Perrin, C., Janet, B., and Addor, N.: CAMELS-FR: A large sample, hydroclimatic dataset for France, to support model testing and evaluation, in: EGU General Assembly 2021, pp. EGU21–13 349, online, 2021.

APC - Administration des ponts et chaussées: Carte géologique harmonisée, URL https://geocatalogue.geoportail.lu/geonetwork/srv/fre/catalog.search#/metadata/542a0caa-4b33-4019-8ce7-b8541b436106, accessed: 2024-05-25, 2022.

Ashley, S. T. and Ashley, W. S.: The storm morphology of deadly flooding events in the United States, International Journal of Climatology, 28, 493–503, doi:10.1002/joc.1554, 2008.

ASTA - Administation des services techniques de l'agriculture and Ministère de l'Agriculture de l'Alimentation et de la Viticulture: AgriMeteo: Precipitation data, URL https://www.agrimeteo.lu/Agrarmeteorologie/Wetterdaten/Niederschlag, accessed: 2024-06-23, 2024.

Bauer, N.: Dauerregenlage durch Vb-Tief, Tech. rep., DWD - German Weather Service, Vorhersage- und Beratungszentrale, URL https://www.dwd.de/DE/wetter/thema_des_tages/2024/5/30.html, accessed: 2024-06-18, 2024.

Baur, F., Hess, P., and Nagel, H.: Kalender der Großwetterlagen Europas 1881-1939, 1944.

Bertola, M., Viglione, A., Lun, D., Hall, J., and Blöschl, G.: Flood trends in Europe: Are changes in small and big floods different?, Hydrology and Earth System Sciences, 24, 1805–1822, doi:10.5194/hess-24-1805-2020, 2020.

Bertola, M., Viglione, A., Vorogushyn, S., Lun, D., Merz, B., and Blöschl, G.: Do small and large floods have the same drivers of change? A regional attribution analysis in Europe, Hydrology and Earth System Sciences, 25, 1347–1364, doi:10.5194/hess-25-1347-2021, 2021.

Bertola, M., Blöschl, G., Bohac, M., Borga, M., Castellarin, A., Chirico, G. B., Claps, P., Dallan, E., Danilovich, I., Ganora, D., Gorbachova, L., Ledvinka, O., Mavrova-Guirguinova, M., Montanari, A., Ovcharuk, V., Viglione, A., Volpi, E., Arheimer, B., Aronica, G. T., Bonacci, O., Čanjevac, I., Csik, A., Frolova, N., Gnandt, B., Gribovszki, Z., Gül, A., Günther, K., Guse, B., Hannaford, J., Harrigan, S., Kireeva, M., Kohnová, S., Komma, J., Kriauciuniene, J., Kronvang, B., Lawrence, D., Lüdtke, S., Mediero, L., Merz, B., Molnar, P., Murphy, C., Oskoruš, D., Osuch, M., Parajka, J., Pfister, L., Radevski, I., Sauquet, E., Schröter, K., Šraj, M., Szolgay, J., Turner, S., Valent, P., Veijalainen, N., Ward, P. J., Willems, P., and Zivkovic, N.: Megafloods in Europe can be anticipated from observations in hydrologically similar catchments, Nature Geoscience, 16, 982–988, doi:10.1038/s41561-023-01300-5, 2023.

Beven, K. J. and Kirkby, M. J.: A physically based, variable contributing area model of basin hydrology, Hydrological Sciences Bulletin, 24, 43–69, doi:10.1080/02626667909491834, 1979.

BGR - Bundesanstalt für Geowissenschaften und Rohstoffe: Geoportal der Bundesanstalt für Geowissenschaften und Rohstoffe, URL https://produktcenter.bgr.de/terraCatalog/DetailResult.do?fileIdentifier=0f2e1b5b-fc02-4491-a12b-2178473f5c84, accessed: 2024-05-25, 2019.

Bingenheimer, V.: Starkregen bringt Überschwemmungen im Zentrum und im Osten, Luxemburger Wort, URL https://www.wort.lu/luxemburg/starkreg

en-bringt-ueberschwemmungen-im-zentrum-und-im-osten/945939.html, accessed: 2024-07-06, 2018.

Bintz, J. and Muller, A.: On the representation of the Luxembourg Sandstone on the new general geological map of the Grand-Duchy (Sur la représentation du Grès de Luxembourg sur la nouvelle carte géologique générale du Grand-Duché), Arch. Inst. Grand-ducal Luxemb. Sect. Sci. Nat. Phys. Math., 31, 241–258, 1965.

Bissolli, P. and Dittmann, E.: The objective weather type classification of the German weather service and its possibilities of application to environmental and meteorological investigations, Meteorologische Zeitschrift, 10, 253–260, doi:10.1127/0941-2948/2001/0010-0253, 2001.

BMI - Federal Ministry of the Interior and Community and Federal Ministry of Finance: Bericht zur Hochwasserkatastrophe 2021: Katastrophenhilfe, Wiederaufbau und Evaluierungsprozesse, URL https://www.bmi.bund.de/SharedDocs/downloads/DE/veroeffentlichungen/2022/abschlussbericht-hochwasserkatastrophe.pdf, accessed: 2024-06-09, 2022.

Bouwer, L. M., Vermaat, J. E., and Aerts, J. C.: Regional sensitivities of mean and peak river discharge to climate variability in Europe, Journal of Geophysical Research Atmospheres, 113, 1–11, doi:10.1029/2008JD010301, 2008.

Brauer, C. C., Teuling, A. J., Overeem, A., van der Velde, Y., Hazenberg, P., Warmerdam, P. M. M., and Uijlenhoet, R.: Anatomy of extraordinary rainfall and flash flood in a Dutch lowland catchment, Hydrology and Earth System Sciences, 15, 1991–2005, doi:10.5194/hess-15-1991-2011, 2011.

BRGM - Géosciences pour uns Terre durable: Téléchargement des cartes géologiques départementales à 1/50 000 (Bd Charm-50), URL https://infoterre.brgm.fr/formulaire/telechargement-cartes-geologiques-departementales-150-000-bd-charm-50, accessed: 2024-05-25, 2020.

Bronstert, A., Agarwal, A., Boessenkool, B., Fischer, M., Heistermann, M., and Köhn-Reich, L.: Die Sturzflut von Braunsbach am 29. Mai 2016 – Entstehung, Ablauf und Schäden eines „Jahrhundertereignisses“. Teil 1: Meteorologische und hydrologische Analyse, Hydrologie und Wasserbewirtschaftung, 61, 150–162, doi:10.5675/HyWa, 2017.

Bronstert, A., Agarwal, A., Boessenkool, B., Crisologo, I., Fischer, M., Heistermann, M., Köhn-Reich, L., López-Tarazón, J. A., Moran, T., Ozturk, U., Reinhardt-Imjela, C., and Wendi, D.: Forensic hydro-meteorological analysis of an extreme flash flood: The 2016-05-29 event in Braunsbach, SW Germany, Science of the Total Environment, 630, 977–991, doi:10.1016/j.scitotenv.2018.02.241, 2018.

Brooks, H. E.: Proximity soundings for severe convection for Europe and the United States from reanalysis data, Atmospheric Research, 93, 546–553, doi:10.1016/j.atmosres.2008.10.005, 2009.

Brooks, H. E.: Severe thunderstorms and climate change, Atmospheric Research, 123, 129–138, doi:10.1016/j.atmosres.2012.04.002, 2013.

Bucała-Hrabia, A., Kijowska-Strugała, M., Bryndal, T., Cebulski, J., Kiszka, K., and Kroczak, R.: An integrated approach for investigating geomorphic changes due to flash flooding in two small stream channels (Western Polish Carpathians), Journal of Hydrology: Regional Studies, 31, 100 731, doi:10.1016/j.ejrh.2020.100731, 2020.

CCR - Caisse Centrale de Réassurance: Événements - inondations, Tech. rep., Caisse Centrale de Réassurance (CCR), Paris, URL https://catastrophes-naturelles.ccr.fr/les-evenements, accessed: 2021-09-24, 2021.

Chagas, V. B., Chaffe, P. L. B., Addor, N., Fan, F. M., Fleischmann, A. S., Paiva, R. C. D., and Siqueira, V. A.: CAMELS-BR: Hydrometeorological time series and landscape attributes for 897 catchments in Brazil, Earth System Science Data, 12, 2075–2096, doi:10.5194/essd-12-2075-2020, 2020.

Champion, A. J., Allan, R. P., and Lavers, D. A.: Atmospheric rivers do not explain UK summer extreme rainfall, Journal of Geophysical Research, 120, 6731–6741, doi:10.1002/2014JD022863, 2015.

Chen, J., Dai, A., Zhang, Y., and Rasmussen, K. L.: Changes in convective available potential energy and convective inhibition under global warming, Journal of Climate, 33, 2025–2050, doi:10.1175/JCLI-D-19-0461.1, 2020.

Clerc-Schwarzenbach, F. M., Selleri, G., Neri, M., Toth, E., van Meerveld, I., and Seibert, J.: HESS Opinions: A few camels or a whole caravan?, EGUsphere [preprint], pp. 1–29, doi:10.5194/egusphere-2024-864, 2024.

Coxon, G., Addor, N., Bloomfield, J. P., Freer, J., Fry, M., Hannaford, J., Howden, N. J., Lane, R., Lewis, M., Robinson, E. L., Wagener, T., and Woods, R.: CAMELS-GB: hydrometeorological time series and landscape attributes for 671 catchments in Great Britain, Earth System Science Data, 12, 2459–2483, doi:10.5194/essd-12-2459-2020, 2020.

Crisis Centrum Belgium: Dossier: Overstromingen Juli 2021, URL https://crisiscentrum.be/nl/overstromingen-juli-2021, accessed: 2024-06-09, 2021.

Daniels, E., Lenderink, G., Hutjes, R., and Holtslag, A.: Relative impacts of land use and climate change on summer precipitation in the Netherlands, Hydrology and Earth System Sciences, 20, 4129–4142, doi:10.5194/hess-20-4129-2016, 2016.

Detring, C., Müller, A., Schielicke, L., Névir, P., and Rust, H. W.: Occurrence and transition probabilities of omega and high-over-low blocking in the Euro-Atlantic region, Weather and Climate Dynamics, 2, 927–952, doi:10.5194/wcd-2-927-2021, 2021.

Devi, G. K., Ganasri, B. P., and Dwarakish, G. S.: A Review on Hydrological Models, Aquatic Procedia: International Conference on Water Resources, Coastal and Ocean Engineering (ICWRCOE 2015), 4, 1001–1007, doi:10.1016/j.aqpro.2015.02.126, 2015.

Diffenbaugh, N. S., Scherer, M., and Trapp, R. J.: Robust increases in severe thunderstorm environments in response to greenhouse forcing, Proceedings of the National Academy of Sciences of the United States of America, 110, 16 361–16 366, doi:10.1073/pnas.1307758110, 2013.

Donat, M. G., Lowry, A. L., Alexander, L. V., O'Gorman, P. A., and Maher, N.: More extreme precipitation in the world's dry and wet regions, Nature Climate Change, 6, 508–513, doi:10.1038/nclimate2941, 2016.

Doswell, C. A. and Schultz, D. M.: On the use of indices and parameters in forecasting severe storms, E-Journal of Severe Storms Meteorology, 1, 1–22, doi:10.55599/ejssm.v1i3.4, 2006.

Doswell, C. A., Brooks, H. E., and Maddox, R. A.: Flash flood forecasting: An ingredients-based methodology, Weather and Forecasting, 11, 560–581, doi:10.1175/1520-0434(1996)011<0560:FFFAIB>2.0.CO;2, 1996.

Dougherty, E. and Rasmussen, K. L.: Climatology of flood-producing storms and their associated rainfall characteristics in the United States, Monthly Weather Review, 147, 3861–3877, doi:10.1175/MWR-D-19-0020.1, 2019.

DWD - German Weather Sercive: Warnkriterien - Starkregen, URL https://www.dwd.de/DE/wetter/warnungen_aktuell/kriterien/warnkriterien.html, accessed: 2024-06-09, 2024.

DWD - German Weather Service: Wetterlexikon - Starkregen, URL https://www.dwd.de/DE/service/lexikon/begriffe/S/Starkregen.html, accessed: 2021-05-20, 2021.

DWD - German Weather Service: Großwetterlagenklassifikation sowie die objektive Wetterlagenzuordnung, URL https://www.dwd.de/DE/leistungen/grosswetterlage/grosswetterlage.html, accessed: 2024-06-09, 2024a.

DWD - German Weather Service: Open data: 10-minute precipitation data, URL https://opendata.dwd.de/climate_environment/CDC/observations_germany/climate/10_minutes/precipitation/historical/, accessed: 2024-06-23, 2024b.

DWD - German Weather Service and GDV - Gesamtverband der Deutschen Versicherungswirtschaft e. V.: Forschungsprojekt „Starkregen" - Fachbericht: Eine Zusammenfassung der wichtigsten Ergebnisse des Projekts zum Zusammenhang zwischen Starkregen und versicherten Schäden untersucht von GDV und DWD, Tech. rep., URL https://www.gdv.de/resource/blob/63746/ac53789625df198043ea0779329b42d9/fachbericht-data.pdf, accessed: 2023-12-31, 2019.

Eden, J. M., Kew, S. F., Bellprat, O., Lenderink, G., Manola, I., Omrani, H., and van Oldenborgh, G. J.: Extreme precipitation in the Netherlands: An event attribution case study, Weather and Climate Extremes, 21, 90–101, doi:10.1016/j.wace.2018.07.003, 2018.

EEA - European Environment Agency: CORINE Land Cover 2018 (vector/raster 100 m), Europe, 6-yearly, Version 2020-2021, doi:10.2909/960998c1-1870-4e82-8051-6485205ebbac, URL https://land.copernicus.eu/en/products/corine-land-cover/clc2018, accessed: 2024-05-25, 2018.

Ellenrieder, M. and Rauch, E.: Ellenrieder, T. and Rauch, E.: Flood risks on the rise - Greater loss prevention is needed, URL https://www.munichre.com/en/risks/natural-disasters/floods.html, accessed: 2024-06-09, 2024.

Espinoza, E. A., Loritz, R., Álvarez Chaves, M., Bäuerle, N., and Ehret, U.: To Bucket or not to Bucket? Analyzing the performance and interpretability of hybrid hydrological models with dynamic parameterization, EGUsphere [preprint], doi:10.5194/egusphere-2023-1980, 2023.

Euser, T., Winsemius, H. C., Hrachowitz, M., Fenicia, F., Uhlenbrook, S., and Savenije, H. H.: A framework to assess the realism of model structures using hydrological signatures, Hydrology and Earth System Sciences, 17, 1893–1912, doi:10.5194/hess-17-1893-2013, 2013.

Feng, D., Fang, K., and Shen, C.: Enhancing Streamflow Forecast and Extracting Insights Using Long-Short Term Memory Networks With Data Integration at Continental Scales, Water Resources Reseach, 56, doi:10.1029/2019WR026793, 2020.

Ficklin, D. L., Null, S. E., Abatzoglou, J. T., Novick, K. A., and Myers, D. T.: Hydrological Intensification Will Increase the Complexity of Water Resource Management, Earth's Future, 10, doi:10.1029/2021EF002487, 2022.

Fischer, E. M. and Knutti, R.: Observed heavy precipitation increase confirms theory and early models, Nature Climate Change, 6, 986–991, doi:10.1038/nclimate3110, 2016.

Fleig, A. K., Tallaksen, L. M., Hisdal, H., and Hannah, D. M.: Regional hydrological drought in north-western Europe: Linking a new Regional Drought Area Index with weather types, Hydrological Processes, 25, 1163–1179, doi:10.1002/hyp.7644, 2011.

Fowler, K. J., Acharya, S. C., Addor, N., Chou, C., and Peel, M. C.: CAMELS-AUS: Hydrometeorological time series and landscape attributes for 222 catchments in Australia, Earth System Science Data, 13, 3847–3867, doi:10.5194/essd-13-3847-2021, 2021.

Frame, J., Kratzert, F., Klotz, D., Gauch, M., Shelev, G., Gilon, O., Qualls, L., Gupta, H., and Nearing, G.: Deep learning rainfall-runoff predictions of extreme events, Hydrology and Earth System Sciences Discussions, pp. 1–20, 2021.

Franceinfo: 3 grand est - Inondations, URL https://france3-regions.francetvinfo.fr/meteo/inondations?r=grand-est, accessed: 2022-11-18, 2021.

Fritzschner, U. and Lux, G.: Starkniederschläge in Sachsen im August 2002 - Eine meteorologisch-synoptische und klimatologische Beschreibung des Augusthochwassers im Elbegebiet, URL https://www.dwd.de/DE/service/lexikon/begriffe/V/Vb-Wetterlage_pdf.pdf, accessed: 2024-06-18, 2002.

Funk, T. W.: Forecasting Techniques Utilized by the Forecast Branch of the National Meteorological Center During a Major Convective Rainfall Event, Weather and Forecasting, 6, 548–564, doi:10.1175/1520-0434(1991)006<0548:FTUBTF>2.0.CO;2, 1991.

Gauch, M., Kratzert, F., Klotz, D., Nearing, G., Lin, J., and Hochreiter, S.: Rainfall-runoff prediction at multiple timescales with a single Long Short-Term Memory network, Hydrology and Earth System Sciences, 25, 2045–2062, doi:10.5194/hess-25-2045-2021, 2021.

Gaume, E., Bain, V., Bernardara, P., Newinger, O., Barbuc, M., Bateman, A., Blöschl, G., Borga, M., Dumitrescu, A., Daliakopoulos, I., Garcia, J., Irimescu, A., Kohnova, S., Koutroulis, A., Marchi, L., Matreata, S., Medina, V., Preciso, E., Sempere-torres, D., Stancalie, G., Szolgay, J., Tsanis, I., Velasco, D., and Viglione, A.: A compilation of data on European flash floods, Journal of Hydrology, 367, 70–78, doi:10.1016/j.jhydrol.2008.12.028, 2009.

George, J. J.: Weather forecasting for aeronautics, Academic Press, New York City, ISBN: 9781483233208, URL https://www.sciencedirect.com/book/9781483233208/weather-forecasting-for-aeronautics, accessed: 2023-12-31, 1960.

Gerstengarbe, F.-W., Werner, P., and Rüge, U.: Katalog der Großwetterlagen Europas (1881-1998) nach Paul Hess und Helmuth Brezowsky, Tech. rep., Potsdam-Institut für Klimafolgenforschung, Potsdam, Offenbach a. M., URL https://publications.pik-potsdam.de/pubman/item/item_16833_1/component/file_16834/4864.pdf, accessed: 2024-07-06, 1999.

Giorgi, F., Raffaele, F., and Coppola, E.: The response of precipitation characteristics to global warming from climate projections, Earth System Dynamics, 10, 73–89, doi:10.5194/esd-10-73-2019, 2019.

Gochis, D., Schumacher, R., Friedrich, K., Doesken, N., Kelsch, M., Sun, J., Ikeda, K., Lindsey, D., Wood, A., Dolan, B., Matrosov, S., Newman, A., Mahoney, K., Rutledge, S., Johnson, R., Kucera, P., Kennedy, P., Sempere-Torres, D., Steiner, M., Roberts, R., Wilson, J., Yu, W., Chandrasekar, V., Rasmussen, R., Anderson, A., and Brown, B.: The great Colorado flood of September 2013, Bulletin of the American Meteorological Society, 96, 1461–1487, doi:10.1175/BAMS-D-13-00241.1, 2015.

Göppert, H.: Auswertung von abgelaufenen Starkregenereignissen über Radarmessungen, Wasserwirtschaft, 108, 44–50, doi:10.1007/s35147-018-0223-8, 2018.

Gourdol, L., Stewart, M. K., Morgenstern, U., and Pfister, L.: Short high-accuracy tritium data time series for assessing groundwater mean transit times in the vadose and saturated zones of the Luxembourg Sandstone aquifer, Hydrology and Earth System Sciences, doi:10.5194/hess-2023-152, 2023.

Gravelius, H.: Flusskunde 1, vol. 1, Göschen, potamology edn., 1914.

Groenemeijer, P. H. and van Delden, A.: Sounding-derived parameters associated with large hail and tornadoes in the Netherlands, Atmospheric Research, 83, 473–487, doi:10.1016/j.atmosres.2005.08.006, 2007.

Hall, A. J.: Flash Flood Forecasting, World Meteorological Organization (WMO) - Operational Hydrology Report, pp. 1–38, doi:92-63-10577-4, 1981.

Hao, Z., Singh, V. P., and Hao, F.: Compound extremes in hydroclimatology: A review, Water (Switzerland), 10, doi:10.3390/w10060718, 2018.

Hellebrand, H., Hoffmann, L., Juilleret, J., and Pfister, L.: Hydrology and Earth System Sciences Assessing winter storm flow generation by means of permeability of the lithology and dominating runoff production processes, Hydrol. Earth Syst. Sci, 11, 1673–1682, doi:10.5194/hess-11-1673-2007, 2007.

Hengl, T., Parente, L. L., Krizan, J., and Bonannella, C.: Continental Europe Digital Terrain Model at 30 m resolution based on GEDI, ICESat-2, AW3D, GLO-30, EUDEM, MERIT DEM and Background Layers. Distributed by OpenTopography, doi:10.5281/zenodo.4724549, accessed: 2024-05-25, 2022.

Hersbach, H., Bell, B., Berrisford, P., Biavati, G., Horányi, A., Muñoz Sabater, J., Nicolas, J., Peubey, C., Radu, R., Rozum, I., Schepers, D., Simmons, A., Soci, C., Dee, D., and Thépaut, J.-N.: ERA5 hourly data on single levels from 1979 to present, Copernicus Climate Change Service (C3S) Climate Data Store (CDS), doi:10.24381/cds.adbb2d47, 2018a.

Hersbach, H., Bell, B., Berrisford, P., Biavati, G., Horányi, A., Muñoz Sabater, J., Nicolas, J., Peubey, C., Radu, R., Rozum, I., Schepers, D., Simmons, A., Soci, C., Dee, D., and Thépaut, J.-N.: ERA5 hourly data on pressure levels from 1979 to present, Copernicus Climate Change Service (C3S) Climate Data Store (CDS), doi:10.24381/cds.bd0915c6, 2018b.

Hersbach, H., Bell, B., Berrisford, P., Hirahara, S., Horányi, A., Muñoz-Sabater, J., Nicolas, J., Peubey, C., Radu, R., Schepers, D., Simmons, A., Soci, C., Abdalla, S., Abellan, X., Balsamo, G., Bechtold, P., Biavati, G., Bidlot, J., Bonavita, M., De Chiara, G., Dahlgren, P., Dee, D., Diamantakis, M., Dragani, R., Flemming, J., Forbes, R., Fuentes, M., Geer, A., Haimberger, L., Healy, S., Hogan, R. J., Hólm, E., Janisková, M., Keeley, S., Laloyaux, P., Lopez, P., Lupu, C., Radnoti, G., de Rosnay, P., Rozum, I., Vamborg, F., Villaume, S., and Thépaut, J. N.: The

ERA5 global reanalysis, Quarterly Journal of the Royal Meteorological Society, 146, 1999–2049, doi:10.1002/qj.3803, 2020.

Hersbach, H., Bell, B., Berrisford, P., Biavati, G., Horányi, A., Muñoz Sabater, J., Nicolas, J., Peubey, C., Radu, R., Rozum, I., Schepers, D., Simmons, A., Soci, C., Dee, D., and Thépaut, J.-N.: ERA5 hourly data on pressure levels from 1940 to present, Copernicus Climate Change Service (C3S) Climate Data Store (CDS), doi:10.24381/cds.bd0915c6, 2023a.

Hersbach, H., Bell, B., Berrisford, P., Biavati, G., Horányi, A., Sabater, J. M., Nicolas, J., Peubey, C., Radu, R., Rozum, I., Schepers, D., Simmons, A., Soci, C., Dee, D., and Thépaut, J.-N.: ERA5 hourly data on single levels from 1940 to present, Copernicus Climate Change Service (C3S) Climate Data Store (CDS), doi:10.24381/cds.adbb2d47, 2023b.

Hess, P. and Brezowsky, H.: Katalog der Großwetterlagen Europas: (1881-1976), Berichte des Deutschen Wetterdienstes, German Weather Service, Berlin, 1952.

Hess, P. and Brezowsky, H.: Katalog der Großwetterlagen Europas: (1881-1976), Berichte des Deutschen Wetterdienstes, German Weather Service, Berlin, 2 edn., 1969.

Hess, P. and Brezowsky, H.: Katalog der Großwetterlagen Europas: (1881-1976), Berichte des Deutschen Wetterdienstes, German Weather Service, Berlin, 3 edn., 1977.

Hissler, C., Martínez-Carreras, N., Barnich, F., Gourdol, L., Iffly, J. F., Juilleret, J., Klaus, J., and Pfister, L.: The Weierbach experimental catchment in Luxembourg: A decade of critical zone monitoring in a temperate forest - from hydrological investigations to ecohydrological perspectives, Hydrological Processes, 35, doi:10.1002/hyp.14140, 2021.

Hobson, R. D.: Surface roughness in topography: quantitative approach, in: Spatial analysis in geomorphology, edited by Chorley, R. J., pp. 221–245, Harper and Row, New York, 1972.

Hochreiter, S. and Schmidhuber, J.: Long Short-Term Memory, Neural Computation, 9, 1735–1780, doi:10.1162/neco.1997.9.8.1735, 1997.

Huth, R., Beck, C., Philipp, A., Demuzere, M., Ustrnul, Z., Cahynová, M., Kyselý, J., and Tveito, O. E.: Classifications of atmospheric circulation patterns: Recent advances and applications, Annals of the New York Academy of Sciences, 1146, 105–152, doi:10.1196/annals.1446.019, 2008.

Höge, M., Kauzlaric, M., Siber, R., Schönenberger, U., Horton, P., Schwanbeck, J., Floriancic, M. G., Viviroli, D., Wilhelm, S., Sikorska-Senoner, A. E., Addor, N., Brunner, M., Pool, S., Zappa, M., and Fenicia, F.: CAMELS-CH: hydro-meteorological time series and landscape attributes for 331 catchments in hydrologic Switzerland, Earth System Science Data, 15, 5755–5784, doi:10.5194/essd-15-5755-2023, 2023.

Iffly, J. F., Bastian, C., Douinot, A., Göhlhausen, D., Hostache, R., Matgen, P., Minette, F., Patz, N., Trebs, I., and Pfister, L.: Mechanistic and statistical analysis of the summer 2016 flash-flood event in Luxembourg: lessons learned and new perspectives in monitoring, in: EGU General Assembly 2018, vol. 20, pp. EGU2018–12 777, 2018.

IPCC - Intergovernmental Panel on Climate Change, H.-O. P., Roberts, D., Tignor, M., Poloczanska, E., Mintenbeck, K., Alegría, A., Craig, M., Langsdorf, S., Löschke, S., Möller, V., Okem, A., and Rama, B.: Summary for Policymakers [Pörtner, H.-O., Roberts, D.C., Poloczanska, E.S., Mintenbeck, K., Tignor, M., Alegría, A.,Craig, M., Langsdorf, S. Löschke, S., Möller, V., Okem, A. (eds.)], pp. 3–33, Cambridge University Press, doi:10.1017/9781009325844.001.

IT-NRW - Information und Technik Nordrhein-Westfalen: Digitales Geländemodell - Gitterweite 1 m - Paketierung: Einzelkacheln, URL https://www.opengeodata.nrw.de/produkte/geobasis/hm/dgm1_xyz/dgm1_xyz/, accessed: 2024-05-25, 2021.

James, P. M.: An objective classification method for Hess and Brezowsky Grosswetterlagen over Europe, Theoretical and Applied Climatology, 88, 17–42, doi:10.1007/s00704-006-0239-3, 2007.

Jhong, Y. D., Chen, C. S., Jhong, B. C., Tsai, C. H., and Yang, S. Y.: Optimization of LSTM Parameters for Flash Flood Forecasting Using Genetic Algorithm, Water Resources Management, 38, 1141–1164, doi:10.1007/s11269-023-03713-8, 2024.

Johst, M., Gerlach, N., and Demuth, N.: Starkregen und Hochwasser im Mai/Juni 2018, Tech. rep., Landesamt für Umwelt Rheinland-Pfalz, Mainz, Germany, URL http://www.hochwasser-rlp.de/publikationen/bericht_juni_2018.pdf, accessed: 2022-11-18, 2018.

Junghänel, T., Kaspar, F., Lengfeld, K., and Rauthe, M.: Hydro-klimatologische Einordnung der Stark-und Dauerniederschläge in Teilen Deutschlands im Zusammenhang mit dem Tiefdruckgebiet "Bernd" vom 12. bis 19. Juli 2021, Tech. rep., DWD - German Weather Service, URL https://www.dwd.de/DE/klimaumwelt/aktuelle_meldungen/240117/Download_Stark_Dauerniederschlaege_2023-2024.pdf;jsessionid=EC08C1EF384F9EA1C7D7ED9B642C6286.live21074?__blob=publicationFile&v=5, accessed: 2024-07-06, 2021.

Junker, N. W., Schneider, R. S., and Fauver, S. L.: A study of heavy rainfall events during the great midwest flood of 1993, Weather and Forecasting, 14, 701–712, doi:10.1175/1520-0434(1999)014<0701:ASOHRE>2.0.CO;2, 1999.

Klingler, C., Schulz, K., and Herrnegger, M.: LamaH-CE: LArge-SaMple DAta for Hydrology and Environmental Sciences for Central Europe, Earth System Science Data, 13, 4529–4565, doi:10.5194/essd-13-4529-2021, 2021.

Kottek, M., Grieser, J., Beck, C., Rudolf, B., and Rubel, F.: World map of the Köppen-Geiger climate classification updated, Meteorologische Zeitschrift, 15, 259–263, doi:10.1127/0941-2948/2006/0130, 2006.

Koutsoyiannis, D.: Revisiting the global hydrological cycle: Is it intensifying?, Hydrology and Earth System Sciences, 24, 3899–3932, doi:10.5194/hess-24-3899-2020, 2020.

Kratzert, F., Klotz, D., Brenner, C., Schulz, K., and Herrnegger, M.: Rainfall – runoff modelling using Long Short-Term Memory (LSTM) networks, Hydrology and Earth System Sciences, pp. 6005–6022, doi:10.5194/hess-22-6005-2018, 2018.

Kratzert, F., Herrnegger, M., Klotz, D., Hochreiter, S., and Klambauer, G.: NeuralHydrology – Interpreting LSTMs in Hydrology. In: Samek, W., Montavon, G., Vedaldi, A., Hansen, L., Müller, KR. (eds) Explainable AI: Interpreting, Explaining and Visualizing Deep Learning. Lecture Notes in Computer Science, vol. vol 11700. Springer, Springer, Cham, doi:10.1007/978-3-030-28954-6_19, 2019a.

Kratzert, F., Klotz, D., Herrnegger, M., Sampson, A. K., Hochreiter, S., and Nearing, G. S.: Toward Improved Predictions in Ungauged Basins: Exploiting the Power of Machine Learning, Water Resources Research, 55, 11 344–11 354, doi:10.1029/2019WR026065, 2019b.

Kratzert, F., Klotz, D., Shalev, G., Klambauer, G., Hochreiter, S., and Nearing, G.: Towards learning universal, regional, and local hydrological behaviors via machine learning applied to large-sample datasets, Hydrology and Earth System Sciences, 23, 5089–5110, doi:10.5194/hess-23-5089-2019, 2019c.

Kratzert, F., Klotz, D., Hochreiter, S., and Nearing, G. S.: A note on leveraging synergy in multiple meteorological data sets with deep learning for rainfall-runoff modeling, Hydrology and Earth System Sciences, 25, 2685–2703, doi:10.5194/hess-25-2685-2021, 2021.

Kratzert, F., Nearing, G., Addor, N., Erickson, T., Gauch, M., Gilon, O., Gudmundsson, L., Hassidim, A., Klotz, D., Nevo, S., Shalev, G., and Matias, Y.: Caravan - A global community dataset for large-sample hydrology, Scientific Data, 10, doi:10.1038/s41597-023-01975-w, 2023.

Kratzert, F., Gauch, M., Klotz, D., and Nearing, G.: HESS Opinions: Never train an LSTM on a single basin, Hydrology and Earth System Sciences Discussion [preprint], 2024, 1–19, doi:10.5194/hess-2023-275, 2024.

Kreienkamp, F., Philip, S. Y., Tradowsky, J. S., Kew, S. F., Lorenz, P., Arrighi, J., Belleflamme, A., Bettmann, T., Caluwaerts, S., Chan, S. C., Ciavarella, A., De Cruz, L., de Vries, H., Demuth, N., Ferrone, A., Fischer, E. M., Fowler, H. J., Goergen, K., Heinrich, D., Henrichs, Y., Lenderink, G., Kaspar, F., Nilson, E., Otto, F. E. L., Ragone, F., Seneviratne, S. I., Singh, R. K., Skålevåg, A., Termonia, P., Thalheimer, L., van Aalst, M., Van den Bergh, J., Van de Vyver, H., Vannitsem, S., van Oldenborgh, G. J., Van Schaeybroeck, B., Vautard, R., Vonk, D., and

Wanders, N.: Rapid attribution of heavy rainfall events leading to the severe flooding in Western Europe during July 2021, Royal Netherlands Meteorological Institute (KNMI), 13, 18, URL https://www.worldweatherattribution.org/wp-content/uploads/Scientific-report-Western-Europe-floods-2021-attribution.pdf, accessed: 2023-12-31, 2021.

Kreklow, J., Tetzlaff, B., Kuhnt, G., and Burkhard, B.: A Rainfall Data Intercomparison Dataset of RADKLIM, RADOLAN, and Rain Gauge Data for Germany, Zenodo, doi:10.5281/zenodo.3262172, dataset License: CC-BY-SA 4.0, 2019.

Kreklow, J., Tetzlaff, B., Burkhard, B., and Kuhnt, G.: Radar-based precipitation climatology in germany-developments, uncertainties and potentials, Atmosphere, 11, doi:10.3390/atmos11020217, 2020.

Kunkel, K. and Frankson, R.: Global Land Surface Extremes of Precipitation, Journal of Extreme Events, 02, 1550 004, doi:10.1142/S2345737615500049, 2015.

Kunz, M., Sander, J., and Kottmeier, C.: Recent trends of thunderstorm and hailstorm frequency and their relation to atmospheric characteristic s in southwest Germany, Royal Meteorological Society, 29, 2283–2297, doi:10.1002/joc.1865, 2009.

Lamb, H. H.: British Isles weather types and a register of daily sequence of circulation patterns, 1861-1971, Geophysical Memoirs, pp. 1–85, 1972.

Lees, T., Buechel, M., Anderson, B., Slater, L., Reece, S., Coxon, G., and Dadson, S. J.: Benchmarking data-driven rainfall-runoff models in Great Britain: A comparison of long short-term memory (LSTM)-based models with four lumped conceptual models, Hydrology and Earth System Sciences, 25, 5517–5534, doi:10.5194/hess-25-5517-2021, 2021.

Lees, T., Reece, S., Kratzert, F., Klotz, D., Gauch, M., Bruijn, J. D., Sahu, R. K., Greve, P., Slater, L., and Dadson, S. J.: Hydrological concept formation inside long short-term memory (LSTM) networks, Hydrology and Earth System Sciences, 26, 3079–3101, doi:10.5194/hess-26-3079-2022, 2022.

Lemordant, L., Gentine, P., Swann, A. S., Cook, B. I., and Scheff, J.: Critical impact of vegetation physiology on the continental hydrologic cycle in response to increasing CO2, Proceedings of the National Academy of Sciences of the United States of America, 115, 4093–4098, doi:10.1073/pnas.1720712115, 2018.

Lenderink, G. and Van Meijgaard, E.: Increase in hourly precipitation extremes beyond expectations from temperature changes, Nature Geoscience, 1, 511–514, doi:10.1038/ngeo262, 2008.

Lengfeld, K., Winterrath, T., Junghänel, T., Hafer, M., and Becker, A.: Characteristic spatial extent of hourly and daily precipitation events in Germany derived from 16 years of radar data, Meteorologische Zeitschrift, 28, 363–378, doi:10.1127/metz/2019/0964, 2019.

LfU-RLP - Landesamt für Umwelt Rheinland-Pfalz: Discharge data Rhineland-Palatine, URL https://wasserportal.rlp-umwelt.de, accessed: 2022-03-02, 2022.

LIST - Luxembourg Institute of Science and Technology, Hydro-Climatological Observation network (HOST): Hourly Precipitation, 15-minute Discharge, URL https://envdata.private.list.lu/, accessed: 2022-04-01, 2022.

Llasat, M. C., Marcos, R., Llasat-Botija, M., Gilabert, J., Turco, M., and Quintana-Seguí, P.: Flash flood evolution in North-Western Mediterranean, Atmospheric Research, 149, 230–243, doi:10.1016/j.atmosres.2014.05.024, 2014.

Llasat, M. C., Marcos, R., Turco, M., Gilabert, J., and Llasat-Botija, M.: Trends in flash flood events versus convective precipitation in the Mediterranean region: The case of Catalonia, Journal of Hydrology, 541, 24–37, doi:10.1016/j.jhydrol.2016.05.040, 2016.

Loritz, R., Stoelzle, M., Guse, B., Heidbüchel, I., Tarasova, L., Mälicke, M., Hassler, S., Ebeling, P., and Kiesel, J.: CAMELS-DE: Initiative für einen konsistenten Datensatz für hydro-meteorologische Analysen in Einzugsgebieten, Tag der Hydrologie (TdH), Munich, doi:10.5281/zenodo.6517142, 2022.

Lucius, M.: Notes on the geological map of Luxembourg – the Gutland (Erläuterungen zur geologischen Spezialkarte Luxemburgs – Das Gutland), Publ. Serv. Geol. Luxemb., 1 edn., 1948.

Lupo, A. R.: Atmospheric blocking events: a review, Annals of the New York Academy of Sciences, doi:10.1111/nyas.14557, 2020.

Lupo, A. R.: Atmospheric blocking events: a review, Annals of the New York Academy of Sciences, 1504, 5–24, doi:10.1111/nyas.14557, 2021.

Luxemburger Wort: Luxemburger Wort - Archiv, URL https://www.wort.lu/archive/, accessed: 2021-07-06, 2021.

LVG - Landesamt für Vermessung und Geobasisinformation: Digitale Geländemodelle - Vermessungs- und Katasterverwaltung Rheinland-Pfalz, URL https://lvermgeo.rlp.de/geodaten-geoshop/open-data, accessed: 2024-05-25, 2021.

Madakumbura, G. D., Kim, H., Utsumi, N., Shiogama, H., Fischer, E. M., Seland, Ø., Scinocca, J. F., Mitchell, D. M., Hirabayashi, Y., and Oki, T.: Event-to-event intensification of the hydrologic cycle from 1.5 °C to a 2 °C warmer world, Scientific Reports, 9, doi:10.1038/s41598-019-39936-2, 2019.

Mansell, M. G.: The Effect of Climate Change on Rainfall Trends and Flooding Risk in the West of Scotland, Nordic Hydrology, 28, 37–50, doi:10.2166/nh.1997.0003, 1997.

Marchi, L., Borga, M., Preciso, E., and Gaume, E.: Characterisation of selected extreme flash floods in Europe and implications for flood risk management, Journal of Hydrology, 394, 118–133, doi:10.1016/j.jhydrol.2010.07.017, 2010.

Mardhel, V., Pinson, S., and Allier, D.: Description of an indirect method (IDPR) to determine spatial distribution of infiltration and runoff and its hydrogeological applications to the French territory, Journal of Hydrology, 592, doi:10.1016/j.jhydrol.2020.125609, 2021.

Markowski, P. and Richardson, Y.: Hazards Associated with Deep Moist Convection, 1, John Wiley & Sons, Ltd, doi:10.1002/9780470682104.ch10, 2010.

Martinkova, M. and Kysely, J.: Overview of observed clausius-clapeyron scaling of extreme precipitation in midlatitudes, Atmosphere, 11, 1–16, doi:10.3390/ATMOS11080786, 2020.

Mathias, L.: Major flood event in the Mullerthal region on 1 June 2018: event analysis and predictability, MeteoLux, pp. 1–17, URL https://www.meteolux.lu/de/filedownload/596/floodmullerthal_fullreport_en_final-1-2.pdf/type/pdf, accessed: 2024-07-06, 2019.

Mathias, L.: Synoptic-mesoscale analysis of the flash-flood-producing thunderstorm over the Vallée de l'Ernz on 22 July 2016, MeteoLux, pp. 1–18, URL https://www.meteolux.lu/IMG/pdf/floodernztal_fullreport_en-2.pdf, accessed: 2023-12-31, 2021.

MECB - Ministère de l'Environnement, du Climat et du Développement durable & MEA - Ministère de l'énergie et de l'Aménagement du territoire: LIS-L Land Use 2018, URL https://data.public.lu/fr/datasets/lis-l-land-use-2007-2015-2018/, accessed: 2024-05-25, 2018.

Meischner, P.: Weather Radar: Principles and Advanced Applications, Springer Berlin Heidelberg, Berlin, ISBN: 9783662052037, 2014.

MeteoLux: Precipitation data, URL https://www.meteolux.lu/de/klima/wetterstation/, accessed: 2024-06-23, 2024.

Meyer, J., Douinot, A., Zehe, E., Tamez-Meléndez, C., Francis, O., and Pfister, L.: Impact of Atmospheric Circulation on Flooding Occurrence and Type in Luxembourg (Central Western Europe), EGU General Assembly 2020, Online, 4-8 May 2020, doi:10.5194/egusphere-egu2020-13953, 2020.

Meyer, J., Neuper, M., Mathias, L., Zehe, E., and Pfister, L.: Atmospheric conditions favouring extreme precipitation and flash floods in temperate regions of Europe, Hydrology and Earth System Sciences, 26, 6163–6183, doi:10.5194/hess-26-6163-2022, 2022.

Michaelides, S. C.: Precipitation: Advances in measurement, estimation, and prediction., Springer, 1 edn., doi:10.1007/978-3-540-77655-0, 2008.

Milly, P. C. and Dunne, K. A.: Potential evapotranspiration and continental drying, Nature Climate Change, 6, 946–949, doi:10.1038/nclimate3046, 2016.

Mishra, V., Wallace, J. M., and Lettenmaier, D. P.: Relationship between hourly extreme precipitation and local air temperature in the United States, Geophysical Research Letters, 39, doi:10.1029/2012GL052790, 2012.

Mohr, S., Wilhelm, J., Wandel, J., Kunz, M., Portmann, R., Punge, H. J., Schmidberger, M., Quinting, J. F., and Grams, C. M.: The role of large-scale dynamics in an exceptional sequence of severe thunderstorms in Europe May–June 2018, Weather and Climate Dynamics, 1, 325–348, doi:10.5194/wcd-1-325-2020, 2020.

Mohr, S., Ehret, U., Kunz, M., Ludwig, P., Caldas-Alvarez, A., Daniell, J. E., Ehmele, F., Feldmann, H., Franca, M. J., Gattke, C., Hundhausen, M., Knippertz, P., Küpfer, K., Mühr, B., Pinto, J. G., Quinting, J., Schäfer, A. M., Scheibel, M., Seidel, F., and Wisotzky, C.: A multi-disciplinary analysis of the exceptional flood event of July 2021 in central Europe - Part 1: Event description and analysis, Natural Hazards and Earth System Sciences, 23, 525–551, doi:10.5194/nhess-23-525-2023, 2023.

Muñoz Sabater, J.: ERA5-Land hourly data from 1981 to present, Copernicus Climate Change Service (C3S) Climate Data Store (CDS), doi:10.24381/cds.e2161bac, 2019.

Müller, E. N. and Pfister, A.: Increasing occurrence of high-intensity rainstorm events relevant for the generation of soil erosion in a temperate lowland region in Central Europe, Journal of Hydrology, 411, 266–278, doi:10.1016/j.jhydrol.2011.10.005, 2011.

Nash, E. and Sutcliffe, V.: River flow forecasting through conceptual models Part I - A discussion of principles, Journal of Hydrology, 10, 282–290, doi:10.1016/0022-1694(70)90255-6, 1970.

Nearing, G., Cohen, D., Dube, V., Gauch, M., Gilon, O., Harrigan, S., Hassidim, A., Klotz, D., Kratzert, F., Metzger, A., Nevo, S., Pappenberger, F., Prudhomme, C., Shalev, G., Shenzis, S., Tekalign, T. Y., Weitzner, D., and Matias, Y.: Global prediction of extreme floods in ungauged watersheds, Nature, 627, 559–563, doi:10.1038/s41586-024-07145-1, 2024.

Nearing, G. S., Pelissier, C. S., Kratzert, F., Klotz, D., Gupta, H. V., Frame, J. M., and Sampson, A. K.: Physically Informed Machine Learning for Hydrological Modeling Under Climate Nonstationarity, Tech. rep., NOAA's National Weather Service, 44th NOAA Annual Climate Diagnostics and Prediction Workshop, Durham, NC, 22-24 October 2019, URL https://api.mdsoar.org/server/api/core/bitstreams/d8f1b8b7-8800-4b85-9288-6deb90b4d50a/content, accessed: 2024-06-16, 2019.

Nearing, G. S., Kratzert, F., Sampson, A. K., Pelissier, C. S., Klotz, D., Frame, J. M., Prieto, C., and Gupta, H. V.: What Role Does Hydrological Science

Play in the Age of Machine Learning?, Water Resources Research, 57, 1–15, doi:10.1029/2020WR028091, 2021.

NWS: National Weather Service Glossary, URL https://forecast.weather.gov/glossary.php, accessed: 2022-08-22, 2021.

Oddo, P. C., Bolten, J. D., Kumar, S. V., and Cleary, B.: Deep Convolutional LSTM for improved flash flood prediction, Frontiers in Water, 6, doi:10.3389/frwa.2024.1346104, 2024.

Oudin, L., Hervieu, F., Michel, C., Perrin, C., and Andréassian, V.: Which potential evapotranspiration input for a lumped rainfall–runoff model? Part 2 – Towards a simple and efficient potential evapotranspiration model for rainfall–runoff modelling, Journal of Hydrology, 303, 290–306, doi:10.1016/j.jhydrol.2004.08.026, 2005.

Owen, P. W., Roberts, G., Prigent, O., Markus, R., Tanguy, B., Bridgford, M., Katharina, B., Ciabatti, I., Gatter, L., Gilson, V., Kubat, J., Laanes, L., Simeonova, R., Critoph, H., and Annette, Z.: Flood Directive: progress in assessing risks, while planning and implementation need to improve, Tech. Rep. 25, European Union, Luxembourg, doi:10.2865/356339, 2018.

Pardé, M.: Fleuves et rivières, Colin, Armand, Paris, 1947.

Pfahl, S., O'Gorman, P. A., and Fischer, E. M.: Understanding the regional pattern of projected future changes in extreme precipitation, Nature Climate Change, 7, 423–428, doi:10.1038/NCLIMATE3287, 2017.

Pfister, L.: Hydrological processes in the Alzette river basin - On the potential and difficulties of interdisciplinary approaches in experimental hydrology, University of Strasbourg, p. 128, 2012.

Pfister, L., Humbert, J., and Hoffmann, L.: Recent trends in rainfall-runoff characteristics in the Alzette river basin, Luxembourg, Climatic Change, 45, 323–337, doi:10.1023/A:1005567808533, 2000.

Pfister, L., Kwadijk, J., Musy, A., Bronstert, A., and Hoffmann, L.: Climate change, land use change and runoff prediction in the Rhine-Meuse basins, River Research and Applications, 20, 229–241, doi:10.1002/rra.775, 2004.

Pfister, L., Wagner, C., Vansuypeene, E., Drogue, G., and Hoffmann, L.: Atlas climatique du grand-duché de Luxembourg, Musée national d'histoire naturelle, Société des naturalistes luxembourgeois, Centre de recherche public Gabriel Lippmann, Administration des services techniques de l'agriculture, Luxembourg, ISBN: 2-919877-24-0, 2005.

Pfister, L., Martínez-Carreras, N., Hissler, C., Klaus, J., Carrer, G. E., Stewart, M. K., and McDonnell, J. J.: Bedrock geology controls on catchment storage, mixing, and release: A comparative analysis of 16 nested catchments, Hydrological Processes, 31, 1828–1845, doi:10.1002/hyp.11134, 2017.

Pfister, L., Faber, O., Hostache, R., Iffly, J. F., Matgen, P., Minette, F., Trebs, I., Bastian, C., Göhlhausen, D., Meisch, C., and Patz, N.: Crue éclair du 22 juillet 2016 dans la region de Larochette - Étude méchanistique et fréquentielle réalisée en 2018 pour le compte de l'Administration de la gestion de l'eau, Tech. rep., Administration de la gestion de l'eau, Esch-sur-Alzette, URL https://eau.gouvernement.lu/dam-assets/publications/crue-éclair-du-22-juillet-2016/1812-LIST-BrochureCrueEclair.pdf, accessed: 2023-12-30, 2018.

Pfister, L., Douinot, A., Hostache, R., Iffly, J. F., Matgen, P., Minette, F., Bastian, C., Gilbertz, C., Göhlhausen, D., Meisch, C., and Patz, N.: Crues subites 2018 - Étude méchanistique et fréquentielle des crues subites de 2018 au Luxembourg, Tech. rep., Administration de la gestion de l'eau, Esch-sur-Alzette, URL https://eau.gouvernement.lu/fr/services-aux-citoyens/publications/2021/brochures/Crues-subites-2018.html, accessed: 2023-12-30, 2020.

Piper, D., Kunz, M., Ehmele, F., Mohr, S., Mühr, B., Kron, A., and Daniell, J.: Exceptional sequence of severe thunderstorms and related flash floods in May and June 2016 in Germany – Part 1: Meteorological background, Natural Hazards and Earth System Sciences, 16, 2835–2850, doi:10.5194/nhess-16-2835-2016, 2016.

Púčik, T., Groenemeijer, P., Rýva, D., and Kolář, M.: Proximity soundings of severe and nonsevere thunderstorms in central Europe, Monthly Weather Review, 143, 4805–4821, doi:10.1175/MWR-D-15-0104.1, 2015.

Púčik, T., Groenemeijer, P., Rädler, A. T., Tijssen, L., Nikulin, G., Prein, A. F., van Meijgaard, E., Fealy, R., Jacob, D., and Teichmann, C.: Future changes in European severe convection environments in a regional climate model ensemble, Journal of Climate, 30, 6771–6794, doi:10.1175/JCLI-D-16-0777.1, 2017.

Pöschmann, J. M., Kim, D., Kronenberg, R., and Bernhofer, C.: An analysis of temporal scaling behaviour of extreme rainfall in Germany based on radar precipitation QPE data, Natural Hazards and Earth System Sciences, 21, 1195–1207, doi:10.5194/nhess-21-1195-2021, 2021.

Qi, D. and Majda, A. J.: Using machine learning to predict extreme events in complex systems, Proceedings of the National Academy of Sciences of the USA, 117, 52–59, doi:10.1073/pnas.1917285117, 2020.

Rädler, A. T., Groenemeijer, P., Faust, E., and Sausen, R.: Detecting severe weather trends using an additive regressive convective hazard model (AR-CHaMo), Journal of Applied Meteorology and Climatology, 57, 569–587, doi:10.1175/JAMC-D-17-0132.1, 2018.

Rasmussen, K. L., Prein, R. M., Rasmussen, A. F., Ikeda, C., and Liu, K.: Changes in the convective population and thermodynamic environments in convection-permitting regional climate simulations over the United States, Climate Dynamics, 55, 383–408, doi:10.1007/s00382-017-4000-7, 2017.

Rauber, R. M., Charlevoix, D. J., and Walsh, J. E.: Severe and hazardous weather: an introduction to high impact meteorology, Kendall/Hunt Publishing Company, Dubuque, Iowa, ISBN: 9781524999841, 3 edn., 2008.

Rauthe, M., Brendel, C., Helms, M., Lohrengel, A.-F., Meine, L., Nilson, E., Norpoth, M., Rasquin, C., Rudolph, E., Schade, N. H., Deutschländer, T., Forbriger, M., Fleischer, C., Ganske, A., Herrmann, C., Kirsten, J., Möller, J., and Seiffert, R.: Klimawirkungsanalyse des Bundesverkehrssystems im Kontext Hochwasser: Schlussbericht des Schwerpunktthemas Hochwassergefahren (SP-103) im Themenfeld 1 des BMVI-Expertennetzwerks, Tech. rep., BMDV - Expertennetzwerk, doi:10.5675/ExpNRM2020.2020.04, accessed: 2024-06-09, 2020.

RGE ALTI - Institut National de l'Information Géographique et Forestière: Le modèle numérique de terrain (MNT) maillé qui décrit le relief du territoire français à grande échelle, URL `https://geoservices.ign.fr/rgealti`, accessed: 2024-05-25, 2020.

Ruiz-Villanueva, V., Borga, M., Zoccatelli, D., Marchi, L., Gaume, E., and Ehret, U.: Extreme flood response to short-duration convective rainfall in South-West Germany, Hydrology and Earth System Sciences, 16, 1543–1559, doi:10.5194/hess-16-1543-2012, 2012.

Sappington, J. M., Longshore, K. M., and Thompson, D. B.: Quantifying Landscape Ruggedness for Animal Habitat Analysis: A Case Study Using Bighorn Sheep in the Mojave Desert, The Journal of Wildlife Management, 71, 1419–1426, doi:10.2193/2005-723, 2007.

Scheff, J. and Frierson, D. M.: Scaling potential evapotranspiration with greenhouse warming, Journal of Climate, 27, 1539–1558, doi:10.1175/JCLI-D-13-00233.1, 2014.

Schmithüsen, J.: Das Klima in Das Luxemburger Land - Landesnatur, Volkstum und bäuerliche Wirtschaft, S. Hirzel, Leipzig, 1940.

Schroeder, A., Basara, J., and Shepherd, J. Marshall, Nelson, S.: Insights into Atmospheric Contributors to Urban Flash Flooding across the United States Using an Analysis of Rawinsonde Data and Associated Calculated Parameters, Journal of Applied Meteorology and Climatology, 55, 313–323, doi:10.1175/JAMC-D-14-0232.1, 2016.

Schumacher, R. S. and Johnson, R. H.: Characteristics of U . S . Extreme Rain Events during 1999 – 2003, Weather and forecasting, 21, 69–85, doi:10.1175/WAF900.1, 2006.

Sevruk, B.: Correction of precipitation measurements, summary report. In: Sevruk, B. (Eds.): Correction of Precipitation Measurements, ETH/IASH/WMO Workshop on the Correction of Precipitation Measurements, Zürich, April 1–3, 1985, Züricher Geographische Schriften 23, ETH, Geographisches Institut, Zürich, pp. 13–23, 1986.

Shen, C., Laloy, E., Elshorbagy, A., Albert, A., Bales, J., Chang, F. J., Ganguly, S., Hsu, K. L., Kifer, D., Fang, Z., Fang, K., Li, D., Li, X., and Tsai, W. P.: HESS Opinions: Incubating deep-learning-powered hydrologic science advances as a community, Hydrology and Earth System Sciences, 22, 5639–5656, doi:10.5194/hess-22-5639-2018, 2018.

Shen, C., Chen, X., and Laloy, E.: Editorial: Broadening the Use of Machine Learning in Hydrology, doi:10.3389/frwa.2021.681023, 2021.

Sikorska-Senoner, A. E. and Seibert, J.: Flood-type trend analysis for alpine catchments, Hydrological Sciences Journal, 65, 1281–1299, doi:10.1080/02626667.2020.1749761, 2020.

Slater, L. J., Anderson, B., Buechel, M., Dadson, S., Han, S., Harrigan, S., Kelder, T., Kowal, K., Lees, T., Matthews, T., Murphy, C., and Wilby, R. L.: Nonstationary weather and water extremes: A review of methods for their detection, attribution, and management, doi:10.5194/hess-25-3897-2021, 2021.

Song, T., Ding, W., Wu, J., Liu, H., Zhou, H., and Chu, J.: Flash flood forecasting based on long short-term memory networks, Water (Switzerland), 12, doi:10.3390/w12010109, 2020.

SPW - Service Public de Wallonie: Relief de la Wallonie - Modèle Numérique de Terrain (MNT) 2013-2014, URL https://geoportail.wallonie.be/catalogue/6029e738-f828-438b-b10a-85e67f77af92.html, accessed: 2024-05-25, 2014.

Stendel, M., Francis, J., White, R., Williams, P. D., and Woollings, T.: The jet stream and climate change, pp. 327–357, Elsevier, doi:10.1016/B978-0-12-821575-3.00015-3, 2021.

Strangeways, I.: Precipitation : theory, measurement and distribution, Cambridge University Press, Cambridge, ISBN: 13978-0-521-85117-6, 2007.

Tandon, N. F., Zhang, X., and Sobel, A. H.: Understanding the Dynamics of Future Changes in Extreme Precipitation Intensity, Geophysical Research Letters, 45, 2870–2878, doi:10.1002/2017GL076361, 2018.

Tarolli, M., Borga, M., Zoccatelli, D., Bernhofer, C., Jatho, N., and al Janabi, F.: Rainfall Space-Time Organization and Orographic Control on Flash Flood Response: The Weisseritz Event of August 13, 2002, Journal of Hydrologic Engineering, 18, 183–193, doi:10.1061/(asce)he.1943-5584.0000569, 2013.

Taszarek, M., Brooks, H. E., and Czernecki, B.: Sounding-derived parameters associated with convective hazards in Europe, Monthly Weather Review, 145, 1511–1528, doi:10.1175/MWR-D-16-0384.1, 2017.

Taszarek, M., Allen, J. T., Brooks, H. E., Pilguj, N., and Czernecki, B.: Differing trends in United States and European Severe Thunderstorm Environments in a

Warming Climate, Bulletin of the American Meteorological Society, 102, E296–E322, doi:10.1175/BAMS-D-20-0004.1, 2021a.

Taszarek, M., Allen, J. T., Marchio, M., and Brooks, H. E.: Global climatology and trends in convective environments from ERA5 and rawinsonde data, Climate and Atmospheric Science, 4, 1–11, doi:10.1038/s41612-021-00190-x, 2021b.

Thackeray, C. W., DeAngelis, A. M., Hall, A., Swain, D. L., and Qu, X.: On the Connection Between Global Hydrologic Sensitivity and Regional Wet Extremes, Geophysical Research Letters, 45, 343–351, doi:10.1029/2018GL079698, 2018.

Trenberth, K. E., Dai, A., Rasmussen, R. M., and Parsons, D. B.: The changing character of precipitation, American Meteorological Society, pp. 1205–1218, doi:10.1175/BAMS-84-9-1205, 2003.

Uhan, J., Andjelov, M., Mardhel, V., and Frantar, P.: Index of development and persistence of the river networks (IDPR) as a component of regional groundwater vulnerability assessment in Slovenia., Proceedings on the International Conference on Groundwater vulnerability assessment and mapping. Ustron, Poland, pp. 15–18, 2004.

Van Campenhout, J., Hallot, E., Houbrechts, G., Peeters, A., Levecq, Y., Gérard, P., and Petit, F.: Flash floods and muddy floods in Wallonia: Recent temporal trends, spatial distribution and reconstruction of the hydrosedimentological fluxes using flood marks and sediment deposits, Belgeo, 1, 0–26, doi:10.4000/belgeo.16409, 2015.

Van Delden, A.: The synoptic setting of thunderstorms in Western Europe, Atmospheric Research, 56, 89–110, doi:10.1016/S0169-8095(00)00092-2, 2001.

Vogel, K., Ozturk, U., Riemer, A., Laudan, J., Sieg, T., Wendi, D., and Agarwal, A.: Die Sturzflut von Braunsbach am 29. Mai 2016 – Entstehung, Ablauf und Schäden eines „Jahrhundertereignisses“. Teil 2: Geomorphologische Prozesse und Schadensanalyse, Hydrologie und Wasserbewirtschaftung, 61, 163–175, doi:10.5675/HyWa, 2017.

Weigl, E. and Winterrath, T.: Radargestütze Niederschlagsanalyse und -vorhersage (RADOLAN, RADVOR-OP), Promet, 35, 76–86, 2009.

Weigl, E., Reich, T., Lang, P., Wagner, A., Kohler, O., Gerlach, N., and Bartels, H.: Routineverfahren zur Online-Aneichung der Radarniederschlagsdaten mithilfe von automatischen Bodenniederschlagsstationen (Ombrometer), Tech. rep., German Weather Service: Hydrometeorology department, German Weather Service: Hydrometeorology department, Offenbach am Main, URL https://www.dwd.de/DE/leistungen/radolan/radolan_info/abschlussbericht_pdf, accessed: 2023-12-31, 2004.

Westermayer, A. T., Groenemeijer, P., Pistotnik, G., Sausen, R., and Faust, E.: Identification of favorable environments for thunderstorms in reanalysis data, Meteorologische Zeitschrift, 26, 59–70, doi:10.1127/metz/2016/0754, 2017.

Whiteman, C. D.: Mountain Meteorology - Fundamentals and Applications, Oxford University Press, doi:10.1093/oso/9780195132717.001.0001, 2000.

Wilbrand, K., Taormina, R., ten Veldhuis, M. C., Visser, M., Hrachowitz, M., Nuttall, J., and Dahm, R.: Predicting streamflow with LSTM networks using global datasets, Frontiers in Water, 5, doi:10.3389/frwa.2023.1166124, 2023.

Wilson, J. W. and Brandes, E. A.: Radar Measurement of Rainfall - A Summary, Armerican Meteorological Society, 60, 1048–1058, doi:10.1175/1520-0477(1979)060<1048:RMORS>2.0.CO;2, 1979.

Winterrath, T., Brendel, C., Hafer, M., Junghänel, T., Klameth, A., Walawender, E., Weigl, E., and Becker, A.: Erstellung einer radargestützten Niederschlagsklimatologie, Tech. rep., Reports of the German Weather Service, No. 251, Offenbach am Main, doi:10.17169/refubium-25153, 2017.

Winterrath, T., Brendel, C., Hafer, M., Junghänel, T., Klameth, A., Lengfeld, K., Walawender, E., Weigl, E., and Becker, A.: RADKLIM Version 2017.002: Reprocessed quasi gauge-adjusted radar data, 5-minute precipitation sums (YW), Tech. rep., German Weather Service (DWD), doi:10.5676/DWD/RADKLIM_YW_V2017.002, 2018.

WMO - World Meteorological Organisation: Flash Flood Guidance System (FFGS) with Global Coverage, URL `https://public-old.wmo.int/en/projects/ffgs`, accessed: 2023-12-30, 2017.

Wood, S. J., Jones, D. A., and Moore, R.: Static and dynamic calibration of radar data for hydrological use, Hydrology and Earth System Sciences, 4, 545–554, doi:10.5194/hess-4-545-2000, 2000.

Woollings, T., Barriopedro, D., Methven, J., Son, S. W., Martius, O., Harvey, B., Sillmann, J., Lupo, A. R., and Seneviratne, S.: Blocking and its Response to Climate Change, Current Climate Change Reports, 4, 287–300, doi:10.1007/s40641-018-0108-z, 2018.

Wrede, S., Fenicia, F., Martínez-Carreras, N., Juilleret, J., Hissler, C., Krein, A., Savenije, H. H. G., Uhlenbrook, S., Kavetski, D., and Pfister, L.: Towards more systematic perceptual model development: a case study using 3 Luxembourgish catchments, Hydrological Processes, 29, 2731–2750, doi:10.1002/hyp.10393, 2015.

Wu, P., Christidis, N., and Stott, P.: Anthropogenic impact on Earth's hydrological cycle, Nature Climate Change, 3, 807–810, doi:10.1038/nclimate1932, 2013.

Yang, D., Yang, Y., and Xia, J.: Hydrological cycle and water resources in a changing world: A review, doi:10.1016/j.geosus.2021.05.003, 2021.

Yilmaz, K. K., Gupta, H. V., and Wagener, T.: A process-based diagnostic approach to model evaluation: Application to the NWS distributed hydrologic model, Water Resources Research, 44, W09 417, doi:10.1029/2007WR006716, 2008.

List of Tables

List of Figures

List of Publications

First author articles

Meyer, J., Neuper, M., Mathias, L., Zehe, E., and Pfister, L.: Atmospheric conditions favouring extreme precipitation and flash floods in temperate regions of Europe, Hydrol. Earth Syst. Sci., 26, 6163–6183, doi: 10.5194/hess-26-6163-2022, 2022a.

Nijzink, J., Loritz, R., Gourdol, L., Iffly, J. F., Zoccatelli, D. and Pfister, L.: CAMELS-LUX: Highly resolved hydro-meteorological and atmospheric data for physiographically characterized catchments around Luxembourg, Earth Syst. Sci. Data, 2024, submitted.

Nijzink, J., Loritz, R., Zoccatelli, D. and Pfister, L.: Challenging LSTMs in summer flood modelling in central western Europe (Luxembourg) [in preparation].

Conference contributions

Meyer, J., Douinot, A., Zehe, E., Tamez-Meléndez, C., Francis, O., and Pfister, L.: Impact of Atmospheric Circulation on Flooding Occurrence and Type in Luxembourg (Central Western Europe), EGU General Assembly 2020, Online, 4–8 May 2020, EGU2020-13953, doi: 10.5194/egusphere-egu2020-13953, 2020

Meyer, J., Douinot, A., Neuper, M., Mathias, L., Tamez-Meléndez, C., Zehe, E., and Pfister, L.: Identifying and linking flash flood prone atmospheric conditions to flooding occurrences in central Western Europe, EGU General Assembly 2021, online, 19–30 Apr 2021, EGU21-12522, doi: 10.5194/egusphere-egu21-12522, 2021.

Meyer, J., Loritz, R., Pfister, L., and Zehe, E.: Learning from differing errors between machine learning and a conceptual hydrological model - the case of convective storms and flash floods, EGU General Assembly 2022, Vienna, Austria, 23–27 May 2022, EGU22-12250, doi: 10.5194/egusphere-egu22-12250, 2022b.

Dataset publication

Nijzink, J., Loritz, R., Gourdol, L., Iffly, J. F., Zoccatelli, D. and Pfister, L.: CAMELS-LUX: Highly resolved hydro-meteorological and atmospheric data for physiographically characterized catchments around Luxembourg [Data set], Zenodo, doi: 10.5281/zenodo.13846620, 2024, submitted.

Acknowledgements

I would like to thank:

- my supervisor, Prof. Dr. Laurent Pfister, for continuously supporting me and following up, even in times of lock-down, in German 'exile', on the bureaucratic side or during my first steps in professional situations. He patiently guided me through the Luxembourgish hydrological and meteorological settings and helped placing detailed ideas in the larger context. Thank you for your valuable feedback in numerous iterations (making any text sound nice) and understanding my continuously changing needs.

- my second supervisor, Prof. Dr. Erwin Zehe, for brainstorming with us and always welcoming me at KIT - no matter the circumstances. He strongly encouraged the exchange with the group of the Institute for Water and Environment - Hydrology and connected me with what ended up as the most fruitful collaborations. Without this exchange my thesis would not have been possible in the way it is.

- all co-authors, that motivated me with their ideas and enthusiasm: Audrey Douinot, who helped me to get started in the topic of flash floods and introduced us to field work. Malte Neuper for patiently briefing me with the relevant meteorological context of extreme events and substantially contributing to the concept of analysing atmospheric proxy parameters. Luca Mathias for providing additional meteorological expertise, when I had to walk on thin ice relying on others. Ralf Loritz for introducing me to the world of modelling and making the easy switch from physical based plans to large-scale regional modelling, that perfectly fits contemporary currents. He always came along with valuable new ideas while providing profound scientific and technical background. Davide Zocatelli for being one of my main contact points in the CAT group and taking the time for evaluating and shaping my studies. Jeff Iffly and Laurent Gourdol for their inexhaustible knowledge of the Greater Region of Luxembourg.

- all colleagues of the CAT group, the HYDRO-CSI DTU and especially the ones sharing the office, A001. I am glad to have found like-minded friends to overcome any difficulty that occurred within the PhD journey.

- all my friends and family, who have had my back throughout the journey. I would like to especially mention Julia for help with typesetting and editing in the right moment and Alina for title brainstorming and proofreading at various

stages. Moreover, my mom, for jumping in as first-class babysitter setting her life aside to travel to wherever needed so that I could fulfill the duties of my contract. My thanks also to Timo, who helped in the most incredible manner to balance my life in a healthy way, preventing me from drowning in the tunnel of PhD research.

- Remko, my first point of contact for motivation, discipline, to-do-lists and coding errors. He knows the challenges of a PhD and could professionally help at any point. He knows my thesis inside out mastering all technical details like noone else all the while patiently putting up with me continuously going on about my PhD. Many thanks as well for keeping me free within the last months and spending evening after evening and weekend after weekend with Timo and without me. This shall get better from now on!

- I would like to acknowledge all of the providers of data used in this work: the German Weather Service (DWD) for the RADOLAN and RADKLIM radar data, the Copernicus Climate Change Service for the ERA5 dataset, Catharin Schäfer and Hans Göppert from the engineering consultancy WALD + CORBE for providing their collection of flash flood events, and most importantly LIST, AGE and ASTA for their discharge and precipitation data.

- also the Luxembourgish National Research Fund who funded the HYDRO-SCI Doctoral Training Unit (grant no. PRIDE15/10623093/HYDRO-CSI), LIST that hosted me during my PhD and the Bureau des Etudes Doctorales of the University of Luxembourg that always proved to be flexible to fit my needs.

Supplement

S1 List of catchments

Table S1.1: 56 nested catchments within the CAMELS-LUX data set listed with their meta data.

ID	Gauge (Stream)	Lat	Lon	Area [km^2]	Start	End
1	Livange (Alzette)	49.526477	6.114957	258.34	2004	2021
2	Hesperange (Alzette)	49.586287	6.14908	317.78	2004	2021
3	Pfaffenthal (Alzette)	49.620647	6.132266	388.96	2004	2021
4	Hunsdorf (Alzette)	49.69895	6.13361	441.91	2004	2021
5	Mersch (Alzette)	49.753068	6.115991	736.86	2004	2021
6	Ettelbruck (Alzette)	49.8448	6.098584	1118.33	2004	2021
7	Reichlange (Attert)	49.774226	5.925732	159.49	2004	2021
8	Useldange (Attert)	49.770335	5.985998	247.50	2004	2021
9	Bissen(Attert)	49.784853	6.056414	289.29	2004	2021
10	Livange (Bibeschbach)	49.531667	6.119773	10.63	2004	2021
11	Kautenbach (Clerve)	49.952417	6.021154	230.91	2004	2021
12	Hesperange (Drosbech)	49.586287	6.14908	10.51	2006	2021
13	Bettembourg (Dudelingerbach)	49.508908	6.097123	46.87	2004	2021
14	Hagen (Eisch)	49.650346	5.937105	50.96	2004	2021
15	Hunnebour (Eisch)	49.729184	6.079524	167.00	2004	2021
16	Sinspelt (Enz)	49.970411	6.322601	101.43	2004	2021
17	Huewelerbach (Huewelerbach)	49.71825	5.905708	2.66	2004	2021
18	Gemund (Irsen)	49.992541	6.154194	125.35	2004	2021
19	Kayl (Kaylbach)	49.500286	6.052986	75.21	2004	2021
20	Merkholtz (Kirel)	49.965897	5.968539	66.88	2006	2021
21	Mamer (Mamer)	49.623206	6.023054	17.93	2004	2021
22	Schoenfels (Mamer)	49.723112	6.100795	81.65	2004	2021
23	Huncherange (Mierbech)	49.518907	6.061947	6.80	2004	2021
24	Giesdorf (Nims)	50.174633	6.454355	16.69	2004	2021
25	Seffern (Nims)	50.064356	6.499988	137.10	2004	2021
26	Alsdorf-Oberecken (Nims)	49.883608	6.462262	264.21	2004	2021
27	Dasbourg (Our)	50.049832	6.126077	447.93	2004	2021
28	Gemund (Our)	49.985333	6.1715	612.05	2004	2021

Continued on next page

ID	Gauge (Stream)	Lat	Lon	Area [km^2]	Start	End
29	Vianden (Our)	49.939224	6.204738	636.88	2004	2021
30	Niederpallen (Pall)	49.754673	5.91413	32.97	2004	2021
31	Luxembourg (Petrusse)	49.606702	6.132359	44.58	2004	2020
32	Prüm (Prüm)	50.21939	6.439864	53.12	2004	2021
33	Echtershausen (Prüm)	50.022304	6.418312	325.58	2004	2021
34	Prümzurlay (Prüm)	49.866647	6.437269	575.71	2004	2021
35	Platen (Roudbach)	49.785259	5.935675	43.96	2004	2021
36	Cessange (Ruisseau de Cessange)	49.598469	6.12	13.6904	2007	2021
37	Colpach (Rau de Colpach)	49.768578	5.819138	18.96	2006	2021
38	Merl (Ruisseau de Merl)	49.59941	6.109055	26.78	2005	2021
39	Useldange (Schwebich)	49.76472	5.977705	30.13	2004	2021
40	Bigonville (Sure)	49.869821	5.801399	308.35	2004	2021
41	Heiderscheidergrund (Sure)	49.901196	5.950724	429.91	2004	2021
42	Michelau (Sure)	49.895421	6.091178	946.48	2004	2021
43	Diekirch (Sure)	49.866622	6.161813	2176.73	2004	2021
44	Bollendorf (Sure)	49.850919	6.359193	3243.51	2004	2021
45	Rosport (Sure)	49.785883	6.509851	4256.62	2004	2021
46	Mertert (Syre)	49.701803	6.4738	201.64	2005	2021
47	Niederfeulen (Wark)	49.855534	6.052637	57.39	2004	2021
48	Welscheid (Wark)	49.883032	6.047939	64.33	2004	2021
49	Ettelbruck (Wark)	49.850643	6.09738	81.35	2004	2017
50	Weierbach (Weierbach)	49.828415	5.797152	0.46	2004	2021
51	Winseler (Wiltz)	49.967894	5.890266	103.87	2004	2021
52	Kautenbach (Wiltz)	49.946524	6.025045	427.94	2004	2021
53	Useldange (Wollefsbach)	49.764402	5.975416	4.49	2004	2021
54	Bous (Aalbach)	49.557468	6.352567	40.86	2006	2021
55	Larochette (Ernz Blanche)	49.791584	6.219358	69.31	2015	2021
56	Hallerbach (Hallerbach)	49.820722	6.321401	19.40	2006	2016

S

S2 List of precipitation stations

Table S2.1: Precipitation stations that were used for the interpolated station product in CAMELS-LUX. The annual precipitation sum is calculated from 2003-2020.

ID	Station	Elevation	Institution	Longitude	Latitude	P [mm/a]
1	Arsdorf	416	ASTA	5.848680	49.858910	669
2	Asselborn	479	ASTA	5.969607	50.096857	616
3	Beringen	216	ASTA	6.111794	49.762003	524
4	Bettendorf	187	ASTA	6.209470	49.874100	511
5	Bigonville	328	AGE	5.801386	49.870038	658
6	Bleesbreck	190	AGE	6.191111	49.871389	517

Continued on next page

ID	Station	Elevation	Institution	Longitude	Latitude	P [mm/a]
7	Bollendorf	172	AGE	6.358056	49.850278	525
8	Boulange	350	LIST	5.965666	49.383029	590
9	Budersberg	400	LIST	6.056289	49.480410	542
10	Burmerange	262	LIST	6.328933	49.494745	484
11	Cessange	316	LIST	6.089277	49.580391	535
12	Clemency	334	ASTA	5.875025	49.598810	603
13	Dahl	474	ASTA	5.980935	49.935958	603
14	Dellen	490	AGE	5.956111	49.860833	694
15	Diekirch	185	AGE	6.150909	49.863565	516
16	Echternach	243	ASTA	6.443379	49.803102	520
17	Esch Sure	345	ASTA	5.921212	49.909078	564
18	Eschdorf	514	ASTA	5.936060	49.880000	633
19	Ettelbruck	254	ASTA	6.089276	49.852864	652
20	Findel	376	MeteoLux	6.203470	49.626100	645
21	Fouhren	356	ASTA	6.187350	49.918490	551
22	Godbrange	325	ASTA	6.235691	49.736373	478
23	Grevenmacher	190	ASTA	6.435413	49.680876	527
24	Harlange	480	AGE	5.798894	49.926580	656
25	Heinerscheid	525	AGE	6.090235	50.093866	613
26	Hersberg	377	LIST	6.316190	49.752750	479
27	Holler	457	ASTA	6.046800	50.122139	635
28	Holtz	463	AGE	5.794499	49.804752	680
29	Hosingen	517	ASTA	6.101470	49.993046	627
30	Huldange	558	AGE	6.023861	50.161787	655
31	Kautenbach	250	AGE	6.024836	49.946497	591
32	Koerich-ASTA	262	ASTA	5.945288	49.679383	650
33	Koerich-AGE	263	AGE	5.945184	49.679393	593
34	Livange	269	AGE	6.115247	49.526388	544
35	Mamer	315	ASTA	6.015620	49.633900	597
36	Merl	307	ASTA	6.091559	49.612945	583
37	Mersch	220	AGE	6.115768	49.753149	537
38	Oberkorn	378	ASTA	5.900897	49.512306	684
39	Olsdorf	328	DWD	6.382000	49.945000	529
40	Perl-Nennig	152	DWD	6.379000	49.535000	530
41	Potaschbierg	260	AGE	6.393733	49.678315	538
42	Reckange	293	ASTA	6.005820	49.562444	560
43	Reichlange	256	AGE	5.926111	49.775460	602
44	Remerschen	183	ASTA	6.349110	49.490980	502
45	Remich	207	ASTA	6.354936	49.545185	526
46	Reuler	492	ASTA	6.036560	50.063314	624
47	Roeser	265	ASTA	6.141727	49.540144	563
48	Roodt-ASTA	437	ASTA	5.820203	49.794506	667
49	Roodt-LIST	488	LIST	5.831247	49.806087	622

Continued on next page

ID	Station	Elevation	Institution	Longitude	Latitude	P [mm/a]
50	Sandweiler	372	LIST	6.210994	49.616949	545
51	Schifflange	282	LIST	6.028375	49.513710	542
52	Schimpach	379	ASTA	5.847459	50.009325	635
53	Schneifelforsthaus	649	DWD	6.419000	50.297000	740
54	Stadtbredimus	224	ASTA	6.358820	49.578980	550
55	Steinsel	247	ASTA	6.123940	49.687320	574
56	Trier-Zewen	132	DWD	6.613000	49.733000	532
57	Trintange	217	ASTA	6.280224	49.574204	521
58	Useldange	280	ASTA	5.967486	49.767397	570
59	Vianden	229	AGE	6.206132	49.941292	559
60	Waldbillig	315	ASTA	6.277300	49.798060	479
61	Walferdange	330	AGE	6.130223	49.668649	552
62	Weierbach	499	LIST	5.794526	49.831967	687
63	Welscheid	271	AGE	6.047131	49.883517	639
64	Wincrange	496	ASTA	5.926335	50.060700	635
65	Wincrange-AGE	497	AGE	5.926308	50.060728	616

S3 Flash flood data base

Table S3.1: Flash flood database used in this manuscript. Region abbreviations are in Germany Baden-Württemberg (Ba-Wü), Rhineland-Palatine (RLP), in France Lorraine (Lo), in Eastern Belgium (BE) and in Luxembourg (LUX).

ID	Date	Location (stream)	Region	Source
1	26/07/2019	Müllheim	Ba-Wü	Wald + Corbe (2021)
2	26/07/2019	Hechingen	Ba-Wü	Wald + Corbe (2021)
3	27/07/2019	Pforzheim-Ispringen	Ba-Wü	Wald + Corbe (2021)
4	27/07/2019	Königsbach-Stein	Ba-Wü	Wald + Corbe (2021)
5	27/07/2019	Gernsbach	Ba-Wü	Wald + Corbe (2021)
6	27/07/2019	Tuttlingen	Ba-Wü	Wald + Corbe (2021)
7	18/06/2019	Ellmendingen (Pfinz)	Ba-Wü	Wald + Corbe (2021)
8	01/06/2018	Müllerthal (Black Ernz)	LUX	Pfister et al. (2020)
9	01/06/2018	Larochette (White Ernz)	LUX	Pfister et al. (2020)
10	01/06/2018	Hallerbach	LUX	Pfister et al. (2020)
11	01/06/2018	Echtershausen (Prüm)	RLP	Johst et al. (2018)
12	01/06/2018	Gemünd (Irsen)	RLP	Johst et al. (2018)
13	01/06/2018	Bierbach (Lünebach)	RLP	Johst et al. (2018)
14	31/05/2018	Ehingen (Würm)	Ba-Wü	Wald + Corbe (2021)
15	27/05/2018	Gerach (Fischbach)	RLP	Johst et al. (2018)
16	22/05/2018	Odenheim	Ba-Wü	Wald + Corbe (2021)
17	22/05/2018	Helmsheim/Heidelsheim	Ba-Wü	Wald + Corbe (2021)

Continued on next page

ID	Date	Location (stream)	Region	Source
18	22/05/2018	Gondelsheim	Ba-Wü	Wald + Corbe (2021)
19	22/07/2016	Hallerbach	LUX	Pfister et al. (2018)
20	22/07/2016	Larochette (White Ernz)	LUX	Pfister et al. (2018)
21	21/07/2016	Audun-le-Tiche	Lo	France3-GrandEst (2016)
22	07/06/2016	Stein	Ba-Wü	Göppert (2018)
23	07/06/2016	Waldkirch (Elz)	Ba-Wü	Göppert (2018)
24	29/05/2016	Braunsbach (Orlacher Bach)	Ba-Wü	Bronstert et al. (2018)
25	29/05/2016	Dallau	Ba-Wü	Göppert (2018)
26	28/05/2016	Waldbrunn	Ba-Wü	Göppert (2018)
27	24/07/2015	Hausen am Tann	Ba-Wü	Wald + Corbe (2021)
28	14/06/2015	Bonndorf	Ba-Wü	Wald + Corbe (2021)
29	06/06/2015	Bretten	Ba-Wü	Göppert (2018)
30	11/07/2014	Saint-Avold (La Roselle)	Lo	France3-GrandEst (2014)
31	12/07/2010	Munzingen	Ba-Wü	Göppert, 2018
32	04/07/2010	Ditzingen (Glems)	Ba-Wü	Göppert (2018)
33	03/07/2009	Ditzingen (Glems)	Ba-Wü	Wald + Corbe (2021)
34	08/06/2008	Britzingen (Ehebach)	Ba-Wü	Göppert (2018)
35	02/06/2008	Rangendingen (Starzel River)	Ba-Wü	Ruiz-Villanueva et al. (2012)
36	02/06/2008	Jungingen	Ba-Wü	Ruiz-Villanueva et al. (2012)
37	30/05/2008	Oberboihingen (Heuspachklingen)	Ba-Wü	Wald + Corbe (2021)
38	09/06/2007	Reichenbach (Fils)	Ba-Wü	Göppert (2018)
39	22/07/2006	Mölschbach (Rambach)	Ba-Wü	Wald + Corbe (2021)
40	05/07/2006	Stebbach (Stebbach)	Ba-Wü	Göppert (2018)

S

References

Bronstert, A., Agarwal, A., Boessenkool, B., Crisologo, I., Fischer, M., Heistermann, M., Köhn-Reich, L., López-Tarazón, J. A., Moran, T., Ozturk, U., Reinhardt-Imjela, C., and Wendi, D.: Forensic hydro-meteorological analysis of an extreme flash flood: The 2016-05-29 event in Braunsbach, SW Germany, Science of the Total Environment, 630, 977–991, doi:https://doi.org/10.1016/j.scitotenv.2018.02.241, 2018.

France3-GrandEst: Saint-Avold : près de 600 interventions après un violent orage, URL https://france3-regions.francetvinfo.fr/grand-est/2014/07/12/saint-avold-pres-de-600-interventions-apres-un-violent-orage-516161.html, accessed: 2024-01-03, 2014.

France3-GrandEst: Des orages et inondations ont touché la Moselle et le Luxembourg, URL https://france3-regions.francetvinfo.fr/grand-est/moselle/des-o

rages-et-inondations-ont-touche-la-moselle-et-le-luxembourg-1053137.html, accessed: 2024-01-03, 2016.

Göppert, H.: Auswertung von abgelaufenen Starkregenereignissen über Radarmessungen, Wasserwirtschaft, 108, 44–50, doi:10.1007/s35147-018-0223-8, URL https://www.wald-corbe.de/upload/pdf/WaWi_2018_11_FA_06_Goeppert.pdf, 2018.

Johst, M.: Hochwasserfrühwarnung für kleine Einzugsgebiete, URL https://lfu.rlp.de/fileadmin/lfu/Downloads/Fachveranstaltung_Starkregen/Top4_Fruehwarnung_Johst_LfU.pdf, 2018.

Pfister, L., Faber, O., Hostache, R., Iffly, J. F., Matgen, P., Minette, F., Trebs, I., Bastian, C., Göhlhausen, D., Meisch, C., and Patz, N.: Crue éclair du 22 juillet 2016 dans la region de Larochette - Étude méchanistique et fréquentielle réalisée en 2018 pour le compte de l'Administration de la gestion de l'eau, URL https://eau.gouvernement.lu/dam-assets/publications/crue-éclair-du-22-juillet-2016/1812-LIST-BrochureCrueEclair.pdf, 2018.

Pfister, L., Douinot, A., Hostache, R., François, I. J., Matgen, P., Minette, F., Bastian, C., Gilbertz, C., Göhlhausen, D., Meisch, C., and Patz, N.: Crues subites 2018 - Étude méchanistique et fréquentielle des crues subites de 2018 au Luxembourg, URL https://eau.gouvernement.lu/fr/services-aux-citoyens/publications/2021/brochures/Crues-subites-2018.html, 2020.

Ruiz-Villanueva, V., Borga, M., Zoccatelli, D., Marchi, L., Gaume, E., and Ehret, U.: Extreme flood response to short-duration convective rainfall in South-West Germany, Hydrology and Earth System Sciences, 16, 1543–1559, doi:10.5194/hess-16-1543-2012, 2012.

Wald + Corbe: Personal communication (Göppert, Hans; Schäfer, Catharin), 2021.

S4 Comparison of trends on differing pressure levels

Trends for specific humidity (q), relative humidity (RH), and wind speed (WS) were compared on differing pressure levels (500 hPa, 700 hPa, 850 hPa). These figures are related to the Fig. 4.3.4 and 4.6.1 in Chapter 4 of the manuscript.

S4.1 Specific humidity (q) at 700 hPa and 850 hPa

For this supplement we used the same thresholds as initially identified for the 700 hPa level. As specific humidity is decreasing with height, we were not able to count enough values above 0.004 kg kg^{-1} at 500 hPa to be able to plot or compare them. At 850 hPa, the positive trend found at 700 hPa remains (Fig. S4.1 e, g). It is, however, less strong in the East of the study area, where it is moreover insignificant (Fig. S4.1 f).

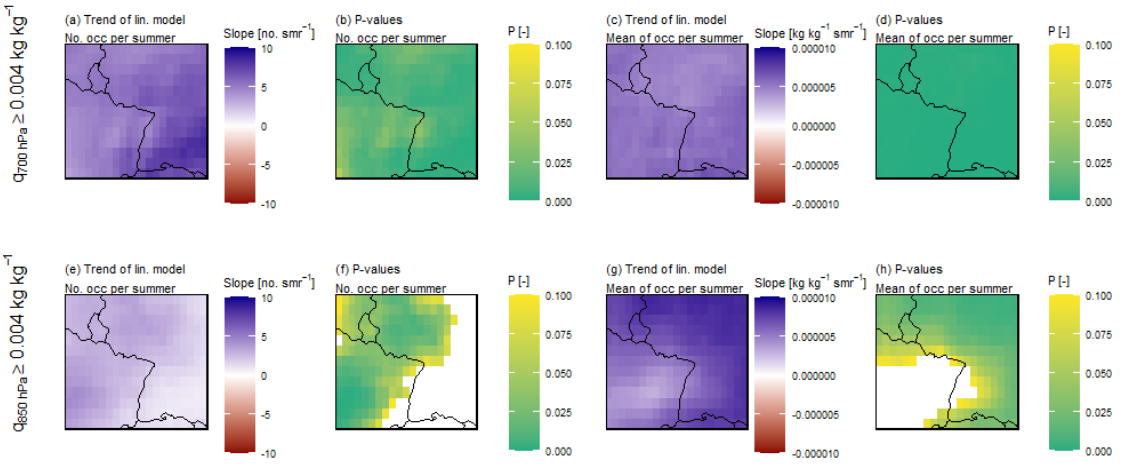

Figure S4.1: Trend analysis of the specific humidity (q) above the identified threshold of 0.004 kg kg^{-1} at two differing pressure levels: 700 hPa and 850 hPa. The first column (a, e) shows the trends of the numbers of hourly occurrences of values above the threshold, including their significance-levels p in the second column (b, f). The third column (c, g) shows the trends of the mean values of all hourly occurrences above the threshold and the last column (d, h) their respective significance-levels. White areas mark insignificance.

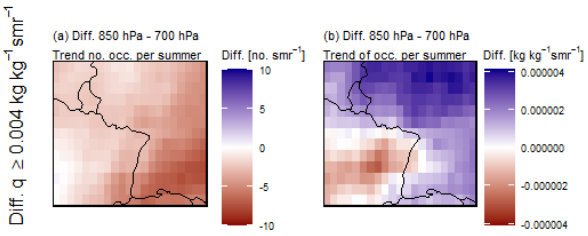

Figure S4.2: The difference of trends in specific humidity (q) above 0.004 kg kg^{-1} smr^{-1} between the pressure levels 850 hPa and 700 hPa regarding the annual number of occurrences (a) and the actual values (b).

S4.2 Relative humidity (RH) at 500 hPa, 700 hPa, 850 hPa

The decrease in relative humidity (RH) is stronger at lower levels of the atmosphere (850 hPa) (Fig. S4.3 i, k), where especially the mean of high RH_{850hPa} is decreasing at a significant level (Fig. S4.3 l). At the 500 hPa pressure level, the decrease in the number of occurrences of $RH_{500hPa} > 59.4\%$ is also stronger (Fig. S4.3 a, b), than at 700 hPa. The actual values above the threshold increased at a very low rate, which was also insignificant (Fig. S4.3 c, d). Concluding, these results show that the 700 hPa level turns out to be a good proxy for RH in the middle of the troposphere.

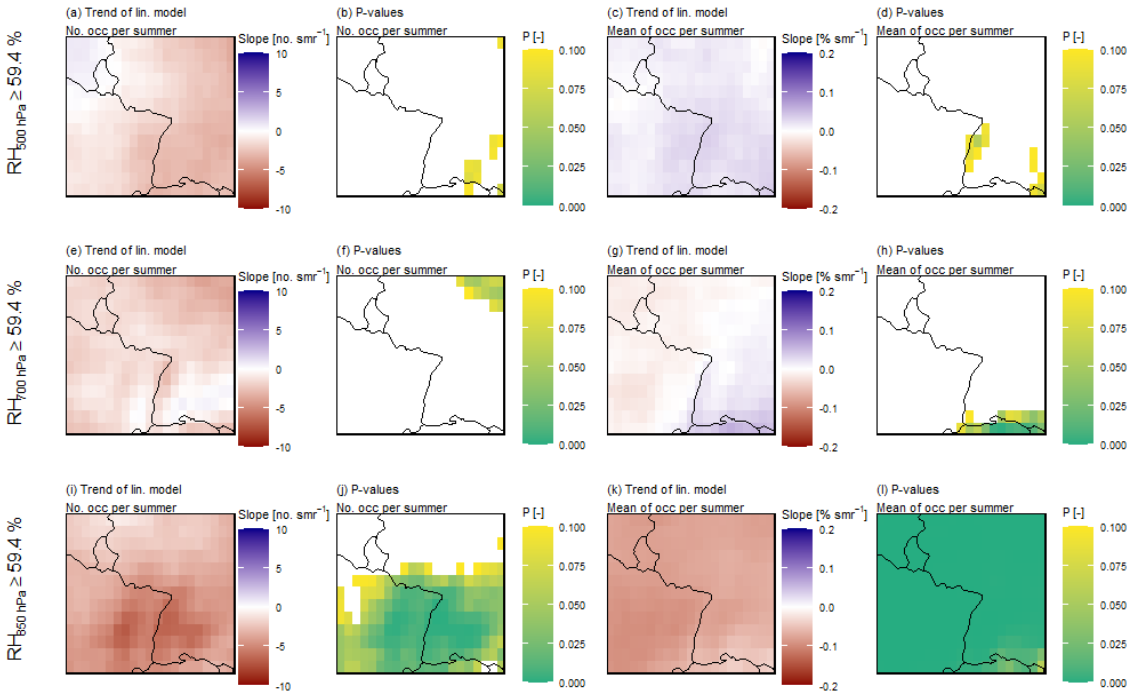

Figure S4.3: Trend analysis of the relative humidity (RH) above the identified threshold of 59.4% at three differing pressure levels: 500 hPa, 700 hPa and 850 hPa. The first column (a, e, i) shows the trends of the numbers of hourly occurrences of values above the threshold, including their significance-levels in the second column (b, f, j). The third column (c, g, k) shows the trends of the mean values of all hourly occurrences above the threshold and the last column (d, h, l) their respective significance-levels p. White areas mark insignificance.

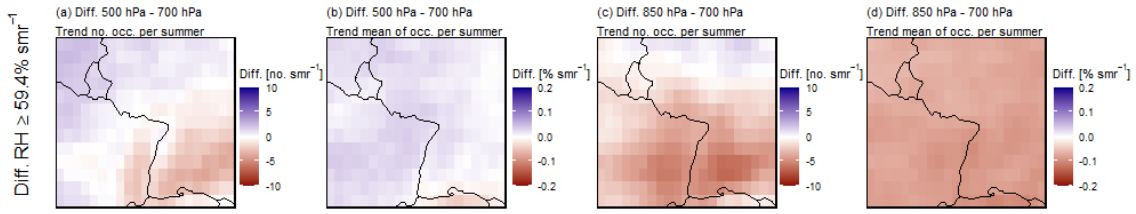

Figure S4.4: The difference of trends in relative humidity (RH) above 59.4% between the pressure levels 500 hPa and 700 hPa (a, b), as well as 850 hPa and 700 hPa (c, d).

S4.3 Windspeed (WS) at 500 hPa, 700 hPa, 850 hPa, and mean between 10 m and 500 hPa

At 500 hPa trends in $\mathrm{WS}_{500hPa} \leq 6.2$ m s^{-1} are showing a stronger, but insignificant decrease compared to the mean of 10 m above the ground level and the pressure level of 500 hPa ($\mathrm{WS}_{10m-500hPa}$) (Fig. S4.5 a-d & m-p, Fig. S4.6 a, b). The WS_{700hPa} at 700 hPa splits the study area in two, where in the north-west, WS_{700hPa} occurrences

below the threshold are decreasing and increasing in the south-west. The decreases in the mean $WS_{850hPa} \leq 6.2$ m s^{-1} at the pressure level 850 hPa are even partly significant (Fig. S4.5 k, l) and occur more often (Fig. S4.5 i, j). $WS_{10m-500hPa}$ shows a strong but insignificant decrease in the number of occurrences of low WS, as well as its mean (Fig. S4.5 m-p). Generally low WS occurs more frequently throughout different levels of the atmosphere and the values at these occurrences are slightly decreasing.

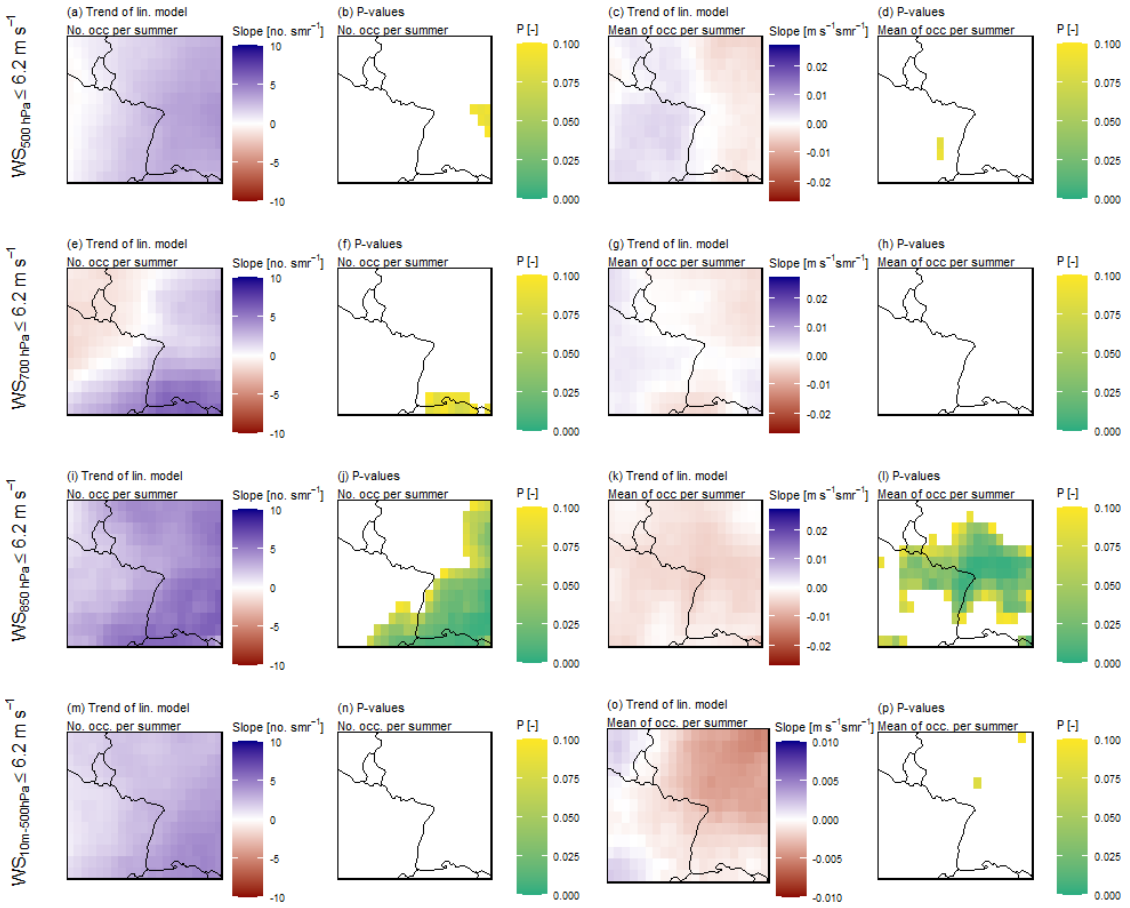

Figure S4.5: Trend analysis of the wind speed (WS) above the identified threshold of 6.2 m s^{-1} at three differing pressure levels (500 hPa, 700 hPa and 850 hPa) as well as considering the mean between the surface (10 m) and the pressure level at 500 hPa. The first column (a, e, i, m) shows the trends of the numbers of hourly occurrences of values above the threshold, including their significance-levels p in the second column (b, f, j, n). The third column (c, g, k, o) shows the trends of the mean values of all hourly occurrences above the threshold and the last column (d, h, l, p) their respective significance-levels p. White areas mark insignificance.

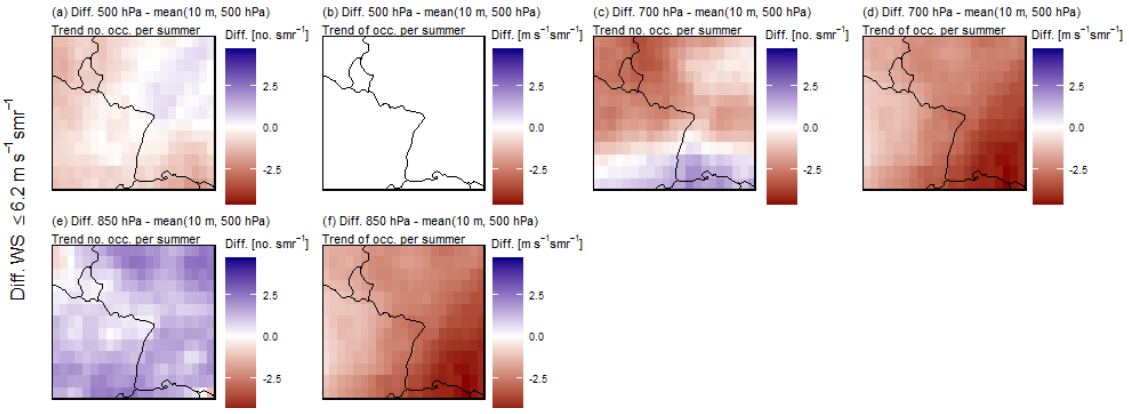

Figure S4.6: The difference of trends in wind speed (WS) below 6.2 m s^{-1} between the pressure levels 500 hPa and the mean of 10 m and 500 hPa (a, b), as well as 700 hPa and the mean of 10 m and 500 hPa (c, d), and 850 hPa and the mean of 10 m and 500 hPa (e, f).

S

S5 Sensitivity of thresholds to the calculation method of atmospheric conditions during precipitation events

We added this supplement to demonstrate the differences between slight variations of our calculation methods to identify the atmospheric data during a precipitation event (P event), illustrated in Fig. S5.1. The first method (Fig. S5.1 a), extracted the atmospheric data for a P event only in the ERA5 grid cell in which the P event occurred. This method was applied in a preliminary version of this study. The second method also includes the mean of a buffer zone of ERA5 grid cells around the identified P events to get more representative values of the atmosphere and is the method applied in this manuscript. This approach is shown in Fig. S5.1 (b)-(d). Fig. S5.1 (c) shows the most common occurrence of P events within one ERA5 grid cell with the neighbouring grid cells. Fig. S5.1 (b) shows two possible exceptions, when the P events occur at the boundary of the study area (i.e. a reduced number of surrounding cells) whereas Fig. S5.1 (d) illustrates the selection of surrounding ERA5 grid cells, when P events are spread over multiple ERA5 grid cells.

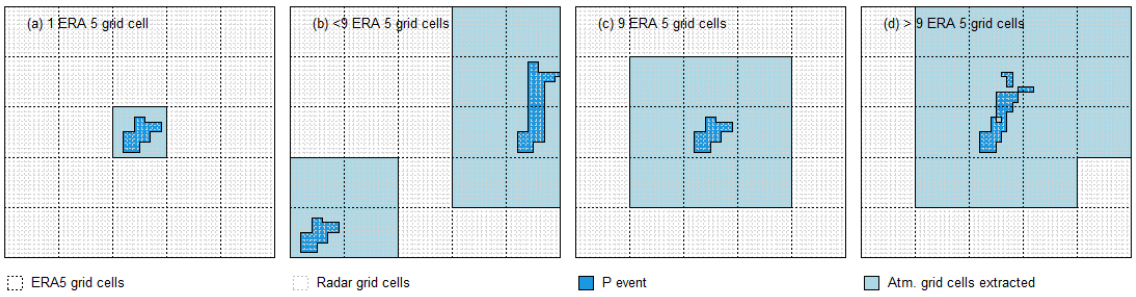

Figure S5.1: Schematic representation of the differing extraction methods compared, with (a) the case of one ERA5 grid cell, (b) including a buffer zone at the boundary of the study area, (c) the standard case of a buffer zone of a one ERA5 grid cell P event and (d) the case of larger P events. Mean values of <9, 9 and >9 ERA5 grid cells are used in the manuscript.

Table S5.1 and Table S5.2 show the number and percentage of P events for different numbers of ERA5 grid cells per P event. Almost 80% of all precipitation events occur within one ERA5 grid cell (Table S3.1), which leads to almost 70% of precipitation events (Table S5.2), that end up with the constellation of Fig. S5.1 (c), including 9 ERA5 grid cells to determine the atmospheric conditions during a precipitation event.

Table S5.1: Number and percentage of P events per number of covered ERA5 grid cells.

No. of ERA5 grid cells per P event	No. of P events	Percentage of P events [%]
1	3054	79.6
2	677	17.6
3	65	1.7
4	39	1.0
6	1	0.03

Table S5.2: Number and percentage of P events per number of ERA5 grid cells including a buffer zone.

No. of ERA5 grid cells per P event incl. buffer zone	No. of P events	Percentage of P events [%]
4	18	0.5
6	470	12.3
8	78	1.9
9	2631	68.6
11	5	0.1
12	551	14.4
15	52	1.4
16	30	0.8
18	4	0.1
20	1	0.03

For each analysed atmospheric variable (e.g. CAPE, q, WS, ...) the parameter range during identified precipitation events is shown in Fig. S5.2. The left boxplot (1) of each panel in Fig. S5.2 shows the parameter value within the one ERA5 grid cell (Fig. S5.1 a), in which the precipitation threshold was crossed. The third column (9) (Fig. S5.2) shows the applied approach of 80% of the P events, where the P event occurred within one ERA5 grid cell. To get a representative value for atmospheric conditions, a mean was calculated for each P event including a buffer zone around the ERA5 event cell (eight neighbouring ERA5 grid cells) (Fig. S5.1 c). The second boxplot (<9) of each panel in Fig. S5.2 shows the exceptions, when precipitation events occurred at the boundary of the study area and the mean could therefore only be calculated from less than 9 grid cells. On the fourth boxplot per panel (>9), the spatially large precipitation events are represented, that cover more than one ERA5 grid cell. The mean of the atmospheric parameters is therefore calculated from more

than 9 ERA5 grid cells. The value ranges of all four groups are rather stable and the different approaches do not make big differences. Therefore, we chose to use all precipitation events, independent of the number of ERA5 grid cells that were used to calculate the mean of the area, to calculate the thresholds.

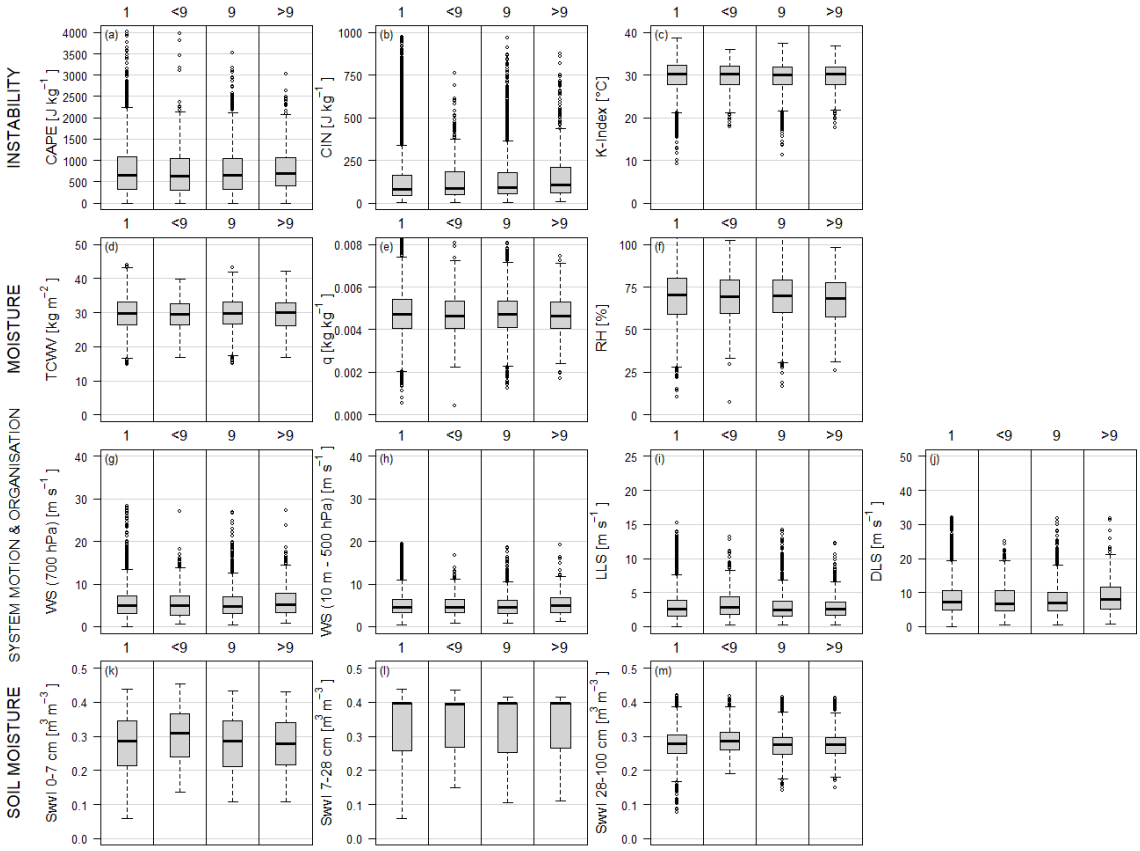

Figure S5.2: ERA5 atmospheric parameter values that are present during precipitation events. The first row (a)-(c) shows the instability parameters. The second row (d)-(f) shows the moisture parameters, the third (g)-(j) the parameters related to system motion and organisation and the fourth (k)-(m) a few parameters related to soil moisture. The left column of each panel shows the parameter range within a single ERA5 grid cell, in which a precipitation event was identified. The second column shows events at the boundary of the study area, where a mean was determined with less than the full surrounding buffer. The third column shows the standard approach of the mean of a regular buffer zone and the fourth shows the precipitation events that span more than one ERA5 grid cell and therefore use a larger number of ERA5 grid cells.